

# Electronic and Geometric Structure of Copper Single-Metal Sites in Zeolites by Hyperfine Spectroscopy and Quantum Chemical Modelling

Der Fakultät für Physik und Geowissenschaften  
der Universität Leipzig  
eingereichte

DISSERTATION

zur Erlangung des akademischen Grades

doctor rerum naturalium  
(Dr. rer. nat.)

vorgelegt

von M.Sc. Paolo Cleto Bruzzese  
geboren am 21.11.1994 in Torino

Leipzig, den 15.09.2022



# Bibliographische Beschreibung

Bruzzese, Paolo Cleto

Electronic and Geometric Structure of Copper Single-Metal Sites in Zeolites by  
Hyperfine Spectroscopy and Quantum Chemical Modelling

Universität Leipzig, Dissertation, 2022

127 S.<sup>1</sup>, 249 Lit.<sup>2</sup>, 15 Tab., 34 Abb., 2 Anlagen

## Abstract

Atomically dispersed transition metal ions in zeolites catalyse a wide range of industrial reactions and are at the centre of intense research interest to design new sustainable synthetic pathways for energy conversion and environment remediation. One of the big challenges in this context is the characterization and location of the active sites. Indeed, mapping their nature with atomic-scale precision occupies a central place in the theory and practice of heterogeneous catalysis.

In this thesis, the site-selectivity and sensitivity of Electron Paramagnetic Resonance (EPR) with its pulsed variants are combined with quantum chemical modelling to determine the microscopic structure of monomeric Cu<sup>II</sup> species in zeolites with Chabazite (CHA) topology as a function of the hydration conditions and sample composition. By isotopic labelling of the zeolite framework with <sup>17</sup>O and employing <sup>17</sup>O ENDOR spectroscopy, the degree of covalency in the Cu-O bond is mapped and the evolution of Cu<sup>II</sup> sites as a function of the hydration conditions is followed. By combining <sup>1</sup>H HYSCORE experiments with state-of-the-art quantum chemical modelling, the EPR signature of the redox active hydroxo-Cu<sup>II</sup> species is univocally identified and a quantitative assessment of its electronic and geometric structure is provided as a function of zeolite composition.

---

<sup>1</sup>... S. (Seitenzahl insgesamt)

<sup>2</sup>... Lit. (Anzahl der im Literaturverzeichnis ausgewiesenen Literaturangaben)

# Contents

<b>List of Figures</b>	<b>1</b>
<b>List of Tables</b>	<b>3</b>
<b>Symbols</b>	<b>5</b>
<b>Abbreviations</b>	<b>6</b>
<b>1 Introduction</b>	<b>8</b>
<b>2 EPR spectroscopy</b>	<b>12</b>
2.1 The spin Hamiltonian approach . . . . .	12
2.2 Continuous wave EPR spectroscopy . . . . .	14
2.3 Pulse EPR techniques . . . . .	19
2.3.1 Free Induction Decay and Electron Spin Echo . . . . .	20
2.3.2 ESEEM techniques . . . . .	22
2.3.3 ENDOR techniques . . . . .	26
2.4 EPR spectroscopy of monomeric Cu <sup>II</sup> species . . . . .	28
2.4.1 Influence of the ligand field splitting on EPR spectra . . .	28
2.4.2 Interpretation of EPR signals of isolated Cu <sup>II</sup> species . . .	32
<b>3 Quantum chemical modelling</b>	<b>35</b>
3.1 Quantum chemical calculation of EPR parameters . . . . .	35
3.1.1 Determination of the spin Hamiltonian terms through an effective Hamiltonian . . . . .	37
3.1.2 Linear response approach . . . . .	40
3.2 Electronic structure methods . . . . .	43
3.2.1 Density Functional Theory . . . . .	43
3.2.2 The Coupled-Cluster theory . . . . .	45
3.3 Quantum chemical modelling of solid state systems . . . . .	47



<b>4</b>	<b>Materials and Methods</b>	<b>49</b>
4.1	Materials . . . . .	49
4.1.1	Copper-exchanged zeolites with Chabazite topology . . .	49
4.2	Methods . . . . .	53
4.2.1	Activation of copper-exchanged Chabazite samples . . . .	53
4.2.2	$^{17}\text{O}$ isotopic labelling of zeolite framework . . . . .	53
4.3	EPR measurements . . . . .	53
4.4	Computational details . . . . .	54
4.4.1	Periodic and cluster modelling . . . . .	54
4.4.2	Periodic calculations . . . . .	55
4.4.3	Cluster calculations . . . . .	56
<b>5</b>	<b>Results and Discussion</b>	<b>58</b>
5.1	$^{17}\text{O}$ EPR characterization of $\text{Cu}^{\text{II}}$ single-metal sites in Chabazite .	59
5.1.1	Structure and dynamics of isolated $\text{Cu}^{\text{II}}$ ions from CW-EPR	59
5.1.2	Geometric and electronic structure through $^{27}\text{Al}$ and $^1\text{H}$ spin density studies . . . . .	62
5.1.3	Nature of the Cu–O bonding interaction from $^{17}\text{O}$ EPR . .	65
5.1.4	Microscopic structure of $\text{Cu}^{\text{II}}$ and Al siting from computa- tional modelling . . . . .	68
5.1.5	Summary . . . . .	72
5.2	The structure of monomeric $[\text{Cu}^{\text{II}}(\text{OH})]^+$ species in Chabazite . .	74
5.2.1	Identification of the EPR signature of $[\text{Cu}^{\text{II}}(\text{OH})]^+$ . . . .	75
5.2.2	Atomistic structure of monomeric $[\text{Cu}^{\text{II}}(\text{OH})]^+$ species . .	81
5.2.3	Quantitative assessment of isolated $\text{Cu}^{\text{II}}$ species in acti- vated Cu-CHA . . . . .	84
5.2.4	Summary . . . . .	86
	<b>Conclusions</b>	<b>87</b>
	<b>A</b>	<b>89</b>
	<b>B</b>	<b>99</b>
	<b>Bibliography</b>	<b>105</b>
	<b>Publications</b>	<b>118</b>



# List of Figures

2.1	Simulated EPR powder spectra (black) with the corresponding absorption spectra (green) of an electron spin $S=1/2$ and associated angular variation in resonant field ( $B_{res}$ ) as a function of the spherical polar angles $\theta, \phi$ (in red and blue). . . . .	17
2.2	Energy levels scheme for an electron spin $S=1/2$ coupled to a nuclear spin $I=1/2$ together with the corresponding EPR spectra. . . . .	18
2.3	Pulse sequences exploiting the ESEEM effect. . . . .	23
2.4	Simulated HYSCORE powder patterns for a $S=1/2$ , $I=1/2$ spin system with an axial hyperfine tensor. . . . .	26
2.5	Davies ENDOR pulse sequence. . . . .	27
2.6	Splitting of the $d$ orbitals in $\text{Cu}^{\text{II}}$ ions. . . . .	29
2.7	Splitting of the $d$ orbitals in $\text{Cu}^{\text{II}}$ complexes with a tetragonal distortion . . . . .	31
2.8	Simulated CW-EPR powder spectra of $\text{Cu}^{\text{II}}$ . . . . .	33
2.9	Peisach-Blumberg plot for different Cu-exchanged zeolites. . . . .	34
4.1	Schematic representation of CHA topology. . . . .	50
5.1	X-band CW-EPR spectra and structural models of $\text{Cu}^{\text{II}}$ single sites in Cu-CHA. . . . .	60
5.2	Experimental and simulated X-band CW-EPR spectra of Cu-CHA(B) recorded at room temperature at different dehydration stages. . . . .	61
5.3	HYSCORE and ENDOR spectra of Cu-CHA(B) at different dehydration stages. . . . .	64
5.4	$^{17}\text{O}$ ENDOR spectra of isotopically enriched Cu-CHA(B). . . . .	67
5.5	Computed energetics and $^{17}\text{O}$ hyperfine couplings of relevant Cu-CHA structures. . . . .	69
5.6	Computed energies of hydrated and dehydrated Cu-CHA models. . . . .	72
5.7	Atomistic structures of the $\text{Cu}^{\text{II}}$ interfacial complexes in Cu-CHA(B). . . . .	73
5.8	Computed Cu speciation as function of zeolite chemical composition space. CW-EPR spectra of $\text{O}_2$ -activated CuCHA samples measured at 77 K and corresponding X-band $^1\text{H}$ HYSCORE spectra. . . . .	76

5.9	Experimental and computer simulations of CW-EPR spectra recorded at 77 K of O <sub>2</sub> -activated Cu-CHA samples. . . . .	77
5.10	Peisach-Blumberg plot for the copper interfacial complexes in O <sub>2</sub> -activated Cu-CHA(C). . . . .	79
5.11	ESE detected EPR spectrum of Cu-CHA(C) with the <sup>1</sup> H HYSCORE spectra recorded at different magnetic fields. . . . .	80
5.12	Atomistic structure, spin density plot and computed <i>g</i> - and <sup>1</sup> H <i>A</i> -tensors orientations of monomeric hydroxo-Cu <sup>II</sup> species in CHA. . . . .	82
5.13	Column graph representing the percentage of Cu species quantified by CW-EPR with respect the total amount of Cu determined by ICP-AES. . . . .	84
A.1	Evaluation of the effect of the nuclear quadrupole interaction in X-band <sup>27</sup> Al HYSCORE experiments measured for hydrated Cu-CHA(B) sample. . . . .	90
A.2	Simulation of the <sup>1</sup> H HYSCORE spectrum of the fully hydrated Cu-CHA(B) sample and of the <sup>27</sup> Al HYSCORE spectrum of the fully dehydrated Cu-CHA(B) sample. . . . .	91
A.3	<sup>17</sup> O Davies ENDOR spectra of the isotopically enriched sample hydrated with H <sub>2</sub> <sup>17</sup> O and with H <sub>2</sub> <sup>16</sup> O. . . . .	93
A.4	Q-band <sup>17</sup> O ENDOR spectra simulation highlighting the contribution of each <sup>17</sup> O species. . . . .	94
A.5	Comparison of experimental (black) and simulated Q-band <sup>17</sup> O ENDOR spectra of the <sup>17</sup> O enriched dehydrated Cu-CHA(B). . . . .	95
A.6	Atomistic structure of Cu <sup>II</sup> species sitting in 6MRs and 8MRs hydrated with 2 and 3 water molecules. . . . .	96
B.1	Experimental and computer simulations of X-band <sup>1</sup> H HYSCORE spectra of O <sub>2</sub> -activated Cu-CHA(C) acquired at different magnetic fields. . . . .	99
B.2	Spin density plots of monomeric Cu <sup>II</sup> -hydroxo cluster model obtained at different level of theories. . . . .	101
B.3	Possible optimized structural geometries of framework bound hydroxo-Cu species in O <sub>2</sub> -activated Cu-CHA. . . . .	101
B.4	<sup>1</sup> H HYSCORE spectra of Cu-CHA(C) together with the computer simulation obtained at the reported magnetic fields. . . . .	102
B.5	Experimental and simulated <sup>1</sup> H HYSCORE spectra taken at different magnetic field setting using the computed spin Hamiltonian parameters. . . . .	103

# List of Tables

5.1	Experimental Cu $g$ - and $A$ -tensors obtained from the simulations of the CW-EPR spectra recorded at 77 K. . . . .	62
5.2	Experimental $^1\text{H}$ and $^{27}\text{Al}$ hyperfine coupling components and quadrupolar coupling constants used for the simulations of HYSCORE and ENDOR spectra in Figure 5.3. . . . .	65
5.3	Experimental $^{17}\text{O}$ hyperfine coupling components and quadrupolar coupling constants used for the simulations of Davies ENDOR spectra in Figure 5.4. . . . .	66
5.4	Experimental Cu $g$ - and $A$ -tensors retrieved from the simulations of the CW-EPR spectra of $\text{O}_2$ -activated Cu-CHA samples. . . . .	78
5.5	Experimental and computed $g_{  }$ and $A_{  }$ (absolute values in MHz) of the principal $\text{Cu}^{\text{II}}$ species in $\text{O}_2$ -activated Cu-CHA samples. . .	81
5.6	Comparison between experimental and calculated spin Hamiltonian parameters at different level of theory on cluster model of monomeric hydroxo- $\text{Cu}^{\text{II}}$ species in CHA. . . . .	83
A.1	B2PLYP-D3 computed $g$ and Cu hyperfine principal components for hydrated cluster models of Cu-CHA compared with experimental values. . . . .	89
A.2	B2PLYP-D3 computed $g$ and Cu hyperfine principal components for dehydrated Cu-CHA models employing three different Al distributions. . . . .	89
A.3	Bond distances of Cu-H obtained from hydrated Cu-CHA models.	90
A.4	Periodic computed spin Hamiltonian parameters of $^{17}\text{O}$ , $^{27}\text{Al}$ and $^1\text{H}$ nuclei on hydrated Cu-CHA models. . . . .	92
A.5	Periodic computed spin Hamiltonian parameters of $^{17}\text{O}$ and $^{27}\text{Al}$ on dehydrated Cu-CHA models experiencing different Al distributions. . . . .	94
A.6	Mulliken spin population analysis and Cu-O bond distances computed for hydrated Cu-CHA models. . . . .	97

A.7	Mulliken spin population analysis and Cu-O bond distances computed for dehydrated Cu-CHA models. . . . .	98
B.1	Speciation of Cu sites and estimation of their amount in activated Cu-CHA samples as reported in literature. . . . .	100
B.2	Computed $^1\text{H}$ hyperfine coupling constants and anharmonic stretching frequencies of OH group bound to Cu for tri- and tetra-coordinated monomeric hydroxo-Cu species. . . . .	104

# Symbols

$\mathbf{A}$	Hyperfine interaction tensor
$a_{iso}$	Isotropic hyperfine interaction
$\mathbf{B}_0$	External magnetic field
$\beta_B$	Bohr magneton ( $9.274\,008\,99 \times 10^{-24} \text{JT}^{-1}$ )
$\beta_n$	Nuclear magneton ( $5.050\,783\,17 \times 10^{-27} \text{JT}^{-1}$ )
$g_e$	Free-electron $g$ value (2.002331)
$g_n$	Nuclear $g$ value
$\hbar$	Reduced Planck constant ( $1.054\,572\,66 \times 10^{-34} \text{Js}$ )
$I$	Nuclear spin quantum number
$\hat{\mathbf{I}}$	Nuclear spin operator
$\hat{\boldsymbol{\mu}}$	Magnetization Vector Operator
$\mathbf{M}$	Macroscopic Magnetization Vector
$\mu_0$	Magnetic constant (vacuum permeability) ( $12.5664 \times 10^{-7} \text{NA}^{-2}$ )
$S$	Electron spin quantum number
$\hat{\mathbf{S}}$	Electron spin operator
$T$	Anisotropic hyperfine interaction
$T_1$	Longitudinal or Spin-Lattice Relaxation
$T_2$	Transverse or Spin-Spin Relaxation
$T_m$	Phase Memory Time

# Abbreviations

**1D** One-Dimensional

**2D** Two-Dimensional

**4MR** Four-Membered Ring

**6MR** Six-Membered Ring

**8MR** Eight-Membered Ring

**BO** Born-Oppenheimer

**CC** Coupled-Cluster

**CCSD** Coupled-Cluster with Single-Double excitations

**CCSD(T)** Coupled-Cluster with Single-Double and perturbative Triple excitations

**CHA** Chabazite

**CO** Crystalline Orbital

**CW** Continuous Wave

**D6MR** Double Six-Membered Ring

**DFT** Density Functional Theory

**ENDOR** Electron-Nuclear Double Resonance

**EPR** Electron Paramagnetic Resonance

**ESE** Electron Spin-Echo

**ESEEM** Electron Spin-Echo Envelope Modulation

**FBZ** First Brillouin Zone



---

<b>FCI</b>	Full Configuration Interaction
<b>FID</b>	Free Induction Decay
<b>GGA</b>	Generalized Gradient Approximation
<b>GIAO</b>	Gauge-Including Atomic Orbital
<b>HF</b>	Hartree-Fock
<b>hfi</b>	Hyperfine interaction
<b>HYSCORE</b>	Hyperfine Sublevel CORrElation
<b>LDA</b>	Local Density Approximation
<b>MO</b>	Molecular Orbital
<b>MP2</b>	Second-Order Many-Body Perturbation Theory
<b>MPT2</b>	Second-Order Many-Body Perturbation Theory
<b>MW</b>	Microwave
<b>NMR</b>	Nuclear Magnetic Resonance
<b>PJTE</b>	Pseudo Jahn-Teller Effect
<b>RF</b>	Radiofrequency
<b>RT</b>	Room Temperature
<b>SCF</b>	Self-Consistent Cycle
<b>SOC</b>	Spin-Orbit Coupling
<b>SOMF</b>	Spin-Orbit Mean-Field
<b>SOMO</b>	Singly Occupied Molecular Orbital
<b>SOS</b>	Sum Over States
<b>SSHC</b>	Single-Site Heterogeneous Catalyst
<b>TMI</b>	Transition Metal Ion
<b>vdW</b>	van-der Waals
<b>zfi</b>	Zero-field interaction

# Chapter 1

## Introduction

The identification of catalytically active sites with atomic-scale precision occupies a central place in the theory and practice of catalysis.<sup>1</sup> Without a detailed understanding of the atomic architecture of the catalytically active centre, we are unlikely to be in a position to improve existing catalysts or design superior new ones.<sup>2</sup>

Such knowledge is particularly important in single-site heterogeneous catalysis<sup>3,4</sup> (SSHCs) where the attractive features of homogeneous and heterogeneous catalysts are combined. In SSHCs, the active sites with regular and tunable architecture related to precise catalytic function are integrated into a thermally stable, porous, solid host that facilitates access of substrates to those sites and separation of products from the catalyst.<sup>5</sup>

Atomically dispersed transition metal ions (TMIs) in zeolites represent a paradigmatic case of SSHCs. Acidic zeolites have established a strong track record as industrial catalysts with initial applications as large scale acid catalysts for the petrochemical industry in 1960s.<sup>6–12</sup> Incorporating extra-framework transition metal ions into their inner pore structure introduces these materials as highly stable oxidation SSHCs, with properties reminiscent of those displayed by metalloenzymes.<sup>13,14</sup> However, unlike enzymes, these inorganic materials are highly robust and can endure harsh reaction conditions. Moreover, the employment of earth-abundant transition metals (i.e. Fe, Cu, Co, Ni, . . .) as active centers in combination with eco-friendly oxidants (i.e. O<sub>2</sub>, H<sub>2</sub>O<sub>2</sub>, N<sub>2</sub>O, . . .) satisfies the increasingly exigent need to design and develop catalysts that can operate in an environmentally benign manner.<sup>15</sup> For such reasons, TMIs zeolite catalysts are promising materials to support the next generation of industrial oxidation processes.<sup>13–16</sup>

Over the past years, copper-exchanged zeolites have been in the focus of comprehensive studies<sup>13,17</sup> due to applications ranging from NO<sub>x</sub> removal<sup>18</sup> to the direct conversion of methane to methanol.<sup>16,19,20</sup> Among other systems, cop-

per-containing zeolites with chabazite (CHA) topology are particularly attractive as they couple industrial and environmental relevance - a Cu-CHA catalyst for diesel engine exhaust was commercialized since 2008 - and structural simplicity.<sup>17</sup> Nevertheless, the exact nature of the Cu active sites and the impact of e.g. the Si/Al and Cu/Al ratios on their atomic structure and, thus, on the catalytic performance are still under debate.<sup>17</sup>

Presumably the most relevant barrier with respect to the experimental characterization of these materials is the presence of inactive spectator metals, which in some cases make up the majority of the extra-framework metal content in TMIs zeolites.<sup>13</sup> As a result, findings obtained from bulk techniques such as X-ray absorption spectroscopy and/or magnetic susceptibility are not always reliable. Despite this, bulk data have been interpreted extensively in the literature, resulting in a range of contradictory assignments for active sites in zeolites. For instance, early reports<sup>21–23</sup> indicated only one extra-framework site in Cu-CHA as exclusive position for Cu ions in the dehydrated materials. Today it is well-established that multiple docking sites are available for Cu<sup>II</sup> and Cu<sup>I</sup> ions, depending on the sample composition and activation procedure adopted.<sup>24–28</sup>

Most of the recent advances in the structural determination of the active species in Cu-CHA are surely connected to the employment of site-selective spectroscopy.<sup>14,16,17</sup> Indeed, spectroscopic techniques with single-site resolution enable correlation of spectroscopic features to individual metal centers limiting the interference from spectator metals.<sup>13</sup> The rigorous spectroscopic finding can then be coupled to electronic structure calculations to associate a microscopic structure to the experimental spectrum and recover its structure-property relationship.

Among the site-selective spectroscopy techniques, Electron Paramagnetic Resonance (EPR) is definitely the most suited one to investigate paramagnetic isolated Cu<sup>II</sup> species in zeolites. The selectivity and sensitivity of EPR have been extensively exploited to probe copper-exchanged zeolites since the 1970s.<sup>29–50</sup> On one hand, it provides quantitative data regarding the total amount of EPR-active Cu<sup>II</sup> sites present. This information can then be used to indirectly quantify also the amount of EPR silent Cu<sup>II</sup> species.<sup>37,51–53</sup> On the other hand, EPR spectroscopy is a powerful tool for determining structural details on Cu<sup>II</sup> ions in zeolites.<sup>29,30,34–36,38,42,43,47,50,51</sup> Besides, the potential of EPR is not limited to paramagnetic Cu<sup>II</sup> species but also diamagnetic Cu<sup>I</sup> sites have been indirectly characterized by using paramagnetic spin probes (i.e. NO).<sup>41,54–60</sup>

Modern EPR spectroscopy has reached an impressive level of sophistication. State-of-the-art pulse techniques allow for the detection of very weak interactions between the unpaired electron and surrounding nuclei, thus allowing for geometric structures to be deduced from spectroscopic measurements with high

level of accuracy. Two EPR tools which have been useful for the direct observation of nearby nuclei in Cu<sup>II</sup>-exchanged zeolites are Electron Spin-Echo Envelope Modulation (ESEEM) spectroscopy<sup>31,33,39,44,48,61,62</sup> and Electron-Nuclear Double Resonance (ENDOR) spectroscopy.<sup>32,45,59,63–66</sup> Information on the local environment (nature of the ligand atoms, distances of interacting nuclei, degree of covalency in the metal-ligand bond and coordination geometry) can be obtained using both ESEEM and ENDOR spectroscopies through the nuclear frequencies of nearby nuclei (usually <sup>1</sup>H and <sup>27</sup>Al nuclei).

The analysis (least-squares fitting) of the EPR signal leads to a set of parameters known as spin Hamiltonian parameters.<sup>67</sup> These phenomenological parameters represent a concise summary of the experimental results and are strictly dependent on the geometric and electronic nature of the paramagnetic center.

The spin Hamiltonian terms may be calculated by using electronic structure methods.<sup>68</sup> Quantum chemical calculations represent an impressive tool because it helps to correlate the EPR parameters with the electronic structure, not just the geometric structure. Since electronic structure is intimately related to reactivity, this sheds light on the reactive properties of the active sites. In spite of such attractive opportunities, only few computational studies combined experimental EPR data with reliable theoretical modelling of the Cu<sup>II</sup> species present in Cu-zeolites and their computed EPR parameters.<sup>69–73</sup> Moreover, the majority of such works are restricted on the computation of the spin Hamiltonian parameters of Cu<sup>II</sup> ions which are still a great challenge for quantum chemistry methods.<sup>74–76</sup> On the other hand, the calculation of weak interactions between the unpaired electron of Cu<sup>II</sup> ions and surrounding nuclei is far more reliable<sup>77</sup> and very rewarding.<sup>78,79</sup>

Therefore an ideal approach towards the atomistic determination of the active Cu<sup>II</sup> species in copper-loaded zeolites might be to initially use EPR data containing the interaction with the magnetic nuclei of the ligands to build an appropriate theoretical model, compute the EPR observables related to that structure and validate the model by directly comparing the computed parameters to the experimental ones. The latter process may then guide further experimental efforts, starting the second cycle of theoretical approximation.<sup>80</sup>

The study reported in this PhD thesis is precisely based on such interplay and exchange between experimental and theoretical methodologies. The combined approach allows to provide unprecedented details on the structure of copper single-metal sites in zeolites with CHA framework as a function of hydration conditions<sup>78</sup> and zeolite composition.<sup>79</sup>

After introducing into the topics of the thesis, a brief summary of its content is given in the following.

The second chapter provides a general description of the EPR techniques em-

ployed in this thesis, outlining the information that can be extracted from the various experiments. The theory behind the two main EPR methodologies employed in this thesis (continuous wave (CW) and pulse modes) is briefly described. In particular, the widely used continuous wave CW-EPR spectroscopy of monomeric  $\text{Cu}^{\text{II}}$  species is discussed in more detail.

The third chapter regards the theory of the quantum chemical methods employed in this study. In particular, it deals with the connection between the spin Hamiltonian and the many-particle Hamiltonian. Moreover, the quantum chemical approximations adopted here are briefly reviewed.

The fourth chapter illustrates the materials and methods employed to perform the experiments carried out in this thesis as well as the computational details. Recipes for the synthesis of the materials, specific activation protocols and isotopic labelling procedures are also outlined.

In the fifth chapter, the results are presented and discussed. In the first section the local structure of single-site  $\text{Cu}^{\text{II}}$  species in a Cu-CHA material is determined as function of the hydration level of the material by  $^{17}\text{O}$  isotopic labelling of the zeolite framework, in conjunction with ENDOR methodologies and theoretical modelling. The second section concerns the structural assessment of hydroxo- $\text{Cu}^{\text{II}}$  species in Cu-CHA zeolites as a function of the sample composition (Si/Al and Cu/Al ratios) by combining ESEEM experiments and cutting-edge quantum chemical modelling.

Finally, a conclusive chapter summarizes the results of this thesis highlighting the most important achievements. Additional experimental and computational data may be found in the appendices at the end of the thesis.

# Chapter 2

## EPR spectroscopy

This chapter provides an overview of the electron paramagnetic resonance techniques exploited in this thesis. First, the terms of the spin Hamiltonian approach will be shortly described. Afterwards, the attention will be focused on the two EPR methodologies (continuous wave and pulse modes) employed together with few practical insights concerning the interpretation and analysis of CW-EPR spectra of  $\text{Cu}^{\text{II}}$  species.

### 2.1 The spin Hamiltonian approach

EPR transitions are based on the interaction of the magnetic dipoles associated with unpaired electrons with magnetic fields, which can be both external (static field, oscillatory microwave field) and internal (*e.g.* due to the presence of magnetically active nuclei in the local environment).<sup>81–83</sup> The energies and corresponding eigenstates of a spin system with electron spin  $S$  and  $m$  nuclei with spin  $I$  in an external magnetic field  $\mathbf{B}_0$  can be described by the spin Hamiltonian formalism introduced by Abragam and Pryce in 1951:<sup>84</sup>

$$\hat{\mathcal{H}}_{spin} = \hat{\mathcal{H}}_{EZ} + \hat{\mathcal{H}}_{NZ} + \hat{\mathcal{H}}_{HF} + \hat{\mathcal{H}}_{NQ} + \hat{\mathcal{H}}_{ZFS} \quad (2.1)$$

which in its explicit form becomes:

$$\hat{\mathcal{H}}_{spin} = \frac{\beta_B \mathbf{B}_0 \mathbf{g} \hat{\mathbf{S}}}{h} - \beta_n \sum_{k=1}^m \frac{g_{n,k} \mathbf{B}_0 \hat{\mathbf{I}}_k}{h} + \sum_{k=1}^m \hat{\mathbf{S}} \mathbf{A}_k \hat{\mathbf{I}}_k + \sum_{I_k > 1/2} \hat{\mathbf{I}}_k \mathbf{Q}_k \hat{\mathbf{I}}_k + \hat{\mathbf{S}} \mathbf{D} \hat{\mathbf{S}} \quad (2.2)$$

The term  $\hat{\mathcal{H}}_{EZ}$  is the electron Zeeman interaction which describes the coupling between magnetic dipole moment associated with the spin angular momentum operator  $\hat{\mathbf{S}}$  and the external magnetic field  $\mathbf{B}_0$ .  $\beta_B$  is the Bohr magneton, the matrix  $\mathbf{g}$  is the  $\mathbf{g}$ -tensor with the principal values  $g_x$ ,  $g_y$  and  $g_z$  and  $h$  is the Planck

constant.

The second term of equations 2.1 and 2.2 is the nuclear Zeeman interaction involving the coupling between the magnetic dipoles of  $m$  nuclei (described by the nuclear spin operators  $\hat{\mathbf{I}}_k$ ) with the external magnetic field  $\mathbf{B}_0$ .  $\beta_n$  is the nuclear magneton and  $g_n$  is the dimensionless nuclear  $g$  factor, specific for each nucleus.

The coupling between the electronic and nuclear spins is described by the hyperfine interaction (hfi) term  $\hat{\mathcal{H}}_{HF}$  (see equations 2.1 and 2.2), where  $\mathbf{A}_k$  are the hyperfine matrices and  $\hat{\mathbf{I}}_k$  are the nuclear spin operators (already introduced in the previous paragraph). The hyperfine interaction consists of two different contributions: the Fermi contact (isotropic) interaction and the electron-nuclear dipole-dipole (anisotropic) interaction. The Fermi contact term ( $\hat{\mathcal{H}}_{iso}$ ) arises from the presence of finite electron spin density at the nucleus, so it becomes particularly important when there are contributions of  $s$  orbitals. This interaction can be written as:

$$\hat{\mathcal{H}}_{iso} = a_{iso} \hat{\mathbf{S}} \hat{\mathbf{I}} \quad (2.3)$$

with

$$a_{iso} = \frac{8\pi}{3} g_e \beta_B g_n \beta_n |\Psi_0(0)|^2 \quad (2.4)$$

where  $|\Psi_0(0)|^2$  is the electron spin density at the nucleus and  $a_{iso}$  is the isotropic hyperfine coupling constant. Contribution of electron density on the nucleus may also occur when the unpaired electron dwells in a  $p$  or  $d$  orbitals through core-polarization effects.<sup>85</sup> The anisotropic part can be written as:

$$\hat{\mathcal{H}}_{DD} = \frac{\mu_0}{4\pi\hbar} g_e \beta_B g_n \beta_n \left[ \frac{(3Sr)(rI)}{r^5} - \frac{SI}{r^3} \right] = \hat{\mathbf{S}} \mathbf{T} \hat{\mathbf{I}} \quad (2.5)$$

where  $r$  is the distance vector between the nuclear and electron spin,  $\mu_0$  is the vacuum permeability and  $\mathbf{T}$  is the traceless dipolar coupling matrix defined as:

$$\mathbf{T} = T \begin{bmatrix} -(1-\rho) & 0 & 0 \\ 0 & -(1-\rho) & 0 \\ 0 & 0 & 2 \end{bmatrix} \quad (2.6)$$

where  $T$  is the dipolar coupling constant and  $\rho$  is the asymmetry parameter. The full  $\mathbf{A}$ -tensor can be written as:

$$\mathbf{A} = \mathbf{1} a_{iso} + \mathbf{T} \quad (2.7)$$

$\hat{\mathcal{H}}_{NQ}$  in equation 2.1 is the nuclear quadrupole interaction and it arises only for nuclei with nuclear spin  $I > 1/2$ . Indeed, nuclei with  $I > 1/2$  possess a non-spherical charge distribution, resulting in an electric quadrupole moment

which interacts with the electric field gradient caused by other species in the surrounding.  $Q$  in equation 2.2 is the traceless nuclear quadrupole tensor. In its principal axes system, the  $\hat{\mathcal{H}}_{NQ}$  is given by:

$$\hat{\mathcal{H}}_{NQ} = \frac{e^2 q Q / h}{4I(2I - 1)} [3I_z^2 - I(I + 1) + \eta(I_x^2 - I_y^2)] \quad (2.8)$$

where  $eq$  is the magnitude of the electric field gradient experienced by the nucleus and  $Q$  is the quadrupole moment of the nucleus.

The last term ( $\hat{\mathcal{H}}_{ZFS}$ ) of equations 2.1 and 2.2 is the zero-field interaction (zfi) and it must be taken in account for electron spins  $S > 1/2$ . Its origin derives from dipolar interactions between electron spins<sup>67</sup> as well as from the spin-orbit coupling between the electron spins and their orbital motion.<sup>86</sup> The  $\hat{\mathcal{H}}_{ZFS}$  can also be conveniently expressed in its principal axes frame:

$$\hat{\mathcal{H}}_{ZFS} = D \left[ \hat{S}_z^2 - \frac{1}{3}S(S + 1) \right] + E(\hat{S}_x^2 - \hat{S}_y^2) \quad (2.9)$$

where the operators  $\hat{S}_u^2$  are the projection of  $\hat{S}$  on the respective principal axes of the zfi tensor.  $D$  and  $E$  are directly linked with the symmetry of the zfi tensor: they are both diverse from zero for a rhombic symmetry whereas in case of axial  $E = 0$  and  $D \neq 0$ .

Unlike the nonrelativistic Hamiltonian, the spin Hamiltonian is typically of low dimension (just  $2S+1$  for the electronic degrees of freedom) and, hence, reasonably easily handled. Indeed, the exact solution of the spin Hamiltonian and therefore the reproduction of the EPR spectral features can be carried out with numerical simulation programs (such as Easyspin).<sup>87</sup>

## 2.2 Continuous wave EPR spectroscopy

The most widely spread EPR method is CW-EPR.<sup>88</sup> In the CW technique, a continuous source of microwave (MW) radiation of fixed frequency is applied to the system in presence of an external magnetic field to induce the electron spin transitions. Among the interactions reported in equation 2.1, the electron Zeeman term is the most affected one since it depends significantly on the magnetic field, whereas, for example, nuclear Zeeman interaction cannot be usually resolved in CW experiments.

In the simplest case, the interaction of one unpaired electron with spin  $S=1/2$  and an external magnetic field  $B_0$  results in the splitting of the energy levels of the spin states,  $\beta$  ( $m_s=-1/2$ ) and  $\alpha$  ( $m_s=+1/2$ ), which correspond to the parallel or anti-parallel orientation of the electron spin with respect to the



magnetic field vector. The allowed energy levels of the systems, corresponding to the two allowed orientations of the spins, are defined by:

$$E_{\pm} = \pm 1/2 g_e \beta_e B \quad (2.10)$$

and the resulting energy difference between the two energy states is:

$$\Delta E = g_e \beta_e B \quad (2.11)$$

The spin population over the two states at the thermal equilibrium follows the Boltzmann law:

$$\frac{n_{\alpha}}{n_{\beta}} = e^{-\frac{\Delta E}{kT}} \quad (2.12)$$

Since the MW frequency is fixed, the resonance condition

$$h\nu = \Delta E = g_e \beta_e B \quad (2.13)$$

is fulfilled for a single and distinct magnetic field  $B = B_0^{res}$ . Only at this field MW radiation is absorbed by the system. The detection of the absorbed MW energy, as function of the magnetic field, results in the observed EPR signal. However, in the common CW setup, the external magnetic field magnitude is superimposed by a small oscillating magnetic field which also modulates the measured EPR spectrum. The corresponding magnitude of the oscillating part of the detected signal is consequently the first derivative of the typical adsorption spectrum.

Equations 2.1 and 2.2 consider the free electron case, without any influence from the local surroundings. In real systems, the unpaired electron belongs to a specific environment, such as a molecular or crystalline systems, it is associated to a specific orbital and thus to an orbital angular momentum and a spin angular momentum which indeed cause a deviation of the  $g$  value from the free electron  $g_e$  value. Besides, the geometry of the system may be such that the interaction of the electron spin with the applied magnetic field depends on their relative orientation, making the  $g$  value anisotropic. Indeed, the chemical environment of the unpaired electron exerts additional electromagnetic fields, thus the effective field  $B_{eff}$  experienced by the electron spin is the sum of the external and internal fields. The  $\hat{\mathcal{H}}_{EZ}$  can therefore be rewritten as:

$$\hat{\mathcal{H}}_{EZ} = \frac{\beta_e g_e B_{eff} S}{\hbar} = \frac{\beta_e g B_0 S}{\hbar} \quad (2.14)$$

where  $\hbar$  is the reduced Planck constant and  $g$  is a tensor describing the orientation dependence of the Zeeman splitting. In the principal axes frame the

$g$ -tensor becomes:

$$\mathbf{g} = \begin{bmatrix} g_{xx} & & \\ & g_{yy} & \\ & & g_{zz} \end{bmatrix} \quad (2.15)$$

For fluid solutions, the tumbling rate of the paramagnetic centre is much faster than the timescale of a EPR measurement. In such conditions, the anisotropy of  $g$  is mediated and only the average  $g$  value  $(g_{xx} + g_{yy} + g_{zz})/3$  can be retrieved. On the other hand, in the case of solid samples, such as single crystals, solid powders or frozen solutions, the  $g$  anisotropy can be measured. The  $g$ -tensor of a single crystal can be obtained by recording CW-EPR spectra for various orientations of the crystal axes with respect to the external magnetic field. For polycrystalline materials (powder or frozen solutions), a random collection of orientations of the paramagnetic centre with respect to the applied magnetic field occurs. As result of this, only the principal values of the  $g$ -tensor are directly obtained from the EPR spectrum, but not the orientation of the  $g$ -tensor with respect to the crystal axes frame. The peaks of an EPR powder spectrum correspond to turning points on the spherical surface  $B(\theta, \phi)$  representing the angular dependency of the resonant field:

$$\frac{\partial B_{res}(\theta, \phi)}{\partial \theta} = 0 \text{ and } \frac{\partial B_{res}(\theta, \phi)}{\partial \phi} = 0 \quad (2.16)$$

When the  $g$ -tensor has a rhombic symmetry ( $g_{xx} \neq g_{yy} \neq g_{zz}$ ), the orientation dependence can be written as:

$$g(\theta, \phi) = (g_{xx}^2 \sin^2 \theta \cos^2 \phi + g_{yy}^2 \sin^2 \theta \sin^2 \phi + g_{zz}^2 \cos^2 \theta)^{1/2} \quad (2.17)$$

In the case of an axial  $g$ -tensor, assuming the rotational symmetry axis lying along  $z$ , two components are equal and known as  $g_{\perp} = g_x = g_y$ , whereas the other component is indicated as  $g_{\parallel} = g_z$ .<sup>88</sup>

$$g(\theta) = (g_{\perp}^2 \sin^2 \theta + g_{\parallel}^2 \cos^2 \theta)^{1/2} \quad (2.18)$$

A graphical representation of the orientation dependence of the EPR signal for an axial and rhombic symmetry is reported in Figure 2.1.

Although the electron Zeeman term is the main interaction in CW-EPR, hyperfine interactions may also be observed. In general, two limiting cases are distinguished depending on the size of the hfi considered: (1)  $A_{xx,yy,zz} > \Delta B_{1/2}^{EPR}$  (where  $\Delta B_{1/2}^{EPR}$  is the EPR linewidth of a spin packet and  $A_{xx,yy,zz}$  are the principal values of the hyperfine tensor) and (2)  $A_{xx,yy,zz} < \Delta B_{1/2}^{EPR}$ . In case (1) the hyperfine contribution can be extracted directly from the CW-EPR spectrum,

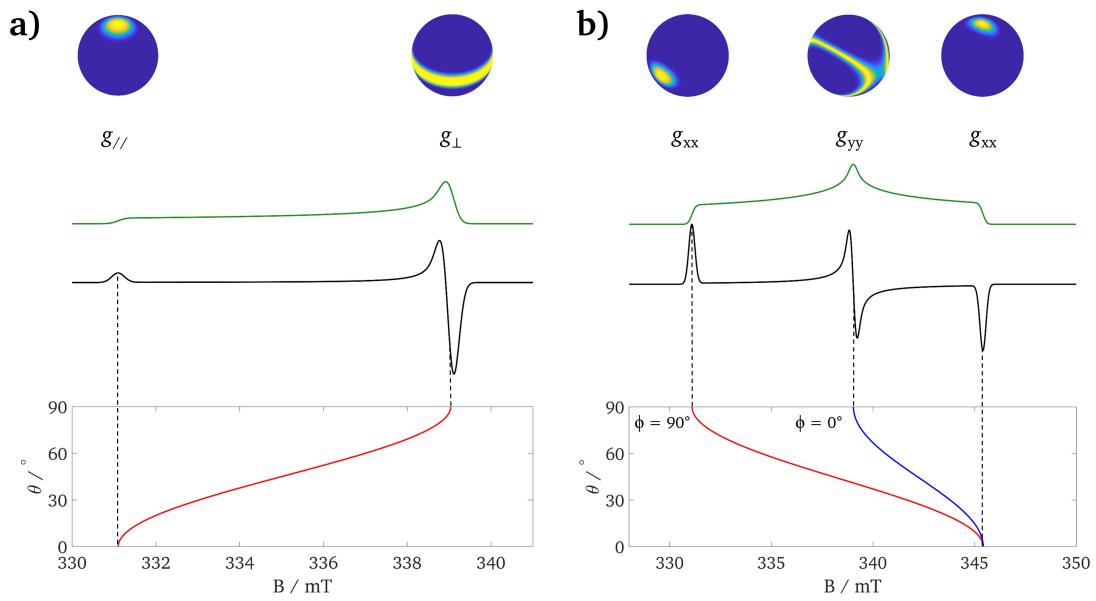


**Figure 2.1:** Simulated EPR powder spectra (black) with the corresponding absorption spectra (green) of an electron spin  $S=1/2$  and associated angular variation in resonant field ( $B_{res}$ ) as a function of the spherical polar angles  $\theta, \phi$  (in red and blue). a) Axial case with  $g_{//} = 2.050$  and  $g_{\perp} = 2.002$  and b) rhombic case with  $g_{xx} = 2.050$ ,  $g_{yy} = 2.002$  and  $g_{zz} = 1.965$ . In both cases, the orientation selection spheres are shown on top. The spectra were simulated by using a frequency of  $\nu = 9.5$  GHz.

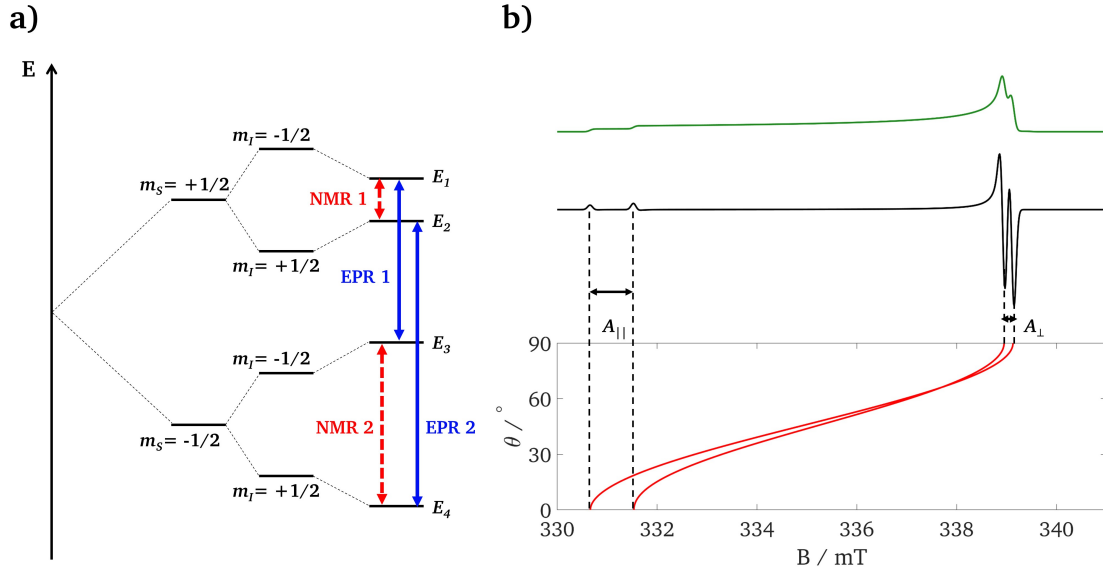


**Figure 2.2:** a) Energy levels scheme for an electron spin  $S=1/2$  coupled to a nuclear spin  $I=1/2$  (e.g., a proton) in the presence of a magnetic field  $B_0$ . b) Simulated EPR powder spectrum (black) with the corresponding absorption spectra (green) of an electron spin  $S=1/2$  coupled to a nuclear spin  $I=1/2$  and associated angular variation in resonant field ( $B_{res}$ ) as a function of the spherical polar angle  $\theta$  (red). Both  $g$ - and  $A$ -tensors are assumed axial ( $g_{\parallel} > g_{\perp}$  and  $A_{\parallel} > A_{\perp}$ ) and collinear. The spectra were simulated by using a frequency of  $\nu = 9.5$  GHz.

whereas in case (2) the so-called hyperfine techniques based on pulse sequences must be adopted to recover the hyperfine tensor (*vide infra*).

To understand the shape of CW-EPR powder spectra in case (1), one may consider the simplest case of an electron spin  $S=1/2$  coupled to a nucleus with  $I=1/2$ . The diagonalization of the corresponding spin Hamiltonian gives the following eigenvalues:<sup>83</sup>

$$E_{1,2} = \frac{\beta_B g B_0}{2} \pm \frac{1}{2} K(+) \text{ for } m_s = 1/2 \quad (2.19)$$

$$E_{3,4} = \frac{\beta_B g B_0}{2} \pm \frac{1}{2} K(-) \text{ for } m_s = -1/2 \quad (2.20)$$

with

$$K(\pm) = \sqrt{\frac{1}{4} (A_{xz}^2 + A_{yz}^2) + \left( -\beta_n g_n B_0 \pm \frac{1}{2} A_{zz} \right)^2} \quad (2.21)$$

The EPR transitions energies are obtained from the selection rules  $\Delta m_S = \pm 1$ ,

$\Delta m_I = 0$  and correspond to:

$$E_1 - E_3 = \beta_B \mathbf{g} \mathbf{B}_0 - \frac{1}{2} K(+) + \frac{1}{2} K(-) \quad (2.22)$$

$$E_2 - E_4 = \beta_B \mathbf{g} \mathbf{B}_0 + \frac{1}{2} K(+) - \frac{1}{2} K(-) \quad (2.23)$$

The nuclear magnetic resonance (NMR) or hyperfine transitions result from the selection rules  $\Delta m_I = \pm 1$ ,  $\Delta m_S = 0$  and are given by:

$$E_1 - E_2 = K(+) \quad (2.24)$$

$$E_3 - E_4 = K(-) \quad (2.25)$$

The resulting energy levels scheme is illustrated in Figure 2.2a. Since the allowed EPR transitions occur between energy levels corresponding to the same nuclear spin state, the effect of the nuclear Zeeman interaction is canceled and the EPR spectrum of a system with one unpaired electron and a single  $I=1/2$  nucleus consists of two lines separated by the hyperfine splitting constant. This treatment is easily extended to the case of a nucleus with a generic nuclear spin  $I$  by taking into account that the allowed spin components are  $2I+1$ . Therefore, each electron spin Zeeman level will be separated by the hyperfine interaction into  $2I+1$  levels and the CW-EPR spectrum will consist of  $2I+1$  lines.

Figure 2.2b shows an example of polycrystalline CW-EPR spectrum for a system with  $S=1/2$  and  $I=1/2$  possessing axial and collinear  $\mathbf{g}$ - and  $\mathbf{A}$ -tensors ( $A_{xx,yy,zz} > \Delta B_{1/2}^{EPR}$ ). Each peak of the EPR powder spectrum is splitted due to the hfi and the separation of the two peaks at lower field gives the  $A_{\parallel}$  component whereas the separation of the two peaks at higher field provides the  $A_{\perp}$  component of the  $\mathbf{A}$ -tensor.

## 2.3 Pulse EPR techniques

A significant amount of the information provided by EPR spectroscopy on the structure and spin distribution can be retrieved through analysis of the hyperfine interactions. However, if the magnitude of such interactions is small, this information will remain unresolved, hidden under the linewidth of the CW-EPR spectrum ( $A_{xx,yy,zz} < \Delta B_{1/2}^{EPR}$ ). Fortunately, a variety of advanced EPR techniques are available to recover the so-called superhyperfine interactions from the magnetic nuclei surrounding the unpaired electron. In such experiments microwave pulses are used to excite the electron spin to manipulate the magnetization. The kind of pulse sequence and the specific scheme of variation of the interpulse times determine the outcome of the measurement. It is worth men-

tioning that CW and pulse EPR are complementary methodologies: CW-EPR is particularly efficient for identifying transitions between electron spin states (EPR 1 and EPR 2 in Figure 2.2a), while pulse EPR allows to observe transitions within electron spin states from electron-nuclear interactions (NMR 1 and NMR 2 in Figure 2.2a).

In the following, the pulse EPR techniques employed in this thesis will be briefly described. They can be divided into two classes: ESEEM and ENDOR techniques. For a detailed description of the formalism used in pulse techniques, the reader is referred to the textbook by Schweiger and Jeschke.<sup>89</sup>

### 2.3.1 Free Induction Decay and Electron Spin Echo

According to a fundamental theorem of quantum mechanics known as *Levitt* theorem, each electron with spin  $S$  has a magnetization defined by the vector operator  $\hat{\mu}$ .<sup>90</sup>

$$\hat{\mu} = -g\mu_B\hat{S} \quad (2.26)$$

where  $g$  is the respective g-factor. The macroscopic magnetization vector  $M$  per unit volume at temperature  $T=0$  K is related to this microscopic quantity via:

$$M = n\langle\hat{\mu}\rangle \quad (2.27)$$

where  $n$  is the density of spins and  $\langle\cdot\rangle$  is the expectation value averaged over all the independent sample quantum states. Equation 2.27 can be rewritten as:

$$M = \frac{1}{V} \sum_{i=1}^N \mu_i \quad (2.28)$$

in which the sum runs over all  $N$  electrons  $i$  within the volume  $V$ .

The variation of the magnetization as a function of time is described by the Bloch equations:<sup>91</sup>

$$\frac{\partial M}{\partial t} = \frac{-g\mu_B}{\hbar} M \times B_0 \quad (2.29)$$

$M$  thus precesses  $B_0$  according to the Larmor frequency  $\nu_L$ :

$$\nu_L = \frac{g\mu_B B_0}{\hbar} \quad (2.30)$$

In thermal equilibrium, in presence of external magnetic field, the macroscopic magnetization  $M_z$  is aligned parallel to  $B_z$ . During a pulse EPR experiment, the application of a short microwave pulse with frequency  $\omega_{mw}$  causes the

rotation of the magnetization  $M_z$  through a flip angle  $\beta$ .  $\beta$  is defined as:

$$\beta = \gamma_e B_1 t_p = \nu_1 t_1 \quad (2.31)$$

where  $\gamma_e$  is the gyromagnetic ratio of the electron spin,  $B_1$  is the intensity of the microwave pulse and  $t_p$  is the pulse duration. In the simplest case,  $\beta = 90^\circ$  ( $\pi/2$  pulse) leads the longitudinal  $M_z$  to transverse  $M_{xy}$  magnetization. If the MW frequency does not match the Larmor frequency, the magnetization rotates about the  $z$  axis with a frequency  $\nu = \nu_L - \nu_{mw}$  in the rotating frame. In the laboratory frame, the magnetization rotates with the Larmor frequency. The detection of this so-called Free Induction Decay (FID) signal is done by down-conversion to video frequencies by mixing with the microwave of the source and measuring the difference frequency  $\nu$ .

The FID signal decays due to transverse relaxation or spin-spin relaxation ( $T_2$ ). Its magnitude describes how quickly the magnetization in the  $xy$ -plane disappears. On the contrary, the spin-lattice relaxation time ( $T_1$ ) is the time it takes for the magnetization to irreversibly returns along the  $z$ -axis. Normally,  $T_2$  is much shorter than  $T_1$ . For this reason the FID signal is not easily detected in EPR experiments.

However, the most popular pulse EPR techniques are typically based on the so-called spin-echo sequences. The simplest pulse sequence to obtain a spin echo was discovered for the first time by Hahn and it is composed of the following pulse progression:  $\pi/2 - \tau - \pi - \tau - echo$ .<sup>92</sup> The electron spin-echo (ESE) obtained is also known as Hahn echo. In the Hahn echo experiment, the  $M_z$  magnetization is turned into transverse magnetization along the  $y$ -axis by applying a  $90^\circ$  pulse. After a time  $\tau$ , a  $180^\circ$  pulse is applied along the  $x$ -axis so that after a further  $\tau$  interval all the group of spins are aligned again into the  $y$ -direction. The decay time of the Hahn echo is described by the phase memory time  $T_m$ , defined as the time taken by the echo amplitude to reach  $1/e$  of its initial value.  $T_m$  includes effects of transverse relaxation as well as spin diffusion.<sup>89</sup> Therefore, ESE-detected measurements may be useful for distinguishing species possessing different relaxation times: indeed, using long  $\tau$  values only the species with sufficiently long  $T_m$  can contribute to the signal. In the ESE-detected EPR experiment, the echo intensity is detected as a function of the applied external magnetic field  $B_0$ . The external magnetic field is increased in small time steps over a certain range and at each point the intensity of the Hahn echo is detected after the two-pulse sequence. The so-called field swept ESE-detected EPR spectrum looks like the absorption EPR spectrum, but it is more sensitive to broad lines difficult to detect by CW-EPR.

As well as the Hahn echo, a stimulated echo can be generated by the following pulse sequence:  $\pi/2 - \tau - \pi/2 - T - \pi/2 - \tau - echo$ .<sup>93</sup> Both the Hahn and

stimulated echoes represent the basis of further experiments described in the next paragraph.

### 2.3.2 ESEEM techniques

ESEEM experiments are employed to observe nuclear frequencies from magnetic nuclei coupled with the unpaired electron.<sup>94</sup> They are based on pulse sequences that create an ESE (both Hahn or stimulated). Typically, in ESEEM experiments the echo amplitude or intensity is recorded in dependence on a pulse delay. The Fourier transformation of the obtained time domain signal results in a frequency domain spectrum featuring the nuclear frequencies of the system. This is the so-called Electron Spin-Echo Envelope Modulation (ESEEM) effect.<sup>93,95,96</sup>

The simplest ESEEM experiment exploits the two-pulse sequence (see Figure 2.3a)  $\pi/2 - \tau - \pi - \tau - \text{echo}$  for creating a Hahn echo (2P-ESEEM).<sup>93</sup> The first  $\pi/2$  pulse generates electron spin coherence, which evolves during the time period  $\tau$ , then the  $\pi$  pulse mixes the electron coherences and after a second evolution time  $\tau$  the echo intensity is detected as a function of  $\tau$ . The exponential decay follows the  $T_m$  of the electron spin. However, if there are magnetic nuclei ( $I$ ) surrounding the unpaired electron, the decay of the echo is modulated due to the presence of weak hyperfine and quadrupole interactions. Nuclear modulations can only be observed when the probability of the forbidden EPR transitions is not zero. In practice, this means that either the hyperfine interactions are anisotropic or quadrupole couplings are different from zero. The two-pulse modulation formula for a system with  $S=1/2$  and  $I=1/2$  is given by:

$$V_{2P}(\tau) = 1 - \frac{k}{4} [2 - 2 \cos(\omega_\alpha \tau) - 2 \cos(\omega_\beta \tau) + \cos(\omega_+ \tau) + \cos(\omega_- \tau)] \quad (2.32)$$

where  $\omega_\alpha$  and  $\omega_\beta$  are the nuclear transition angular frequencies,  $\omega_+ = \omega_\alpha + \omega_\beta$  and  $\omega_- = \omega_\alpha - \omega_\beta$ . Assuming a point-dipole approximation, the nuclear frequencies  $\omega_\alpha$  and  $\omega_\beta$  are given by:

$$\omega_\alpha = |\omega_{1,2}| = \left[ \left( \omega_I + \frac{A}{2} \right)^2 + \frac{B^2}{4} \right]^{1/2} \quad (2.33)$$

$$\omega_\beta = |\omega_{3,4}| = \left[ \left( \omega_I - \frac{A}{2} \right)^2 + \frac{B^2}{4} \right]^{1/2} \quad (2.34)$$

$k$  is the modulation depth parameter and it is defined as:

$$k = \frac{9}{4} \left( \frac{\mu_0 g \mu_B}{4\pi B} \right)^2 \frac{\sin^2(2\theta)}{r^6} \quad (2.35)$$



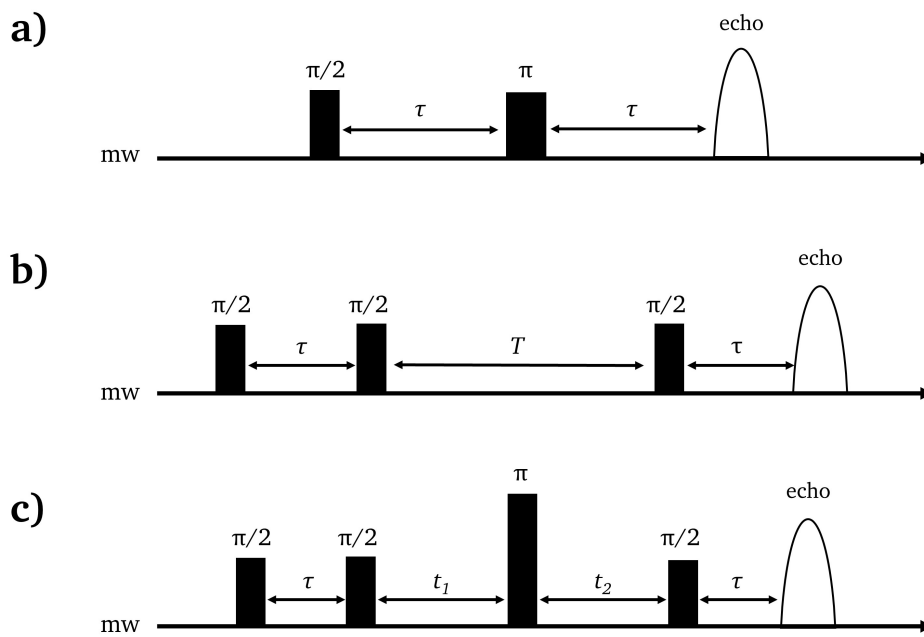


**Figure 2.3:** Pulse sequences exploiting the ESEEM effect. a) Two-pulse sequence and the Hahn echo for 2P-ESEEM. b) Three-pulse sequence and the stimulated echo for 3P-ESEEM. c) Four-pulse sequence for the HYSORE experiment.

where  $r$  is the electron-nucleus distance. The modulation of the electron spin-echo due to couplings with  $j$  nuclei combine in a multiplicative way and are superimposed on the exponential decay of the Hahn echo according to

$$V'_{2P}(\tau) = \exp\left(\frac{-2\tau}{T_M}\right) \prod_j V_{2P,j}(\tau) \quad (2.36)$$

Hence, if the electron spin interacts with several nuclei, combinations between all nuclear frequencies can occur complicating the spectral pattern. According to Equation 2.36, the modulation time trace is a function of the phase memory time  $T_m$ , which is typically short. This is the major drawback of the 2P-ESEEM experiment which may lead to unresolved low frequency modulations.

In a three-pulse ESEEM (3P-ESEEM)<sup>93,97</sup> experiment a stimulated echo is generated by the sequence  $\pi/2 - \tau - \pi/2 - T - \pi/2 - \tau - echo$  (Figure 2.3b). After the generation of electron spin coherence with the  $\pi/2$  pulse and their free evolution during time  $\tau$ , a second  $\pi/2$  pulse creates nuclear coherence which evolves during time  $T$ . The third  $\pi/2$  pulse transfers the nuclear coherence back to electron coherence. The echo envelope decays modulated by the nuclear transition frequencies according to:

$$V_{3P}(\tau, T) = 1 - \frac{k}{4} \{ [1 - \cos(\omega_\alpha \tau)] [1 - \cos(\omega_\beta (\tau + T))] + [1 - \cos(\omega_\beta \tau)] [1 - \cos(\omega_\alpha (\tau + T))] \} \quad (2.37)$$

The experimental time trace becomes:

$$V'_{3P}(\tau, T) = \exp\left(\frac{-T}{T_M^N}\right) \exp\left(\frac{-2\tau}{T_M}\right) \quad (2.38)$$

where  $T_M^N$  is the nuclear phase memory time which is usually of the same order of magnitude of the longitudinal relaxation time  $T_1$  of electron spins. Since the relaxation time  $T_1$  is larger than  $T_m$  of the electron spins, 3P-ESEEM spectra are characterized by narrower lines in the frequency-domain pattern providing increased spectral resolution. Besides, no combination frequencies  $\nu_{+,-}$  are observed so that the appearance of the spectrum is simplified in comparison to the corresponding two-pulse experiment. Nonetheless, from the  $\tau$ -dependent cosine terms in Equation 2.37, 3P-ESEEM spectra are subjected to the presence of blind-spots at  $\nu_{\alpha,\beta}$  when  $\tau = 2\pi n / \nu_{\beta,\alpha}$ , because of the time delay  $\tau$  between the first two pulses. Therefore, it is mandatory to perform measurements at different  $\tau$  values to retrieve the overall signal, resulting in a more time consuming experiment.

Both 2P- and 3P-ESEEM have the drawback of one-dimensionality (1D) which

may cause possible overlap of signals. Besides, powder spectra are typically characterized by broad lines due to anisotropic hfi and related distribution of  $\nu_{\alpha,\beta}$ . Indeed, the modulation decays very rapidly in time domain of 1D experiments (defocusing of nuclear coherences) and cannot be detected in Fourier transformed spectra anymore. The Hyperfine Sublevel CORrElation (HYSCORE) experiment<sup>98</sup> overcome such problems. By adding a mixing  $\pi$  pulse between the second and third  $\pi/2$  pulse of the 3P-ESEEM experiment and varying independently the two inter-pulse delays,  $t_1$  and  $t_2$ , a two-dimensional (2D) time delay array is produced. The HYSCORE pulse sequence is illustrated in Figure 2.3c and can be written as:  $\pi/2 - \tau - \pi/2 - t_1 - \pi - t_2 - \pi/2 - \tau - echo$ . The nuclear coherence generated by the first two  $\pi/2$  pulses undergoes free evolution during  $t_1$  with frequency  $\nu_\alpha$ . Thus, the mixing  $\pi$  pulse transfers populations in one  $m_s$  spin manifold to the other and similarly transfers the nuclear coherence between manifolds so that it evolves with frequency  $\nu_\beta$  during time  $t_2$ . Fourier transformation of the time-domain data along the two dimensions ( $t_1$  and  $t_2$ ) leads to 2D frequency-domain spectrum where cross-peaks correlate nuclear transition frequencies from the different  $m_s$  manifolds. Since strong cross-peaks can only be observed between NMR frequencies of the same nucleus, HYSCORE spectra can be slightly simplified compared to 3P-ESEEM. Moreover, the refocusing of nuclear coherences allows the detection of those broad lines usually present in 1D spectra, which appear as ridges in 2D HYSCORE spectra. However, since HYSCORE experiments involve detection of a stimulated echo, they are affected by  $\tau$ -dependent blind-spots, as described for 3P-ESEEM. Such disadvantage can be turned into an advantage as by carefully choosing the  $\tau$  values it is possible to suppress certain spectral feature in order to analyze others.<sup>99</sup>

Simulated HYSCORE spectra for a powder system with  $S=1/2$  and  $I=1/2$  are reported in Figure 2.4. In the weak coupling regime ( $|A| < 2\nu_L$ ), cross peaks are located in the (+,+) quadrant, while for the strong coupling case ( $|A| > \nu_L$ ) the signals appear in the (-,+) quadrant. This facilitates the interpretation for systems containing many interacting nuclei. For single crystal samples, the cross-peaks appear as sharp off-diagonal peaks. For polycrystalline systems the correlation peaks broaden into ridges which represent the sum of the cross-peaks corresponding to specific orientations excited at a distinctive magnetic field position. Therefore, experiments at various magnetic fields need to be performed to excite several molecular orientations and extract the full hyperfine and/or nuclear quadrupole tensors.

In the limit of the point dipole approximation, the anisotropy of the dipolar hyperfine interaction ( $T$ ) can be determined from the maximum curvature of

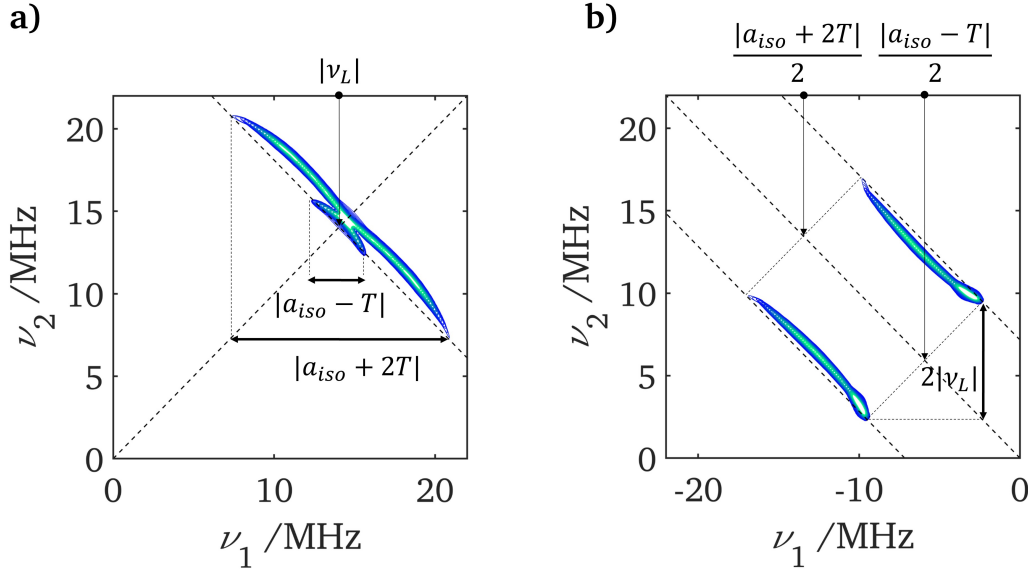


**Figure 2.4:** Simulated HYSCORE powder patterns for a  $S=1/2$ ,  $I=1/2$  spin system with an axial hyperfine tensor. a) Weak-coupling case with  $\nu_L=14$  MHz,  $a_{iso}=2.5$  MHz and  $T=6$  MHz. b) Strong-coupling case with  $\nu_L=3.5$  MHz,  $a_{iso}=18$  MHz and  $T=6$  MHz.  $\nu_L$  is the Larmor frequency for the nucleus of interest. Adapted from Ref.<sup>100</sup>

the ridges away from the anti-diagonal:<sup>31</sup>

$$\nu_{max} = \frac{9T^2}{32|\nu_L|} \quad (2.39)$$

The magnitude of  $a_{iso}$  can be found from the ridge end points or from simulations.

### 2.3.3 ENDOR techniques

Electron-Nuclear DOuble Resonance (ENDOR) spectroscopy exploits a different approach for measuring hyperfine and nuclear quadrupole interactions. Unlike the ESEEM techniques, in ENDOR both microwave and radiofrequency (RF) waves are employed for manipulating the electron and nuclear spins respectively. In an ENDOR experiment, a microwave field changes the populations of the levels involved in an EPR transition, while a radiofrequency field induces nuclear spin transitions thus altering the populations of the energy levels. The amplitude of the electron spin-echo is then subsequently measured as a function of the applied RF. The two standard and most used pulse ENDOR sequences are Davies<sup>101</sup> and Mims ENDOR.<sup>102</sup> Since in this work only Davies ENDOR se-

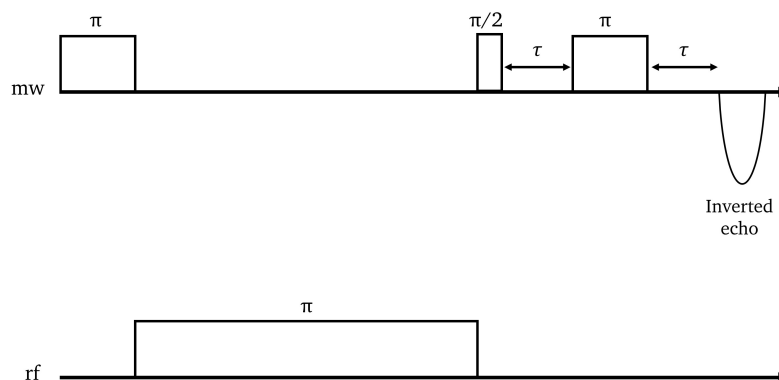


**Figure 2.5:** Davies ENDOR pulse sequence.

quences were employed, a brief description of this technique is given in the following. For a detailed overview of ENDOR techniques the reader is referred to elsewhere.<sup>103</sup>

The Davies ENDOR sequence, written as  $\pi_{MW} - \pi_{RF} - \pi/2_{MW} - \tau - \pi_{MW} - \tau - echo$ , is shown in Figure 2.5. A selective (weak)  $\pi$  microwave pulse polarizes the electronic population of one of the allowed EPR transitions. A radiofrequency pulse is applied, which inverts the population of one of the NMR transitions. The radiofrequency is swept and when the resonance with the nuclear transition is fulfilled, the echo will be less polarized, producing the ENDOR spectrum.

An important requirement of Davies ENDOR is that the first  $\pi_{MW}$  pulse only excites one of the allowed EPR transitions of each spin packets. Under these conditions, the inversion  $\pi_{MW}$  pulse acts as a filter for small hyperfine couplings. This filter can be adjusted by varying the length and thus bandwidth of the MW inversion  $\pi_{MW}$  pulse. The bandwidth, defined as full width at half height (in Hz), of a rectangular MW pulse of length  $t_p$  is given by:

$$\Delta\nu \approx \frac{1}{1.6578 \times t_p} \quad (2.40)$$

The absolute ENDOR intensity as a function of the selectivity of the inversion

$\pi_{MW}$  pulse is given by:<sup>104</sup>

$$V(\eta_s) = V_{\max} \frac{\sqrt{2}\eta_s}{\eta_s^2 + 1/2} \quad (2.41)$$

with

$$\eta_s = \frac{t_\pi a_{iso}}{2\pi} \quad (2.42)$$

Here,  $V_{\max}$  is the maximum ENDOR intensity obtained when  $\eta_s = \sqrt{2}/2$ ,  $t_\pi$  the length of the preparation  $\pi_{MW}$  pulse, and  $a_{iso}$  the observed hyperfine coupling (in radians). This filtering technique is often very valuable as it allows to suppress the ENDOR signal from weakly coupled nuclei that may overlap with signal from strongly coupled nuclei by using relatively hard  $\pi_{MW}$  preparation pulse. Finally, it is worth noting that the ENDOR technique provides complementary information to ESEEM spectroscopy and it is particularly powerful for detecting high frequency couplings, especially dominated by isotropic contributions.

## 2.4 EPR spectroscopy of monomeric Cu<sup>II</sup> species

Monomeric Cu<sup>II</sup> ions possess a  $3d^9$  electronic configuration where the 9  $d$  electrons are always maximally paired to give a total spin  $S=1/2$ . The dominating EPR interactions are the electron Zeeman interaction and the hyperfine interaction of the unpaired electron with  $^{63,65}\text{Cu}$  isotopes (natural abundance of  $^{65}\text{Cu}$  isotope is 30.83%). Although such information are recovered by CW-EPR, the metal-ligand interactions remain unresolved. Indeed, the hyperfine interactions with ligands cannot be resolved through CW-EPR experiments in most cases: the expected splitting of the EPR line in  $\prod_n (2nI + 1)$  lines due to the electron spin interacting with  $n$  nuclear spins  $I$ , is usually not easily recognized and only broad signals are observed.<sup>82</sup>

### 2.4.1 Influence of the ligand field splitting on EPR spectra

The  $g$ -tensor components of Cu<sup>II</sup> species strongly depend on the local symmetry experienced by the cation. Due to the direction of the five  $d$ -orbitals ( $d_{x^2-y^2}$ ,  $d_{xz}$ ,  $d_{yz}$ ,  $d_{xy}$  and  $d_{z^2}$ ), the ligands surrounding the Cu<sup>II</sup> ion cause these orbitals to split into groups with different energy. The entity of the energy splittings depend on the nature of the ligands and their arrangement around the metal ion. In the simplest case, Cu<sup>II</sup> ion possesses an octahedral coordination by binding six ligands (L) placed on the Cartesian axes forming a perfect octahedron ( $O_h$  point group symmetry). The electrostatic field created by these ligands destabilizes the orbitals and removes the five-fold degeneracy of the  $d$  orbitals by splitting

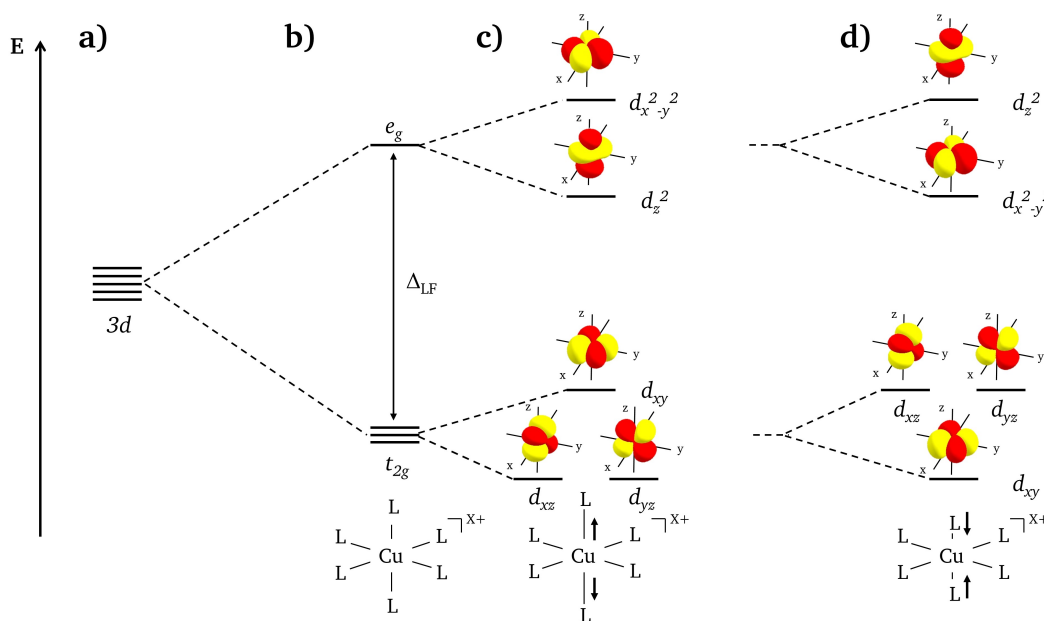


**Figure 2.6:** Splitting of the  $d$  orbitals in: a) free ion, b) octahedral ligand field, tetragonal distorted ligand field caused by elongation c) and d) compression along the  $z$  axis.

them in two degenerate levels. The energy of the  $e_g$  set is raised compared to the  $t_{2g}$  set because the  $d_{z^2}$  and  $d_{x^2-y^2}$  orbitals point directly to the ligands, whereas the remaining orbitals point between these ligands. The energy difference between these two sets depends on the strength of the ligand field ( $\Delta_{LF}$ ). The orbital degeneracy is further removed due to the Jahn-Teller effect.<sup>105</sup> This leads to a tetragonal distortion which produces a system with lower symmetry (from  $O_h$  to  $D_{4h}$ ), either by elongation or compression along the  $z$  axis.<sup>82,83</sup>

In the former case, the unpaired electron resides in the  $d_{x^2-y^2}$  orbital, which becomes the highest occupied orbital in energy, as depicted in Figure 2.6c. The missing electron can be seen as a "hole". Spin-orbit coupling causes the unpaired "hole" to admix with orbitals, other than  $d_{x^2-y^2}$ , reintroducing orbital angular momentum. The admixture of  $d$  orbitals depends on the symmetry of the coupled states. The application of magnetic field orthogonal to either  $x$ ,  $y$  or  $z$  axes induces motion between states having the correct symmetry. This corresponds to a rotation of the electron about that axis. For a  $D_{4h}$  symmetry, rotations around the  $z$  axes belong to the irreducible representation  $A_{2g}$ , while rotations around  $x$  and  $y$  axes belong to the irreducible representation  $E_g$ . The  $d_{x^2-y^2}$  orbital has  $B_{1g}$  symmetry. Hence, when the magnetic field is aligned along the  $z$  axis (symmetry  $A_{2g}$ ), the  $d_{x^2-y^2}$  (symmetry  $B_{1g}$ ) can mix with the  $d_{xy}$  orbital (symmetry  $B_{2g}$ ) because of the product  $B_{1g} \times A_{2g} = B_{2g}$ . The magnitude

of the resulting  $g$  value is given by:

$$g_{zz}(g_{\parallel}) = g_e + \frac{8\lambda}{E_{(x^2-y^2)} - E_{xy}} \quad (2.43)$$

where  $\lambda$  is the spin-orbit coupling constant ( $828 \text{ cm}^{-1}$  for  $\text{Cu}^{\text{II}}$ ).<sup>106</sup>

On the other hand, when the magnetic field is parallel to the  $xy$  plane, this will transform according to the irreducible representation  $E_g$ . The product  $B_{1g} \times E_g$  gives  $E_g$  symmetry to which correspond the degenerate  $d_{xz}$  and  $d_{yz}$  orbitals. In this case,  $d_{x^2-y^2}$  mixes with  $d_{xz}$  or  $d_{yz}$  orbital and the corresponding  $g$  values is:

$$g_{xx,yy}(g_{\perp}) = g_e + \frac{2\lambda}{E_{(x^2-y^2)} - E_{xz,yz}} \quad (2.44)$$

Because of the energetic difference of the  $E_0 - E_n$  states in Equations 2.43 and 2.44, anisotropic  $g$  values are obtained, both larger than  $g_e$ .<sup>82,83</sup>

As soon as the symmetry of the metal complex changes, the ligand field splitting also changes and thus different  $g$  values are observed. When the  $\text{Cu}^{\text{II}}$  ion experiences compression along  $z$  axis, the unpaired electron dwells in the  $d_{z^2}$  orbital, the highest in energy among the  $d$  orbitals for such geometry (see Figure 2.6d). The  $d_{z^2}$  orbital belongs to the  $A_{1g}$  irreducible representation. When the magnetic field is applied along  $z$  axis, this orbital does not mix with any other orbitals since  $A_{1g} \times A_{2g} = A_{2g}$ , so that  $g_{zz} = g_e$ . However, when the magnetic field is parallel to the  $xy$  plane,  $A_{1g}$  couples with  $E_g$  states, giving a  $E_g$  state. The expression for the  $g_{xx,yy}$  is:

$$g_{xx,yy}(g_{\perp}) = g_e + \frac{6\lambda}{E_{(z^2)} - E_{xz,yz}} \quad (2.45)$$

In this case, the predicted order for the  $g$  values is  $g_{\perp} > g_{\parallel} > g_e$ .<sup>82,83</sup>

The removal of the two axial ligands (aligned along the  $z$  axis) leads the  $\text{Cu}^{\text{II}}$  ion to a square planar arrangement, resulting in considerable stabilization of the  $d_{z^2}$  orbital and destabilization of the  $d_{xy}$  (see Figure 2.7). Nonetheless, the square planar geometry behaves according to the  $D_{4h}$  symmetry, enabling the same kind of states admixture discussed for the tetragonally elongated complex. Once again, since the energy difference of the  $E_0 - E_n$  states changes, the  $g$  values for square planar geometry also changes.

The anisotropic part of the  $\mathbf{A}$ -tensor associated to the  $\text{Cu}^{\text{II}}$  nucleus is also dependent on the symmetry and crystal field. Simplified theoretical expressions for the copper hyperfine couplings  $A_{zz}(A_{\parallel})$  and  $A_{xx,yy}(A_{\perp})$  when the unpaired



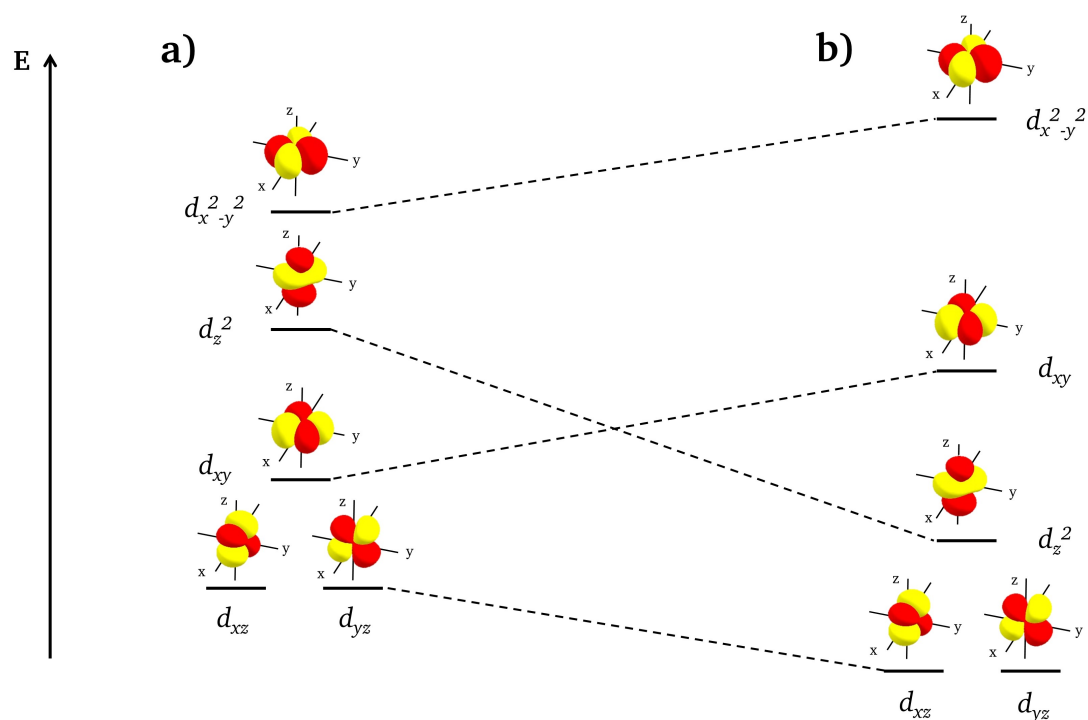


**Figure 2.7:** Splitting of the  $d$  orbitals in: a) six-coordinated Cu<sup>II</sup> complex with a tetragonal distortion (elongation along  $z$  axis). b) square planar Cu<sup>II</sup> complex obtained after the removal of the two axial ligands.

electron dwells in the  $d_{x^2-y^2}$  orbital are given by:<sup>86</sup>

$$A_{zz}(A_{\parallel}) = P \left[ -\kappa + \Delta g_{zz} - \frac{4}{7}\alpha^2 + \frac{3}{7}\Delta g_{xx} \right] \quad (2.46)$$

$$A_{xx,yy}(A_{\perp}) = P \left[ -\kappa + \frac{2}{7}\alpha^2 - \frac{11}{14}\Delta g_{xx} \right] \quad (2.47)$$

where  $\Delta g_{zz} = g_{\parallel} - g_e$  and  $\Delta g_{xx} = g_{\perp} - g_e$ ,  $P$  is the dipolar hyperfine coupling and depends on the metal ion ( $P_{\text{Cu}} = 1171$  MHz). The terms containing  $\alpha^2$  arise from dipole–dipole interactions between the magnetic moments associated with the spin motion of the electron and nucleus. As the unpaired electron is more delocalized onto the surrounding ligands, this contribution to  $\alpha^2$  is reduced.  $\kappa$  arises from the Fermi contact interaction that has its origin in a nonvanishing probability of finding the unpaired electron at the site of the nucleus. A similar set of equations can be derived when the unpaired electron resides in the  $d_{z^2}$  orbital:<sup>86</sup>

$$A_{zz}(A_{\parallel}) = P \left[ -\kappa + \frac{4}{7}\alpha^2 - \frac{1}{7}\Delta g_{xx} \right] \quad (2.48)$$

$$A_{xx,yy}(A_{\perp}) = P \left[ -\kappa + \frac{2}{7}\alpha^2 + \frac{15}{14}\Delta g_{xx} \right] \quad (2.49)$$

### 2.4.2 Interpretation of EPR signals of isolated $\text{Cu}^{\text{II}}$ species

In Figure 2.8 are shown four examples of typical CW-EPR powder spectra of  $\text{Cu}^{\text{II}}$  ions experiencing different coordination geometries. By moving from elongated octahedral (Figure 2.8a) to square planar (Figure 2.8c) geometry, the  $g_{\parallel}$  value decreases (shifting towards higher magnetic field) due to higher energy splitting between the  $d_{x^2-y^2}$  and the  $d_{xy}$  orbitals (see also Equation 2.43). On the other hand, the  $A_{\parallel}$  value is higher in a square planar complex with respect to a tetragonally distorted octahedral one because of the different contribution of the  $g_{zz}$  values in Equation 2.46. The spectrum in Figure 2.8d behaves differently and it shows an inverted  $g$ -tensor ( $g_{\perp} > g_{\parallel}$ ) due to the  $d_{z^2}$  ground state. This simple example illustrates how diagnostic the  $g_{\parallel}$  and  $A_{\parallel}$  values can be for the prediction of structure, symmetry and electronic properties of  $\text{Cu}^{\text{II}}$  ions.<sup>81–83,86</sup>

The trends of  $g_{\parallel}$  and  $A_{\parallel}$  can also be very informative on the nature of the coordinated ligands for many square planar  $\text{Cu}^{\text{II}}$  systems. The pioneering work of Peisach and Blumberg demonstrated this empirical correlation for several  $\text{Cu}^{\text{II}}$  containing biological systems through the so-called *Peisach-Blumberg* plots.<sup>107</sup> For instance, a systematic change in  $g_{\parallel}$  and  $A_{\parallel}$  is expected for  $\text{Cu}^{\text{II}}$  ion coordinated by four nitrogen donor ligands compared to two nitrogen plus two oxygen donors, or four oxygens (Cu-porphyrin or Cu-acetylacetonate complexes).

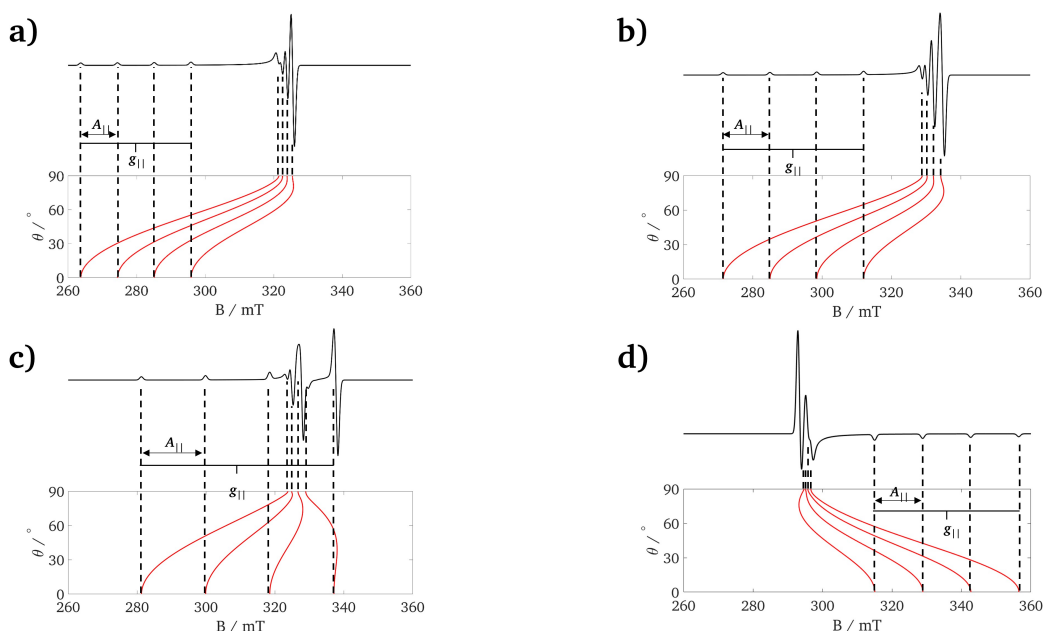


**Figure 2.8:** Simulated CW-EPR powder spectra of Cu<sup>II</sup> species in tetragonally distorted crystal field (in black) together with the angular variation in resonant field ( $B_{res}$ ) as a function of the spherical polar angle  $\theta$  (in red). a) elongated octahedral, b) square pyramidal, c) square planar and d) trigonal bipyramidal geometries. The spectra were simulated by using a frequency of  $\nu = 9.4$  GHz.

Such plots may also be successfully used for the interpretation of EPR spectra of copper-exchanged zeolites.<sup>108</sup> An example of how these plots can be interpreted is given in Figure 2.9. All of the dehydrated zeolites are almost perfectly located on the antidiagonal of the plot. This means that generally, for the same coordinating atom type and number (e.g. four equatorial oxygen donor atoms), a Cu<sup>II</sup> ion surrounded by a more negative coordination sphere is found in the upper-left part of the plot whereas, in the opposite case, it is found in the lower-right. For instance, Cu-MFI zeolite hosts two distinct copper species named as MF1 and MF2 in Figure 2.9. MF2 was assigned to a six-membered ring site with two Al whereas MF1 was assigned to a six-membered ring site in which one Al is inside the ring while the other one bridges the ring.<sup>30</sup> Since the latter environment produces a more negative charge on the Cu<sup>II</sup> ion, the parameters related to this site appear in the higher left hand part of the plot. Regarding the hydrated Cu-zeolites, their position on the bottom right hand side is due to the different number and nature of ligands around the copper (i.e., water molecules instead of framework atoms). To conclude, the Peisach–Blumberg approach is an additional evidence of how the relation between  $g_{||}$  and  $A_{||}$  values may provide a fundamental understanding of the structure and geometry of Cu<sup>II</sup> systems.

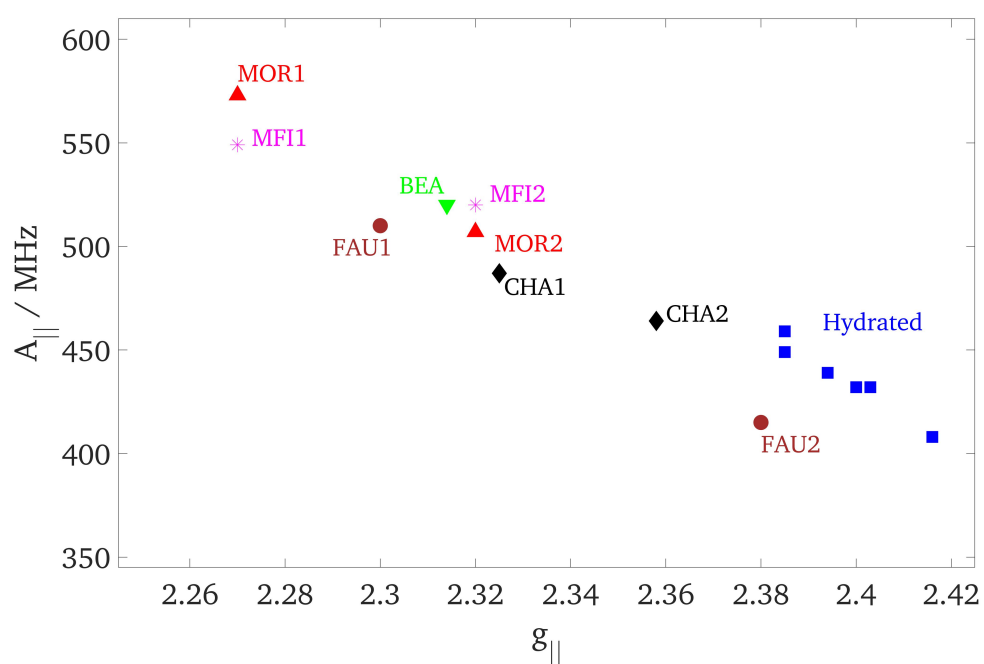


**Figure 2.9:** Peisach-Blumberg plot for different Cu-exchanged zeolites. The data for hydrated Cu-zeolites are given with blue squares and they refer to low temperature measurements. Adapted from Ref.<sup>29</sup>

## Chapter 3

# Quantum chemical modelling

The following chapter provides the fundamental theory of the quantum chemical approaches employed in this thesis. The first section describes shortly the relationship between the spin Hamiltonian and the many-particle Hamiltonian which leads to closed-form expressions for all EPR parameters. The analytic implementation of such expressions in the framework of the commonly used quantum chemical methods is also outlined. Subsequently, the two quantum chemical approximations exploited in this work are briefly reviewed. Finally, the strategy used to accurately model microporous systems such as zeolites is depicted. For a detailed description of the quantum chemical methods and theory illustrated in this chapter, the reader is referred to several textbooks and articles.<sup>68,109–113</sup>

### 3.1 Quantum chemical calculation of EPR parameters

The properties of molecules are described by the many-particle Schrödinger equation which can be written as (in its time-independent version):<sup>109</sup>

$$\hat{\mathcal{H}}(\mathbf{x}_1, \dots, \mathbf{x}_N) \Psi_I(\mathbf{x}_1, \dots, \mathbf{x}_N) = E_I \Psi_I(\mathbf{x}_1, \dots, \mathbf{x}_N) \quad (3.1)$$

where  $I = 0, \dots, \infty$  indicates the electronic states of the system,  $\Psi$  is the electronic wavefunction which depends on the electronic coordinates  $\mathbf{x}_i$  containing the three spatial coordinates  $\mathbf{r}$  and one spin coordinate  $\sigma_i$  of the  $i$ 'th electron. The Hamiltonian operator  $\hat{\mathcal{H}}$  consists of all the terms that contribute for the total energy of the system. Usually it is divided into a relativistic part, a nonrelativistic part and a part describing the interaction of the particles with external fields. The nonrelativistic Hamiltonian within the Born-Oppenheimer (BO) ap-

proximation (frozen nuclei) is expressed in atomic units as:

$$\hat{\mathcal{H}}_{BO} = \underbrace{-\frac{1}{2} \sum_i \nabla_i^2}_{\hat{T}_e} - \underbrace{\sum_{A,i} \frac{Z_A}{r_{A,i}}}_{\hat{V}_{eN}} + \underbrace{\frac{1}{2} \sum_{i \neq j} \frac{1}{r_{i,j}}}_{\hat{V}_{ee}} + \underbrace{\frac{1}{2} \sum_{A \neq B} \frac{Z_A Z_B}{R_{AB}}}_{\hat{V}_{NN}} \quad (3.2)$$

where  $i, j$  are the electronic coordinates and  $A, B$  the nuclear coordinates.  $Z_A$  is the charge of nucleus  $A$ ,  $r_{Ai}$  is the distance of the  $i$ 'th electron to the  $A$ 'th nucleus and analogous for  $r_{ij}$  and  $R_{AB}$ . The first two terms in Equation 3.2 are attractive and describe the electron kinetic energy ( $\hat{T}_e$ ) and the coulombic electron-nuclei interaction ( $\hat{V}_{eN}$ ), whereas the other two terms are repulsive and describe the electron-electron ( $\hat{V}_{ee}$ ) and nuclei-nuclei ( $\hat{V}_{NN}$ ) coulombic interactions. The eigenfunctions of the BO Hamiltonian are characterized by the quantum number  $S$  and  $M$ , where  $S$  is the total spin of the system and  $M$  is its projection onto the  $z$  axis. The related time-independent BO Schrödinger equation cannot be solved in closed form and it is necessary to approximate its solution, as it will be shown in the following section.

If one assume to know the exact solution of the BO Schrödinger equation, then it is possible to introduce further terms in the Hamiltonian arising from the theory of relativity.<sup>111</sup> A comprehensive treatment of the relativistic many-particle Schrödinger equation is not possible here and details are provided elsewhere.<sup>114,115</sup> It is sufficient to point out that the relativistic extension of the Hamiltonian contains a number of terms depending on the electron and nuclear spins and their mutual interaction. The most important spin-dependent term is the spin-orbit coupling (SOC). Its simplest version is given by:

$$\hat{\mathcal{H}}_{SOC} = \frac{\alpha^2}{2} \sum_i \sum_A \frac{Z_A \hat{\mathbf{I}}_{iA} \hat{\mathbf{s}}_i}{r_{iA}^3} - \frac{\alpha^2}{2} \sum_i \sum_{j \neq i} \frac{\hat{\mathbf{I}}_{ij} (\hat{\mathbf{s}}_i + 2\hat{\mathbf{s}}_j)}{r_{ij}^3} \quad (3.3)$$

where  $\hat{\mathbf{s}}_i$  is the spin-operator for the  $i$ 'th electron,  $\alpha \approx \frac{1}{137}$  is the fine structure constant in atomic units,  $\hat{\mathbf{I}}_{iA}$  is the angular momentum operator of the  $i$ 'th electron relative to the  $A$ 'th nucleus,  $\hat{\mathbf{I}}_{ij}$  is the angular momentum operator of the  $i$ 'th electron relative to the  $j$ 'th electron. The SOC operator is thus a sum of an one-electron and a two-electron operator. A good approximation of the SOC operator is given by the spin-orbit mean-field (SOMF) approach which transforms the SOC in a quasi-one-electron form:<sup>116,117</sup>

$$\hat{\mathcal{H}}_{SOMF} = \sum_i \mathbf{z}(\mathbf{r}_i) \hat{\mathbf{s}}_i \quad (3.4)$$

where  $\mathbf{z}(\mathbf{r}_i)$  contains three spatial components.

Subsequently, the terms that depend on external fields are considered. In particular, one must take in account the terms that couple the electrons to the magnetic field given by:

$$\hat{\mathcal{H}}_{SB+LB} = \beta_e \mathbf{B}_0 \sum_i \left( \hat{\mathbf{I}}_i + g_e \hat{\mathbf{s}}_i \right) \quad (3.5)$$

The angular momentum operator  $\hat{\mathbf{I}}_i$  refers to the global origin: this leads to a lack of gauge invariance and the results depend on the choice of the origin. Another important term regards the coupling of the nuclear spin to the electron angular momenta

$$\hat{\mathcal{H}}_{LI} = \beta_e \sum_{i,A} g_n^{(A)} \beta_n \frac{\hat{\mathbf{I}}_{iA} \hat{\mathbf{I}}^{(A)}}{r_{iA}^3} \quad (3.6)$$

where  $g_n^{(A)}$  is the nuclear  $g$ -factor of the  $A$ 'th nucleus. Moreover, the coupling of the nuclear spin to the electron spins is expressed as:

$$\hat{\mathcal{H}}_{SI} = g_e \beta_e \sum_{i,A} g_n^{(A)} \beta_n \left[ \hat{\mathbf{I}}^{(A)} \hat{\mathbf{s}}_i - 3(\hat{\mathbf{s}}_i \mathbf{n}_{iA}) \left( \hat{\mathbf{I}}^{(A)} \mathbf{n}_{iA} \right) \right] \quad (3.7)$$

where  $\mathbf{n}_{iA}$  is a unit vector in the direction of  $\mathbf{R}_A - \mathbf{r}_i$ . At last, the dipole-dipole interaction between the electrons is given by the following expression:

$$\hat{\mathcal{H}}_{DD} = \frac{g_e^2 \alpha^2}{8} \sum_{i \neq j} \frac{\hat{\mathbf{s}}_i \hat{\mathbf{s}}_j - 3(\hat{\mathbf{s}}_i \mathbf{n}_{ij})(\hat{\mathbf{s}}_j \mathbf{n}_{ij})}{r_{ij}^3} \quad (3.8)$$

with  $\mathbf{n}_{ij}$  being the unit vector pointing from the electron  $i$  to the electron  $j$ . Both the isotropic and anisotropic contribution to the hyperfine interaction arise from  $\hat{\mathcal{H}}_{DD}$  operator. By neglecting other small terms,<sup>114</sup> all the interactions described in Equations 3.4, 3.5, 3.6, 3.7 and 3.8 may be collected in a perturbing Hamiltonian  $\hat{\mathcal{H}}_1$ :

$$\hat{\mathcal{H}}_1 = \hat{\mathcal{H}}_{SOMF} + \hat{\mathcal{H}}_{SB+LB} + \hat{\mathcal{H}}_{LI} + \hat{\mathcal{H}}_{SI} + \hat{\mathcal{H}}_{DD} \quad (3.9)$$

### 3.1.1 Determination of the spin Hamiltonian terms through an effective Hamiltonian

The important task left now is to cleanly connect the effective “true” Hamiltonian  $\hat{\mathcal{H}}_{BO} + \hat{\mathcal{H}}_1$  with the much simpler spin Hamiltonian  $\hat{\mathcal{H}}_{spin}$ .<sup>68</sup> McWeeny<sup>118</sup> was the first to propose a transparent treatment further refined later.<sup>119</sup> By assuming that the ground-state  $\Psi_0^{SM}$  is sufficiently isolated from the remaining excited states  $\Psi_n^{S'M'}$  and that the BO problem has been solved exactly, the eigen-

states of  $\hat{\mathcal{H}}_{BO} + \hat{\mathcal{H}}_1$  can be expanded in terms of the BO eigenfunctions:

$$\Phi_X(\mathbf{x}_1, \dots, \mathbf{x}_N) = \sum_{I,S,M} c_{ISM} \Psi_I^{SM}(\mathbf{x}_1, \dots, \mathbf{x}_N) \quad (3.10)$$

Equation 3.10 emphasizes that the relativistic eigenstates involve, theoretically, all magnetic sublevels of all multiplets with any multiplicity. The coefficients  $c_{ISM}$  can be obtained by means of the variational principle:

$$\mathbf{H}\mathbf{c} = E\mathbf{c} \quad (3.11)$$

in which:

$$\begin{aligned} H_{ISM,JS'M'} &= \langle \Psi_I^{SM} | \hat{\mathcal{H}}_{BO} + \hat{\mathcal{H}}_1 | \Psi_I^{S'M'} \rangle \\ &= \delta_{ISM,JS'M'} E_I + \langle \Psi_I^{SM} | \hat{\mathcal{H}}_1 | \Psi_I^{S'M'} \rangle \end{aligned} \quad (3.12)$$

Considering the well-isolated ground-state, the eigenvalue problem may be partitioned into a “*a*-set” containing only the  $2S+1$  members of the electronic ground state and a “*b*-set” with all the other states. Equation 3.11 becomes:

$$\begin{pmatrix} \mathbf{H}^{aa} & \mathbf{H}^{ab} \\ \mathbf{H}^{ba} & \mathbf{H}^{bb} \end{pmatrix} \begin{pmatrix} \mathbf{c}^a \\ \mathbf{c}^b \end{pmatrix} = E \begin{pmatrix} \mathbf{c}^a \\ \mathbf{c}^b \end{pmatrix} \quad (3.13)$$

The effective nonlinear Hamiltonian is thus given by:

$$[\mathbf{H}^{aa} - \mathbf{H}^{ab}(\mathbf{H}^{bb} - \mathbf{1}^b E)^{-1} \mathbf{H}^{ba}] \mathbf{c}^a = E \mathbf{c}^a \quad (3.14)$$

where  $\mathbf{1}^b$  is the unit matrix in *b*-space. To solve Equation 3.14 it is necessary to make some simplifications. First, the coupling with *b*-states through  $\hat{\mathcal{H}}_1$  may be neglected resulting in  $H_{KL}^{bb} = \delta_{KL} E_K$ ; secondly, the unknown  $E$  in the matrix inverse needs to be replaced by a known energy. A reasonable choice is to use  $E_0$  as known energy. The effective Hamiltonian in *a*-set becomes:

$$\begin{aligned} H_{MM'}^{eff} &= \delta_{MM'} E_0 + \langle \Psi_0^{SM} | \hat{\mathcal{H}}_1 | \Psi_0^{SM'} \rangle \\ &\quad - \sum_{KS'M''} \Delta_K^{-1} \langle \Psi_0^{SM} | \hat{\mathcal{H}}_1 | \Psi_K^{S'M''} \rangle \langle \Psi_K^{S'M''} | \hat{\mathcal{H}}_1 | \Psi_0^{SM'} \rangle \end{aligned} \quad (3.15)$$

with  $\Delta_K = E_K - E_0$ . The ground-state energy in the first term can be dropped since it shifts all levels equally. Apart from the nuclear spin degrees of freedom, the Hamiltonian in Equation 3.15 is of the same dimension as the spin Hamiltonian but it utterly relies on nonrelativistic BO eigenstates.

The explicit expressions for the spin Hamiltonian parameters are determined



by comparing the matrix elements of the effective Hamiltonian with the spin Hamiltonian one-by-one.<sup>119</sup> For example, for the hfi one looks for terms involving electron and nuclear spin. The direct coupling is provided by  $\hat{\mathcal{H}}_{SI}$  and, thus, it is a first-order contribution. On the contrary, the cross products of  $\hat{\mathcal{H}}_{LI}$  and  $\hat{\mathcal{H}}_{SOMF}$  are also proportional to  $S$  times  $I$  and, hence, there have also a contribution from the final, infinite sum over states (SOS) term that represents a second-order contribution. The  $\mathbf{g}$ -matrix arises from second-order terms between  $\hat{\mathcal{H}}_{SOMF}$  and  $\hat{\mathcal{H}}_{SB+LB}$  while the zfi arises from the first order term  $\hat{\mathcal{H}}_{SS}$  and the second-order term arising from twice  $\hat{\mathcal{H}}_{SOMF}$ .

The final expressions for the spin Hamiltonian parameters read:<sup>68,74,119</sup>

$$\mathbf{g} = \mathbf{g}^{(SB)} + \mathbf{g}^{(RMC)} + \mathbf{g}^{(GC)} + \mathbf{g}^{(OZ/SOC)} \quad (3.16)$$

$$\mathbf{A}^{(A)} = \mathbf{A}^{(FC;A)} + \mathbf{A}^{(SD;A)} + \mathbf{A}^{(SOC;A)} \quad (3.17)$$

$$\mathbf{D} = \mathbf{D}^{(SS)} + \mathbf{D}^{(SOC-(0))} + \mathbf{D}^{(SOC-(+1))} + \mathbf{D}^{(SOC-(-1))} \quad (3.18)$$

where the labels mean:  $SB$  is the first-order free electron  $g$ -value contribution to the  $\mathbf{g}$ -matrix;  $RMC$  is the relativistic mass correction;  $GC$  is the gauge correction;  $OZ/SOC$  is the second-order contribution from orbital Zeeman and SOC;  $FC$  is the Fermi contact;  $SD$  stands for spin-dipole;  $(SOC; A)$  is the spin-orbit contribution to the hyperfine coupling of nucleus  $A$ ;  $SOC$  is the second-order SOC contribution to the zfi;  $SS$  is the first-order spin-spin contribution to the zfi. The individual components composing the expressions for  $\mathbf{g}$ - and  $\mathbf{A}$ -matrices (Equations 3.16 and 3.17) are:<sup>68</sup>

$$g_{KL}^{(SB)} = \delta_{KL} g_e \quad (3.19)$$

$$g_{KL}^{(RMC)} = \delta_{KL} \frac{\alpha^2}{2} \frac{1}{S} \frac{g_e}{2} \left\langle \Psi_0^{SS} \left| \sum_i \nabla_i^2 \hat{s}_{z;i} \right| \Psi_0^{SS} \right\rangle \quad (3.20)$$

$$g_{KL}^{(GC)} = \frac{1}{S} \left\langle \Psi_0^{SS} \left| \sum_{i,A} \xi(r_{iA}) \{ \mathbf{r}_{iA} \mathbf{r}_i - r_{iA;K} r_{i;L} \} s_{z;i} \right| \Psi_0^{SS} \right\rangle \quad (3.21)$$

$$\begin{aligned} g_{KL}^{(OZ/SOC)} = & -\frac{1}{S} \sum_{b(S_b=S)} \Delta_b^{-1} \left\{ \left\langle \Psi_0^{SS} \left| \sum_i \hat{l}_{i,K} \right| \Psi_b^{SS} \right\rangle \times \left\langle \Psi_b^{SS} \left| \sum_i z_{L;i} \hat{s}_{z;i} \right| \Psi_0^{SS} \right\rangle \right. \\ & \left. + \left\langle \Psi_0^{SS} \left| \sum_i z_{K;i} \hat{s}_{z;i} \right| \Psi_b^{SS} \right\rangle \times \left\langle \Psi_b^{SS} \left| \sum_i \hat{l}_{i,L} \right| \Psi_0^{SS} \right\rangle \right\} \quad (3.22) \end{aligned}$$

$$A_{KL}^{(FC;A)} = \delta_{KL} \frac{8\pi}{3} \frac{1}{S} \beta_e g_e \beta_n^{(A)} g_n^{(A)} \left\langle \Psi_0^{SS} \left| \sum_i \delta(r_{iA}) \hat{s}_{z;i} \right| \Psi_0^{SS} \right\rangle \quad (3.23)$$

$$A_{KL}^{(SD;A)} = \frac{1}{S} \beta_e g_e \beta_n^{(A)} g_n^{(A)} \times \left\langle \Psi_0^{SS} \left| \sum_i \hat{s}_{z;i} r_{iA}^{-5} \{ \delta_{KL} r_{iA}^2 - 3r_{iA;K} r_{iA;L} \} \right| \Psi_0^{SS} \right\rangle \quad (3.24)$$

$$A_{KL}^{(SOC;A)} = -\frac{1}{S} \beta_e g_e \beta_n^{(A)} g_n^{(A)} \sum_{b(S_b=S)} \Delta_b^{-1} \left\{ \left\langle \Psi_0^{SS} \left| \sum_i \frac{\hat{l}_{i;K}^{(A)}}{r_{iA}^3} \right| \Psi_b^{SS} \right\rangle \right. \\ \times \left\langle \Psi_b^{SS} \left| \sum_i z_{L;i} \hat{s}_{z;i} \right| \Psi_0^{SS} \right\rangle + \left\langle \Psi_0^{SS} \left| \sum_i z_{K;i} \hat{s}_{z;i} \right| \Psi_b^{SS} \right\rangle \\ \left. \times \left\langle \Psi_b^{SS} \left| \sum_i \frac{\hat{l}_{i;L}^{(A)}}{r_{iA}^3} \right| \Psi_0^{SS} \right\rangle \right\} \quad (3.25)$$

Two main conclusions may be extracted from these equations. First, the second-order terms contain an infinite sum over excited states that, in practice, cannot be performed. Secondly, the  $g$ -matrix is not gauge invariant since the angular momentum operator is referred to a global origin. This latter problem can be circumvented by making the basis functions used in the calculation magnetic field dependent (so-called *gauge-including atomic orbitals*, GIAOs) by including a magnetic field dependent phase factor.<sup>120,121</sup>

### 3.1.2 Linear response approach

The main problem with the theory described above, besides the unavailability of the exact BO eigenfunctions, is the infinite SOS in the second-order contributions to the effective Hamiltonian. In order to come to an equivalent but more practical formulation promptly applied to approximate electronic structure methods, a perturbing one-electron Hamiltonian may be written as:

$$\lambda \hat{\mathcal{H}}_\lambda = \lambda \sum_i \hat{h}_\lambda(x_i) \quad (3.26)$$

where  $\lambda$  is the perturbation parameter and  $\hat{\mathcal{H}}_\lambda$  is some perturbing one-electron operator (any of the terms in Equation 3.9). Equation 3.26 can be rewritten by

introducing Fermion creation and annihilation operators ( $a_p^+$  and  $a_q$ ).

$$\lambda \hat{\mathcal{H}}_\lambda = \lambda \sum_{pq} h_{pq}^{(\lambda)} a_p^+ a_q \quad (3.27)$$

In a nutshell, the operator  $a_p^+ a_q$  replaces orbital  $q$  with orbital  $p$  provided the state that it acts on is a state where  $q$  is occupied and  $p$  is unoccupied. Otherwise it will give zero. By adding this Hamiltonian to the BO Hamiltonian, the ground-state energy can be expanded in a Taylor series:

$$E_0(\lambda) = E_0(0) + \lambda \left. \frac{\partial E_0}{\partial \lambda} \right|_{\lambda=0} + \dots \quad (3.28)$$

By making use of the Hellmann-Feynman theorem:<sup>122</sup>

$$\left. \frac{\partial E_0}{\partial \lambda} \right|_{\lambda=0} = \left\langle \Psi_0 \left| \sum_{pq} h_{pq}^{(\lambda)} a_p^+ a_q \right| \Psi_0 \right\rangle = \sum_{pq} h_{pq}^{(\lambda)} \langle \Psi_0 | a_p^+ a_q | \Psi_0 \rangle = \sum_{pq} h_{pq}^{(\lambda)} D_{pq} \quad (3.29)$$

where the last equality defines the reduced density matrix  $D_{pq}$  of the electronic ground state and thus the expectation value of any one-electron operator of the ground state. Equation 3.29 establishes that the first derivative of the ground-state energy with respect to the perturbation parameter  $\lambda$  is equivalent to first-order perturbation theory and merely involves the expectation value of the perturbation over the ground-state wavefunction. Introducing a second perturbation  $\mu$ :

$$\hat{\mathcal{H}}_\mu = \lambda \mu \sum_{pq} h_{pq}^{(\mu)} a_p^+ a_q \quad (3.30)$$

Finally, there might be mixed terms of the form:

$$\hat{\mathcal{H}}_{\lambda\mu} = \lambda \mu \sum_{pq} h_{pq}^{(\lambda,\mu)} a_p^+ a_q \quad (3.31)$$

where the derivatives become:

$$\frac{\partial^2 E_0}{\partial \lambda \partial \mu} = \sum_{pq} h_{pq}^{(\lambda,\mu)} D_{pq} + \sum_{pq} h^{(\lambda)} \frac{\partial D_{pq}}{\partial \mu} \quad (3.32)$$

The first term is merely the expectation value of the second derivative of the Hamiltonian with respect to both perturbations: it corresponds precisely to the first-order term in the effective Hamiltonian. The derivative of the density matrix is:

$$\frac{\partial D_{pq}}{\partial \mu} = \left\langle \frac{\partial \Psi_0}{\partial \mu} | a_p^+ a_q | \Psi_0 \right\rangle + \left\langle \Psi_0 | a_p^+ a_q | \frac{\partial \Psi_0}{\partial \mu} \right\rangle \quad (3.33)$$

Since the eigenfunctions of the BO Hamiltonian form a complete set in N-particle space, the derivatives can be expanded in terms of the unperturbed wavefunctions:

$$\left| \frac{\partial \Psi_0}{\partial \mu} \right\rangle = \sum_{n>0} c_n^{(\mu)} |\Psi_n\rangle \quad (3.34)$$

According to first-order perturbation theory:<sup>123</sup>

$$c_n^{(\mu)} = -\frac{\langle \Psi_0 | H_\mu | \Psi_n \rangle}{E_n - E_0} \quad (3.35)$$

Therefore Equation 3.33 becomes:

$$\frac{\partial D_{pq}}{\partial \mu} = -\sum_{n>0} \Delta_n^{-1} \{ \langle \Psi_0 | H_\mu | \Psi_n \rangle \langle \Psi_n | a_p^\dagger a_q | \Psi_0 \rangle + cc \} \quad (3.36)$$

where  $cc$  stands for complex conjugate. By substituting the new form of  $\frac{\partial D_{pq}}{\partial \mu}$  in Equation 3.32, one can writes:

$$\begin{aligned} \frac{\partial^2 E_0}{\partial \lambda \partial \mu} &= \sum_{pq} h_{pq}^{(\lambda, \mu)} D_{pq} + \sum_{pq} h^{(\lambda)} \frac{\partial D_{pq}}{\partial \lambda} \\ &= \langle \Psi_0 | H_{\lambda\mu} | \Psi_0 \rangle - \sum_{n>0} \Delta_n^{-1} \{ \langle \Psi_0 | H_\lambda | \Psi_n \rangle \langle \Psi_n | H_\mu | \Psi_0 \rangle + \langle \Psi_0 | H_\mu | \Psi_n \rangle \langle \Psi_n | H_\lambda | \Psi_0 \rangle \} \end{aligned} \quad (3.37)$$

Equation 3.37 establishes that the second derivative of the ground-state energy is equivalent to the second-order effective Hamiltonian and implicitly contains an infinite sum over states (Equation 3.15). Hence, whatever the approximate method chosen to compute the ground-state energy  $E_0$ , the spin Hamiltonian parameters can be defined as derivatives of this energy. Such approach is referred to as *linear response theory*.<sup>124</sup> For example, the equivalent for the second-order contribution to the  $g$ -matrix (Equation 3.22) in linear response language is:

$$g_{KL}^{(OZ/SOC)} = -\frac{1}{S} \sum_{\mu\nu} \frac{\partial D_{\mu\nu}^{\alpha-\beta}}{\partial B_K} \langle \mu | z_L | \nu \rangle \quad (3.38)$$

where  $D_{\mu\nu}^{\alpha-\beta}$  is the spin-density matrix expressed in terms of the orbital basis set  $\phi_\mu$ . Fortunately, the theory of how to actually take the derivatives of approximate wavefunctions is a highly developed art in quantum chemistry.<sup>125</sup>

It is important mentioning that linear response treatment has some limitations. For instance, if the ground-state multiplet is not well-isolated from the excited state manifold, the perturbation sum will not converge, the response of

the system to the perturbation will become nonlinear and either SOS methods or the linear-response approach fail. This is usually the case of very heavy elements, where the SOC matrix elements reach several thousand wavenumbers and transition metal complexes with orbitally degenerate or nearly degenerate ground states.<sup>126</sup> To date, the only methods that can deal properly with this type of problem are multiconfigurational wavefunction methods.<sup>68</sup>

## 3.2 Electronic structure methods

### 3.2.1 Density Functional Theory

In the many-particle time-independent Schrödinger equation (Equation 3.1) the wavefunction  $\Psi_0$  utterly describes the ground-state of a considered system. Its degrees of freedom are usually very large since  $3N$  spatial and  $N$  spin coordinates of the electrons have to be considered. A different approach in approximating the solution of the BO Schrödinger equation is to consider the electron density  $\rho(r)$ . The electron density  $\rho(r)$  is the probability of finding any of the  $N$  electrons within the volume element  $d\vec{r}_1$  but with arbitrary spin while the other  $N - 1$  have arbitrary spin and positions.<sup>127</sup>

$$\rho(\vec{r}) = N \int \cdots \int |\Psi(\vec{x}_1, \vec{x}_2, \dots, \vec{x}_N)|^2 ds_1 d\vec{x}_2 \dots d\vec{x}_N \quad (3.39)$$

From its definition, electron density is a quantity always positive and its integral over all space is equal to  $N$ . Besides, it is an observable that can be obtained, for instance, from X-ray diffraction. The formal connection between the wavefunction and the electron density is given by the Hohenberg–Kohn theorems.<sup>128</sup> They prove that the exact ground-state energy of a nondegenerate electronic state is a unique (but unknown) functional of just the electron density alone, i.e.,  $E[\rho]$ . Thus, all contributions to the energy can, in principle, be expressed in terms of the density.

$$E[\rho] = \hat{T}_e[\rho] + \hat{V}_{ee}[\rho] + \hat{V}_{ext}[\rho] \quad (3.40)$$

The first two terms of equation 3.40 are in general unknown:  $V_{ee}[\rho]$  is a sum of two terms, the classic Coulombian term  $J[\rho]$  which describes the interaction of the electron density with itself, and a non-classic term  $E_{nc}[\rho]$ , not known. Therefore the total energy functional is:

$$E[\rho] = \hat{T}_e[\rho] + \hat{E}_{nc}[\rho] + \frac{1}{2} \iint \frac{\rho(r_i)\rho(r_j)}{r_{ij}} dr_i dr_j + \int \rho(r)v_{ext}(r) dr \quad (3.41)$$

The real applicability of the Density Functional Theory (DFT) methods is

due to the clever Kohn-Sham formalism.<sup>129</sup> In this approach, the electrons are considered as non-interacting, yet generating an electron density identical to the one of the ground-state for interacting electrons. Therefore, the kinetic term for a non-interacting system is easily defined, the electron nucleus and electron-electron interactions are defined as a functional of  $\rho(\vec{r})$  whereas the kinetic correlation and the quantistic part of the electron-electron interaction are put together in a term known as *exchange-correlation* functional  $E_{XC}[\rho]$ . This term includes exchange and Coulomb correlations, electron kinetics and self-interaction correction. The Kohn-Sham approach leads to an expression that, if  $E_{XC}[\rho]$  is known, is completely exact and gives the exact energy of the ground-state. Moreover, all the energetic functionals become functionals of the Kohn-Sham molecular orbitals  $\phi_\lambda^{KS}$ , thus the minimization procedure is performed over the orbitals that are also functional of the electron density. In this way, pseudo-eigenvalue equations known as Kohn-Sham equations are obtained:

$$\hat{f}^{KS}(i)\phi_\lambda^{KS}(i) = \epsilon_\lambda^{KS}\phi_\lambda^{KS}(i) \quad (3.42)$$

with  $\hat{f}^{KS}$  known as Kohn-Sham operator:

$$\hat{f}^{KS} = -\frac{1}{2}\nabla_i^2 + \hat{V}_{eff}(i) = -\frac{1}{2}\nabla_i^2 - \sum_{a=1}^M \frac{Z_a}{r_{ia}} + \int \frac{\rho(r_j)}{r_{ij}} dr_j + \hat{V}_{XC}[\rho] \quad (3.43)$$

The term  $\hat{V}_{XC}[\rho]$  is the unknown exchange-correlation potential and one has to approximate it. There have been hundreds of proposals on how to accomplish this ( $\approx 300$  density functional approximations). The principles behind the construction of approximate density functionals range from highly formal reasoning to highly parameterized semiempirical approaches.

One of the earliest density functional approximation developed combines the Slater exchange with local density correlation. Such methods is known as “local density” approximation (LDA)<sup>127</sup> and it is still a major workhorse of solid state physics but rarely used in chemistry. A major step forward was the introduction of terms depending on the gradient of the density (“generalized gradient approximation”, GGA).<sup>130</sup> Adding the kinetic energy density defines meta-GGA functionals. Next-step functionals are called hyper-GGA whose the most representative methods of this class are the hybrid functionals: they include part of the exact Hartree-Fock (HF) exchange.<sup>131</sup> The most famous hybrid functional belonging to this class is the B3LYP where the exchange part comes from the B3 functional (Becke-3 parameters)<sup>131</sup> while the correlation part derives from Lee-Yang-Parr (LYP) functional.<sup>132</sup> The functionals of the Minnesota group are based on extensive parameterization and have recently gained popularity in chemistry, most noticeable, M06 and M06-2X.<sup>133</sup> Finally, the last class of density functionals

proposed are known as double-hybrid functionals.<sup>134</sup> They contain, in addition to a fraction of exact exchange, also a fraction of wavefunction based correlation energy calculated from second-order many-body perturbation theory (MPT2).

A general drawback of all common DFT methods is that they cannot describe long-range electron correlations, responsible for van-der Waals (vdW) interactions.<sup>135</sup> The vdW forces are very important since they control the structures of DNA or proteins, formation of aggregates and packing of molecular crystals and microporous systems. The simplest way to account for dispersion interactions is to add a semi-empirical term to the total DFT electron energy:

$$E_{el} = E_{DFT} + E_{disp} \quad (3.44)$$

Different expressions for the  $E_{disp}$  term have been proposed by Grimme and coworkers during the last decades within the frame of the so-called DFT-D methods.<sup>136</sup> For instance, the expression for the so-called D3 scheme is defined as (in case of a molecular systems):

$$E_{disp}^{D3} = - \sum_{AB} \sum_{n=6,8} s_n \frac{C_n^{AB}}{R^n} f_{damp}^{(n)}(R) \quad (3.45)$$

where  $s_n$  scale the individual multipolar contributions.  $f_{damp}^{(n)}(R)$  is a damping function that reduces the dispersion energy to zero at small interatomic separation. Two variants of D3 exist that employ different damping schemes. The original D3 approach employs a damping function proposed by Chai and Head-Gordon,<sup>137</sup> whereas a second damping scheme was combined with the atom pairwise D3 method.<sup>138</sup>

### 3.2.2 The Coupled-Cluster theory

In the HF method<sup>139–141</sup> - which represents the first step of complexity in approximating the solution of BO Schrödinger equation - the  $N$ -particle wavefunction  $\Psi$  is constructed as an antisymmetrized product (Slater determinant) of one-particle wavefunctions (atomic orbitals). In practice, such orbitals are usually expanded in a set of auxiliary functions called basis sets. The variation principle is thus applied to find the shapes of the orbitals that minimize the energy under the constrain that the orbitals remain orthonormal. The energy is always higher than the true ground-state energy. HF theory leads to an energy that is typically around 99.8 % correct. However, the remaining 0.2 % of the energy, namely the correlation energy, is very important for molecular properties and amounts to hundred of kcal mol<sup>-1</sup> since the total energy of an atom or molecule is a large number.

Since the basis set is always larger than the number of electrons in the system, the solution of the HF equations yields a set of occupied orbitals  $\Psi_i$  and unoccupied (virtual) orbitals  $\Psi_a$ . The problem of calculating the correlation energy can be approached by constructing the  $N$ -particle wavefunction as a linear combination of determinants in which a certain number of orbitals are swapped with virtual orbitals from the Hartree–Fock determinant. If this is done to completion and the variational principle applied to solve the many-determinant wavefunction, the resulting method is called Full Configuration Interaction (FCI). It represents the exact solution of the nonrelativistic Schrödinger equation in the given basis set. Approaching the basis set limit of the FCI method yields the exact many-particle wavefunction.

The solution of FCI equations is completely impractical for chemical applications since the computational cost for solving them scales factorially with the number of electrons of the system. Hence, there are many approximate approaches, all of which strive for approaching the FCI limit in the same basis set. Among all the available approaches, there appears to be consensus that Coupled-Cluster (CC) theory is the best way to tackle this problem.<sup>142</sup> CC is based on an exponential Ansatz for the wavefunction

$$|\Psi_0\rangle = \exp(\hat{T})|\Psi_{HF}\rangle \quad (3.46)$$

where  $|\Psi_{HF}\rangle$  is the HF determinant of the ground state.  $\hat{T}$  is the “cluster operator” and it is defined as:

$$\hat{T} = \hat{T}_1 + \hat{T}_2 + \hat{T}_3 + \dots \quad (3.47)$$

where  $\hat{T}_n$  represents all possible  $n$ -fold excitations. For instance, the single ( $\hat{T}_1$ ) and double ( $\hat{T}_2$ ) excitations are defined as:

$$\hat{T}_1 = \sum_{i,a} t_a^i a_a^+ a_i; \quad \hat{T}_2 = \sum_{i,j,a,b} t_{ab}^{ij} a_a^+ a_b^+ a_j a_i \quad (3.48)$$

in which the unknown cluster amplitudes  $t_a^i$  and  $t_{ab}^{ij}$  are determined by solving the CC equations.<sup>142</sup> If  $n = N$ , the CC method converges to the FCI result. Fortunately, convergence with  $n$  is very fast thus the cluster operator can be truncated at low  $n$  while still obtaining an accurate approximation to the FCI result. The Coupled-Cluster with Single-Double (CCSD) defined at  $n = 2$  is an excellent electronic-structure method. Supplementing it with a perturbative correction for the effect of  $\hat{T}_3$  defines the “gold-standard” method of quantum chemistry (CCSD(T)). It has proven countless times to be an excellent approximation to FCI, provided that a single-determinant wavefunction is a good starting point.



Nonetheless, the computational effort to solve the CCSD equations scales as the sixth power of molecular size and CCSD(T) scales as the seventh power. With such steep scaling, solving the problem with ever increasingly powerful hardware can only be successful to a very limited extent. However, great progress has been made in linear-scaling approximations to CCSD(T) which exploit the locality of the dynamic electron correlation.<sup>143</sup> As a result of this, CC theory can now be applied for the calculation of EPR parameters of large molecules with reasonable computational effort.<sup>144,145</sup>

### 3.3 Quantum chemical modelling of solid state systems

Microporous solid systems such as zeolites exhibit a crystalline structure which can be hardly simulated by means of molecular models. Indeed, the finity of a molecular modelling approach may result not reliable since it cannot consider the three-dimensional array of atoms but only a portion of it. Hence, to account for the crystalline structure of a solid, the model of a perfect crystal is usually preferred.<sup>113</sup> Although no real crystal is a perfect crystal, this model is suitable in most cases and, indeed, experimental evidence of crystal periodicity exists in x-ray, neutron, and electron diffraction patterns, which are hardly affected by the presence of the surface, unless the experiment is done in special conditions.

Because a crystal can be regarded as a huge molecule consisting of about as many as Avogadro's number of atoms or ions, calculation of the crystalline electronic structure and properties may appear as an unattainable problem. Fortunately, however, crystals exhibit a very important symmetry property: they are translation invariant by definition.<sup>113</sup> Indeed, a perfect crystal consists of a three-dimensional array of atoms, ions, or molecules, a few of which form a spatial pattern that is repeated identically throughout the crystal. A clever exploitation of this symmetry property makes the computational problem solvable.

Because of symmetry requirements, the Schrödinger equation for a perfect crystal must also be translation invariant which means that, after a translation of the entire crystal by any direct lattice vector  $\mathbf{g}$  the solution of equation:

$$\hat{\mathcal{H}}(\mathbf{r} - \mathbf{g})\Psi(\mathbf{r} - \mathbf{g}) = E\Psi(\mathbf{r} - \mathbf{g}) \quad (3.49)$$

concide with those of Equation 3.1. It has been demonstrated that the eigenfunctions of Equation 3.49 must obey the Bloch theorem<sup>146</sup> and are function of the spatial coordinate in the direct lattice as well as the wave vector  $k$  in the reciprocal lattice. A function that satisfies the Bloch theorem is called Bloch

function and can be written as:

$$\Phi(\mathbf{r} + \mathbf{g}; \mathbf{k}) = \Phi(\mathbf{r}; \mathbf{k})e^{i\mathbf{k} \cdot \mathbf{g}} \quad (3.50)$$

A Bloch function can also be expressed as the product of a plane wave and a periodic function  $u(\mathbf{r}; \mathbf{k})$  with the same periodicity of the lattice:

$$\Phi(\mathbf{r}; \mathbf{k}) = e^{i\mathbf{k} \cdot \mathbf{g}} u(\mathbf{r}; \mathbf{k}) \quad (3.51)$$

For this reason, several ab initio all-electron programs for solid state simulations use plane waves to represent Bloch functions.<sup>147–152</sup> CRYSTAL code<sup>110</sup> was the first periodic ab initio all-electron program based on the use of atomic orbitals (Gaussian functions) to express the Bloch functions. In this way, the crystalline orbitals (COs)  $\Psi_i(\mathbf{r}; \mathbf{k})$  (the periodic version of molecular orbitals MOs) may be expressed as linear combinations of Bloch functions  $\Phi_\mu(\mathbf{r}; \mathbf{k})$ , which in turn are expanded as linear combinations of atomic orbitals  $\phi_\mu(r)$ . Then it is possible to write:

$$\Psi_i(\mathbf{r}; \mathbf{k}) = \sum_{\mu} a_{\mu,i}(k) \Phi_{\mu}(\mathbf{r}; \mathbf{k}) \quad \Phi_{\mu}(\mathbf{r}; \mathbf{k}) = \sum_{\mathbf{g}} \phi_{\mu}(\mathbf{r} - \mathbf{A}_{\mu} - \mathbf{g}) e^{i\mathbf{k} \cdot \mathbf{g}} \quad (3.52)$$

The exponential term  $e^{i\mathbf{k} \cdot \mathbf{g}}$  is the phase factor, dependent on the vector  $\mathbf{k}$  in the first Brillouin zone (FBZ) of the reciprocal lattice and on the translation vector  $\mathbf{g}$ .  $\mathbf{A}_{\mu}$  are the coordinates of the  $\mu$ -th atom on which the atomic orbitals are centered in the reference cell. The coefficients of the linear combinations which define the crystalline orbital are calculated for every  $\mathbf{k}$  vector of the reciprocal lattice according to

$$\mathbf{F}^k \mathbf{C}^k = \mathbf{S}^k \mathbf{C}^k \mathbf{E}^k \quad (3.53)$$

In which  $\mathbf{F}^k$ ,  $\mathbf{C}^k$ ,  $\mathbf{S}^k$  and  $\mathbf{E}^k$  are the Fock matrix, eigenvectors, overlap and eigenvalues matrices, respectively. Representing the Fock matrix in the basis of the reciprocal space makes the Fock matrix block-diagonal with each block referring to one particular point  $\mathbf{k}$  in the reciprocal space. Unfortunately, an infinite number of  $\mathbf{k}$  points exist such as an infinite number of factorized finite-sized blocks exists. In other words, Bloch functions as a basis set allow to transform a problem of infinite size into an infinite number of problems of finite size. Nevertheless, it is generally possible to sample the Fock matrix at a finite number of points and solve the approximate Schrödinger equation for a periodic system at different points in the first Brillouin zone. If sampling is convenient, the number of  $\mathbf{k}$  points to be considered is usually relatively small and solving the approximate Schrödinger equation in the reciprocal space is a feasible method.<sup>153</sup>

# Chapter 4

## Materials and Methods

The first part of this chapter gives a brief description of the zeolite materials, with a specific focus on CHA topology. Subsequently, a comprehensive description of the procedures adopted to synthesize and treat the copper-exchanged CHA samples employed in this work is provided. Finally, the details concerning the EPR measurements and the quantum chemical calculations are described.

### 4.1 Materials

#### 4.1.1 Copper-exchanged zeolites with Chabazite topology

##### General concepts

Zeolites are aluminosilicate microporous systems characterized by a regular three-dimensional framework of channels and cages.<sup>154</sup> The fundamental building unit of all zeolites is the  $[\text{SiO}_4]^{4-}$  tetrahedron. It forms a three-dimensional network through corner-sharing of the four O atoms and leads to a charge-neutral network.<sup>155</sup> Because of crystalline ordering, zeolites contain ordered cavities and pores that have characteristic shapes and sizes. More than 200 different structure types are known.<sup>156</sup> Some of these can be found in nature as minerals, but most are synthetic materials. Zeolites are represented with three-letter codes, which are under the supervision of the structure commission of the International Zeolite Association (IZA).<sup>156,157</sup>

The  $\text{Si}^{4+}$  sites are commonly substituted by  $\text{Al}^{3+}$ , thus giving an overall negative charge to the framework. This anionic charge inside the solid is charge-compensated by extra-framework cations. The amount of exchangeable cations is expressed by the cation exchange capacity which depends on the amount of Al doping. In principle, the degree of Al for Si substitution ranges from zero ( $\text{Si}/\text{Al} = \infty$ ) to  $\text{Si}/\text{Al} = 1$ . Whatever the  $\text{Si}/\text{Al}$  ratio, the isomorphous substitu-

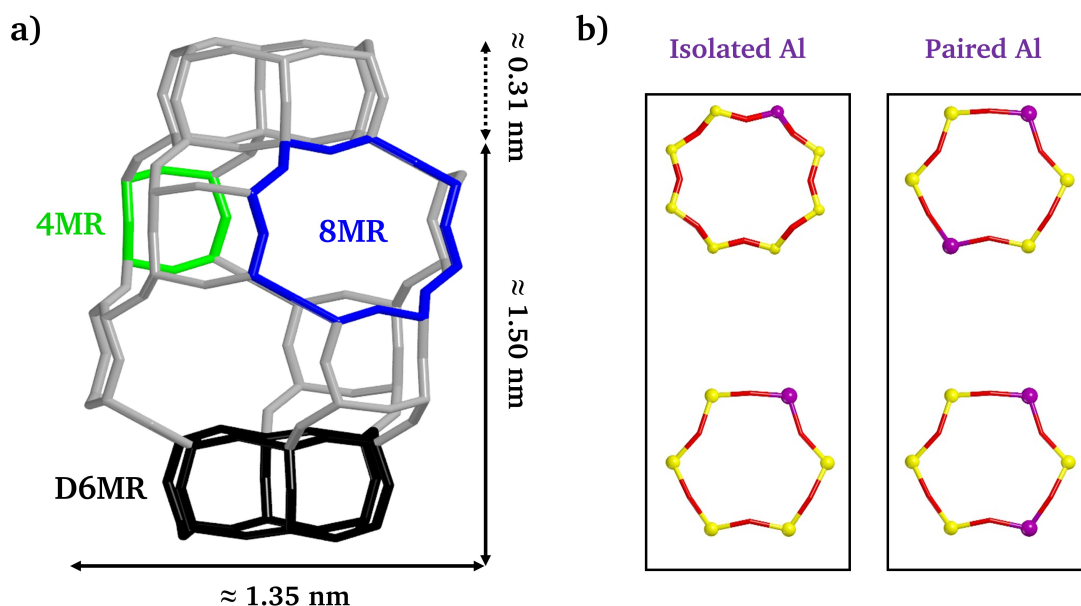


**Figure 4.1:** a) Schematic representation of CHA topology, underlining the presence of 4MRs, 6MRs and 8MRs and the major dimension of the cages. b) Possibilities of isolated and paired Al sites. Color code: Si atoms are drawn in yellow, O atoms in red and Al atoms in violet.

tion obeys Loewenstein's rule: two Al tetrahedra cannot be neighbours sharing an O atom.<sup>158</sup>

In natural zeolites, the extra-framework cations counterbalancing the negative charge of the framework are usually alkaline or alkaline earth metal ions. Since they are not covalently bound to it, they can be partially or totally exchanged by other cations, in particular TMI. Besides isolated cases where the TMI is inserted by employing chemical vapor deposition/impregnation<sup>32,159–162</sup> and or solid ion exchange,<sup>163,164</sup> in the vast majority of the literature the cation exchange is performed via aqueous phase ion-exchange using different TMIs salts. Such procedures are often carried out on  $H^+$ - or  $NH_4^+$ -zeolites, where the TMIs exchange for Brønsted acid sites (which in  $NH_4^+$ -zeolite are generated by thermal treatment with consequent  $NH_3$  release) or on  $Na^+$  (or other alkaline/alkaline earth metal ions) zeolites.

The framework of zeolites with CHA topology is characterized by layers of double six-membered rings (D6MRs) that are interconnected by units of four-membered rings (4MRs). The double six-membered ring layers are stacked in an ABC sequence, leading to a framework with a regular array of barrel-shaped cages interconnected by eight-membered rings (8MRs) windows (see Figure 4.1a).<sup>165–167</sup> The different possibilities of isolated and paired Al sites are illustrated in Figure 4.1b

### Synthesis of copper-exchanged Chabazite samples

In this contribution, four copper-exchanged CHA samples were synthesized. Some of the synthetic procedures were performed in Erlangen at the Erlangen Center for Interface Research and Catalysis under the supervision of Prof. Dr. Martin Hartmann and his group. For the sake of clarity, the copper-containing CHA samples are henceforth labelled as Cu-CHA(A), Cu-CHA(B), Cu-CHA(C) and Cu-CHA(D). In the following, the detailed recipes for the synthesis are provided.

- **Cu-CHA(A).** Na-CHA was synthesized using the procedure reported by Fickel and Lobo.<sup>21</sup> 12 g of H<sub>2</sub>O, 0.16 g of NaOH (Fisher Scientific) and 5 g of sodium silicate (Sigma Aldrich, 26.5 wt% SiO<sub>2</sub>, 10.6 wt% Na<sub>2</sub>O) were mixed and stirred for 15 minutes; then 0.5 g of NH<sub>4</sub>-Y (Zeolyst CBV100, Si/Al = 2.47) were added to the solution and stirred for 30 minutes. After that, 0.8 g of N,N,N-trimethyl-1-adamantammonium hydroxide (TMAdaOH) (25 wt%) were added to the solution and stirred for other 30 minutes. The resulting solution was transferred into Teflon-lined steel autoclave and heated at 413 K for 6 days. The product was recovered by centrifugation, washed more times with deionized water, dried overnight at 348 K and calcined in air at 823 K for 8 hours to remove the TMAdaOH. The resulting zeolite was a pure Na-CHA (Si/Al=7). The introduction of Cu<sup>II</sup> ions was performed by following the procedure reported by Kevan et al.<sup>33</sup> The protonated form of the CHA was prepared after ion exchange with a 10 % solution of ammonia nitrate, air-drying and calcined at 773 K in air to drive-off the ammonia. Thus, 0.5 g of the zeolite were stirred with a solution composed of 5 mL of 2 mM Cu(NO<sub>3</sub>)<sub>2</sub> and 50 mL of deionized water at about 343 K for 1 hour. The sample was recovered by centrifugation and washed with boiling water to remove Cu<sup>II</sup> ions from the exterior surface. The elemental percentage composition of the final sample, determined by ICP-AES analysis, is the following: 33.35 wt% of Si, 4.76 wt% of Al and 0.01 wt% for Cu. Hence, the Cu/Al ratio is 0.001.
- **Cu-CHA(B).** Na-CHA was prepared following the procedure published in the patent literature.<sup>168</sup> The resulting synthesis gel was transferred to a Teflon-lined steel autoclave and heated to 413 K for 6 days. The product was recovered by centrifugation, washed several times with deionized water, dried overnight at 348 K and calcined in air at 823 K for 8 h to remove the TMAdaOH. The resulting zeolite was a pure Na-CHA (Si/Al = 15) without FAU impurities. Prior to the copper exchange, the protonated form of the zeolite was obtained by liquid ion exchange with a 10% solution of ammonia nitrate, drying in the oven (348 K) overnight and heating

at 823 K for 3 h to remove the ammonia residues from the framework. Cu ion-exchange was performed by following the same recipe described for Cu-CHA(A). The elemental percentage composition of the sample, determined by ICP-AES analysis, is the following: 43.70 wt% of Si, 2.72 wt% of Al and 0.03 wt% for Cu. The Cu/Al ratio is thus 0.005.

- **Cu-CHA(C).** K/Na-CHA was synthesized through interzeolite conversion method employing NH<sub>4</sub>-Y (Zeolyst CBV720, Si/Al = 14) as Si and Al source, TMAdaOH (25 wt%) as organic structure directing agent and KOH and NaOH as mineralizing agents. The mixture was constructed by stirring NaOH, KOH and the TMAdaOH followed by the addition of zeolite Y. The following gel composition was adopted: SiO<sub>2</sub> : 1 Al<sub>2</sub>O<sub>3</sub> : 0.067 TMAdaOH : 0.220 Na<sub>2</sub>O : 0.037 K<sub>2</sub>O : 0.012. The mixture was dried at 348 K overnight in convection oven and afterwards put in a steam sterilizer where the crystallization occurred via steam assisted crystallization procedure (T=413 K for 24 hours). The product was retrieved by centrifugation, washed four times with deionized water, dried overnight and then calcined in air at 823 K for 8 hours. The resulting zeolite was in K/Na-CHA (Si/Al=12). The ion-exchange with Cu<sup>II</sup> was carried out by slightly modifying the procedure described for Cu-CHA(A). After obtaining the H-form of the zeolite (as described for Cu-CHA(A)), 1 g of the zeolite were stirred with a solution composed of 10 mL of 5mM Cu(NO<sub>3</sub>)<sub>2</sub> and 100 mL of deionized water at about 343 K for 2 hours. The sample was retrieved by centrifugation and washed with boiling water to remove Cu<sup>II</sup> ions from the exterior surface. The elemental percentage composition of the final sample, determined by ICP-AES analysis, is the following: 37.89 wt% of Si, 2.82 wt% of Al and 0.62 wt% for Cu. Hence, the Cu/Al ratio is 0.09.
- **Cu-CHA(D).** The H-form of this zeolite comes from the same batch synthesized for Cu-CHA(C). The difference between the two samples is due to the different procedure and amount of Cu<sup>II</sup> ions exchanged. For Cu-CHA(D), a modified version of the procedure reported by Giordanino et al.<sup>169</sup> was followed to introduce the Cu<sup>II</sup> ions into the CHA framework. 125 mL of a solution 6mM of Cu(CH<sub>3</sub>COO)<sub>2</sub> were mixed with 0.5 g of zeolite for 24 hours at 343 K. The exchanged zeolite was recovered by centrifugation, dried overnight at 343 K and calcined at 773 K in static air for 3 h in order to remove the residual ligands. The elemental percentage composition of the final sample, determined by ICP-AES analysis, is the following: 34.55 wt% of Si, 2.69 wt% of Al and 4.23 wt% for Cu. Hence, the Cu/Al ratio is 0.67.

## 4.2 Methods

### 4.2.1 Activation of copper-exchanged Chabazite samples

The activation of zeolites is a key step for catalysis purposes because the evacuation of water and other molecules adsorbed in the channels and cavities is necessary to make the active sites accessible to reactants. Therefore the speciation of the active species is strongly affected by the activation process.<sup>24–26,170</sup>

In this work the activation of copper-exchanged CHA samples was performed either in inert atmosphere or O<sub>2</sub> atmosphere. In the first case, about 25 mg of Cu-CHA were dehydrated at several temperatures under dynamic vacuum (final pressure  $<10^{-4}$  mbar) for a maximum time of 2 hours. In the latter case, the same amount of zeolite was initially dehydrated at room temperature until reaching an equilibrium pressure  $<10^{-4}$  mbar. After that, the EPR cell was filled with O<sub>2</sub> (about 200 mbar at equilibrium pressure) in order to create an oxidative atmosphere during the dehydration step. The sample was then heated at 523 K for 2 hours (heating ramp 5 K/min). After the treatment the cell was evacuated under dynamic vacuum ( $<10^{-4}$  mbar) at the same temperature (523 K) for 1 hour.

### 4.2.2 <sup>17</sup>O isotopic labelling of zeolite framework

Cu-CHA(B) was isotopically enriched by exposing its dehydrated powder to three consecutive hydration and dehydration cycles in presence of vapours of H<sub>2</sub><sup>17</sup>O (86% isotopic enrichment supplied by Icon Services New Jersey) at 393 K for 2 hours: this method was proved to be extremely efficient in the <sup>17</sup>O enrichment of zeolites without causing any dealumination of the framework.<sup>171</sup> At the end of the process, a <sup>17</sup>O enriched Cu-CHA(B) sample hydrated with H<sub>2</sub><sup>17</sup>O was obtained and, after a final dehydration step, the isotopically labelled water was removed from the framework. Finally, the dehydrated <sup>17</sup>O labelled sample was rehydrated with H<sub>2</sub><sup>17</sup>O by merely exposing the solid to air for 24 hours in order to further prove the framework substitution of <sup>16</sup>O with <sup>17</sup>O.

## 4.3 EPR measurements

The X-band (microwave frequency of 9.42 GHz) CW-EPR spectra were detected at 298 K and 77 K on a Bruker EMX spectrometer equipped with an ER 4119 HS cylindrical cavity and a Bruker EMXmicro spectrometer. In both cases, modulation frequency of 100 kHz, a modulation amplitude of 1 mT, and a microwave power of 2 mW were adopted. Pulse EPR measurements were performed at 10

and 15 K at X-band (microwave frequency 9.75 GHz) and Q-band (microwave frequency 33.50 GHz) on a Bruker ELEXYS 580 spectrometer equipped with helium gas-flow cryostat from Oxford Inc. The SpinCount package of Bruker Xenon Software<sup>172</sup> was employed to quantify the spin number (total amount of paramagnetic Cu<sup>II</sup> ions) in each sample. X-band and Q-band ESE detected EPR spectra were acquired with the pulse sequence  $\pi/2 - \tau - \pi - \tau - echo$ . The pulse lengths of  $t_{\pi/2} = 16$  ns,  $t_{\pi} = 32$  ns and a  $\tau$  value of 200 ns were used in conjunction of a shot repetition time of 3.55 KHz.

X-band HYSCORE<sup>98</sup> measurements were carried out with the standard pulse sequence  $\pi/2 - \tau - \pi/2 - t_1 - \pi - t_2 - \pi/2 - \tau - echo$ , employing a eight-step phase cycle for deleting unwanted echoes. Pulse lengths  $t_{\pi/2} = 16$  ns,  $t_{\pi} = 32$  ns and a shot repetition time of 1.77 KHz were used. The increment of the time intervals  $t_1$  and  $t_2$  was 16 ns, starting from 80 to 2704 ns giving a data matrix of 170x170. The  $\tau$  value used for each measurements are reported in figure captions. The time traces of HYSCORE spectra were baseline corrected with a third-order polynomial, apodized with a hamming window and zero-filled to 2048 points. After 2D Fourier transformation, the absolute-value spectra were calculated.

Q-band ENDOR measurements were carried out at 15 K and 20 K by employing the Davies pulse sequence ( $\pi_{MW} - \pi_{RF} - \pi/2_{MW} - \tau - \pi_{MW} - \tau - echo$ ).<sup>101</sup> Unselective microwave pulses were employed to suppresses the small hyperfine couplings in favour of large ones. The RF pulse length was set to 14  $\mu$ s,  $\tau$  was set equal to 180 ns and a resolution of 440 points was adopted. Further experimental settings are provided in the figure captions. All the EPR spectra were simulated by using the Easyspin package (version 6.0.0 dev 26 and 36)<sup>87</sup>

## 4.4 Computational details

### 4.4.1 Periodic and cluster modelling

CHA structure was modelled by employing periodic boundary conditions which better describe the crystalline environment of the zeolite with respect to cluster approaches. Firstly, a purely siliceous CHA (space group  $R\bar{3}m$ ) composed by a rhombohedral lattice with 12 tetrahedral (T) sites per unit cell was considered. Therefore, two Si atoms were replaced by two Al atoms generating a model with a Si/Al ratio equal to 5. The excess of negative charge is exactly compensated by one Cu<sup>II</sup> cations per unit cell. Structures with different distributions and amount (Si/Al ratio of 5 and 11) of aluminium atoms were fully optimized in P1 space group without any symmetry constrains in order to find the most stable Al configuration. Hydrated copper species incorporated inside the CHA



framework were simulated by adding water molecules to the previously optimized structures or by inserting a Cu molecular complex inside the CHA cavity and reoptimizing the whole adduct. In other models, only one Si atom was substituted by one Al atom and the negative charge was compensated by one  $\text{Cu}^{\text{II}}$  cation and a  $\text{OH}^-$  group per unit cell. Supercell models (2x2x1) were also employed to account for the dilution of the Cu centers in the considered samples. For these cases, a Cu/Al ratio of 0.5 was achieved by inserting 2 Al sites and 1  $[\text{Cu}^{\text{II}}\text{OH}]^+$  species per unit cell. In this way, 1 Al site was charge compensated by an acidic proton (Brønsted site) whereas the second one was compensated by the copper hydroxyl species.

#### 4.4.2 Periodic calculations

Periodic calculations (geometry optimization, calculations of hyperfine couplings and vibrational frequencies) were performed by using the replicated data parallel version of CRYSTAL17 code (PCRYSTAL)<sup>110</sup> within the framework of DFT exploiting the hybrid B3LYP method, Becke's three parameters exchange functional and the correlation functional from Lee, Yang and Parr.<sup>131,132</sup> Dispersive interactions, extremely relevant in determining the geometry of zeolites,<sup>173,174</sup> were taken into account empirically through the so-called DFT-D3 method in conjunction with a three-body correction.<sup>175,176</sup> Pob-TZVP basis set<sup>177</sup> was adopted for all the elements, except for the extra-lattice O and H atoms of the hydroxyl group and water molecules for which the Ahlrichs VTZP basis set<sup>178</sup> was employed. For the prediction of  $^{27}\text{Al}$ ,  $^1\text{H}$  and  $^{17}\text{O}$  hfi, single point calculations performed on the optimized structures were carried out by employing the aug-cc-pVTZ-J basis set<sup>179</sup> for Al atoms, and the EPR-III<sup>180</sup> for H and O atoms at B3LYP-D3. Primitive Gaussian functions with exponents lower than 0.06 were removed in order to avoid linear dependency in the Self-Consistent Cycle (SCF). The other elements were treated with the same basis sets used for geometry optimizations. A pruned grid consisting of 75 radial points and a maximum number of 974 angular points in regions relevant for chemical bonding has been adopted. The accuracy of the calculation of the two electron integrals in the Coulomb and exchange series was controlled by setting truncation criteria at the values of  $10^{-7}$  except for the pseudo-overlap of the HF exchange series which was fixed to  $10^{-25}$ . A shrink factor equals to 6 was used to diagonalize the Hamiltonian matrix in at least 112 k-points of the first Brillouin zone. The default value of mixing (30%) of the Kohn-Sham (KS) matrix at a cycle with the previous one was adopted. The threshold in energy variation of SCF cycles was set equal to  $10^{-8}$  Hartree for geometry optimization and equal to  $10^{-10}$  Hartree for frequency calculations. The number of unpaired electrons in the unit cell

was not locked to one in order to leave the SCF procedure to freely converge to a doublet spin state of the system wavefunction.

Harmonic vibrational frequencies were computed at the center of the first Brillouin zone in the reciprocal space ( $\Gamma$  point) from the diagonalization of the mass-weighted Hessian matrix of the second energy derivatives with respect to atomic displacement.<sup>181–183</sup> Two displacements for each atom along each cartesian direction were considered to numerically compute the second energy derivatives.

Anharmonic calculation of O-H bond stretching was performed by considering the selected O-H bond as an independent oscillator.<sup>184,185</sup> The O-H distance was varied around the equilibrium value  $d_0$  [ $d_0 + (-0.2, -0.16, -0.06, 0.00, 0.16, 0.24, 0.3 \text{ \AA})$ ]. All the other geometrical features were kept fixed. For each value of the O-H distance the total potential energy was computed and a polynomial curve of sixth degree was used to best fit the energy points (root mean square error below  $10^6$  Hartree). Thus, the corresponding mono-dimensional nuclear Schrödinger equation is solved numerically<sup>186</sup> according to the procedure proposed by P. Ugliengo.

Molecular cluster calculations were carried out to compute  $g$ -tensor, hyperfine interactions of  $\text{Cu}^{\text{II}}$  species and  $^1\text{H}$  nucleus as well as the orientation of the  $^1\text{H}$  hyperfine tensor with respect to the  $g$  frame. Cluster models were cut out from the related optimized periodic structure and the dangling bonds were saturated with hydrogen atoms oriented along the broken bonds. No further geometry optimization was performed in order to maintain the same relaxed atomic coordinates as in the optimized periodic structure. The net charge on the molecular models was set to 0 in a doublet spin state.

#### 4.4.3 Cluster calculations

Cluster calculations were carried out with ORCA (v4.2.1 and v5.0.2)<sup>187,188</sup> code. The SOC contribution (not negligible for  $\text{Cu}^{\text{II}}$  species)<sup>189</sup> was explicitly treated by using SOMF operator.<sup>117</sup> The potential was constructed to include one-electron terms, compute the Coulomb term in a semi-numeric way, incorporate exchange via one-center exact integrals including the spin-other orbit interaction and include local DFT correlation (SOCFlags 1,2,3,1 in ORCA). The CP(PPP) basis set<sup>190</sup> was employed for Cu nucleus for all the calculations, while the def2-TZVP basis sets<sup>191</sup> were employed for Si, Al, O and H atoms for DFT computations. Concerning DFT calculations (hybrid and double hybrid), the H atom from the  $\text{OH}^-$  group was treated with the well-known EPR-III basis set. Increased integration grids were employed (DefGrid3 in ORCA v5.0.2 and Grid7 in ORCA v4.2.1 nomenclature) and tight energy convergence settings were applied throughout

(TightSCF). The resolution of identity (RI) in conjunction with the corresponding auxiliary basis sets were adopted. In case no auxiliary basis set was available, the AutoAux keyword was employed to automatically build the auxiliary basis set. Double-hybrid calculations were carried out by using the “relaxed” Møller-Plesset (MP2) density and keeping all the electron active (NoFrozenCore keyword).

Open-shell domain-based local pair natural orbital coupled cluster with single and double excitations (DLPNO-CCSD) calculations<sup>192</sup> were performed to compute the  $^1\text{H}$  hfi of the hydroxo group bound to  $\text{Cu}^{\text{II}}$ . The CCSD calculations were initiated with unrestricted Kohn-Sham orbitals and followed the standard DLPNO procedure.<sup>193,194</sup> The specific settings employed for this method are the followings:  $\text{TCutMKN} = 1.0 \times 10^{-4}$ ,  $\text{TCutDO} = 5.0 \times 10^{-3}$ ,  $\text{TCutPNO} = 1.0 \times 10^{-7}$ ,  $\text{TCutPNOSingles} = 0.00$ ,  $\text{TScalePNOCore} = 1.0 \times 10^{-3}$ , and  $\text{TScalePNOSOMO} = 1.0 \times 10^{-1}$ . All the electrons were set as active and “unrelaxed” spin density was adopted (where the effect of orbital relaxation is recovered only through the action of  $\exp(T_1)$  onto the reference).<sup>192</sup> Concerning CCSD calculations, all the elements (apart from Cu) were treated with cc-pwCVQZ basis sets<sup>195,196</sup> and its corresponding auxiliary basis sets. The maximum amount of memory per core used for these calculations was 62.5 GB.

# Chapter 5

## Results and Discussion

Copper-exchanged CHA zeolites feature a plurality of different copper species ranging from monomeric<sup>197</sup> to dinuclear<sup>198,199</sup> ( $[\text{Cu}_2\text{O}]^{2+}$  and  $[\text{Cu}_2\text{O}_2]^{2+}$ ) copper sites and polynuclear clusters<sup>200</sup> whose nature and abundance are intimately linked to the zeolite composition and its chemical treatment. These different copper species exhibit unique spectroscopic features, which reflect specific electronic and geometric structures that can make key contributions to the reactivity. Indeed, the characterization of the geometric as well as the electronic nature of the copper active sites represents the basis for understanding the catalytic mechanisms.<sup>13,14</sup>

In this thesis a multitechnique approach involving advanced EPR methodologies in conjunction with state-of-the-art quantum chemical modelling is adopted to shed light on the microscopic structure of monomeric  $\text{Cu}^{\text{II}}$  moieties in CHA systems as a function of the hydration conditions and sample composition. Specific synthetic protocols, activation procedures and isotopic enrichment are employed to tackle the complexity of the problem.

The first section of the current chapter concerns the employment of pulse EPR spectroscopy (ENDOR and HYSCORE) combined with  $^{17}\text{O}$  isotopic enrichment and quantum chemical modelling. The combined methodology provides unprecedented details on the microscopic structure of the  $\text{Cu}^{\text{II}}$  sites and follow the evolution of the  $\text{Cu}^{\text{II}}$  species as a function of the hydration of the material.<sup>78</sup> The second section regards the determination of the atomistic structure of hydroxo  $\text{Cu}^{\text{II}}$  species by using high resolution hyperfine techniques (HYSCORE) and accurate quantum chemical methods.<sup>79</sup> As it will be pointed out, this structure differs from previous assignments present in literature. The detection and assignment of the EPR fingerprint of the copper-hydroxo species allows to quantify their amount as a function of the zeolite composition.

## 5.1 $^{17}\text{O}$ EPR characterization of $\text{Cu}^{\text{II}}$ single-metal sites in Chabazite

EPR techniques have been abundantly used to obtain information on the structure and topological distribution of isolated  $\text{Cu}^{\text{II}}$  species in zeolites.<sup>29,30,33–41</sup> However, the most revealing and important piece of information that can be extracted from this technique, the detection of hyperfine couplings for the coordinating oxygen atoms,<sup>171,201,202</sup> is currently missing.

The only magnetic isotope of oxygen is  $^{17}\text{O}$  ( $I = 5/2$ ) but its natural abundance (0.037%) is by far lower than the value necessary to detect a hyperfine structure. The exploitation of hyperfine techniques for the investigation of the metal-oxygen bond requires therefore the isotopic enrichment of oxide solid systems that involves both cost and effort, which however can be very rewarding. Indeed  $^{17}\text{O}$  solid state NMR has revealed invaluable to address important issues in this context, providing unique insights into crucial aspects related to the local structure of aluminosilicate zeolites.<sup>201,202</sup> However, this approach cannot be applied to investigate the Cu–O interaction due to the paramagnetic nature of  $\text{Cu}^{\text{II}}$  ions and low number of  $^{17}\text{O}$  nuclei affected by  $\text{Cu}^{\text{II}}$ .  $^{17}\text{O}$  EPR has been used in different context to derive structural information on paramagnetic species.<sup>203–208</sup>

In this section, the  $^{17}\text{O}$  nuclear transition frequencies detected by ENDOR techniques from oxygen donor atoms directly bound to  $\text{Cu}^{\text{II}}$  species in a low copper-loaded CHA (Cu-CHA(B)) is reported.<sup>78</sup> This enables to obtain exquisite details on the nature of the Cu interaction with the oxygen donor atoms of the zeolite framework and of solvating water molecules. The measured  $^{17}\text{O}$  hyperfine couplings provide an effective handle to obtain a detailed understanding of the Cu–O bond, to assess the siting of Al in the most stable Cu coordination and to follow the migration of  $\text{Cu}^{\text{II}}$  species across the zeolite channels as a function of hydrating conditions.

### 5.1.1 Structure and dynamics of isolated $\text{Cu}^{\text{II}}$ ions from CW-EPR

Water has been shown to play a strong effect on the reactivity of Cu species in zeolites promoting specific reaction pathways,<sup>26,209,210</sup> promoting dynamic catalytic mechanisms at the cross road between homogeneous and heterogeneous catalysis.<sup>5,211,212</sup> For this reason, the first key question to address is related to the structure and evolution of  $\text{Cu}^{\text{II}}$  species as a function of hydration and their interaction with the zeolite framework. According to early reports<sup>21–23</sup> and more recent studies,<sup>24,26,69</sup> the potential extra-framework sites of Cu cations are located on the window of D6MRs (Figure 5.1a) or on 8MRs (Figure 5.1b) with

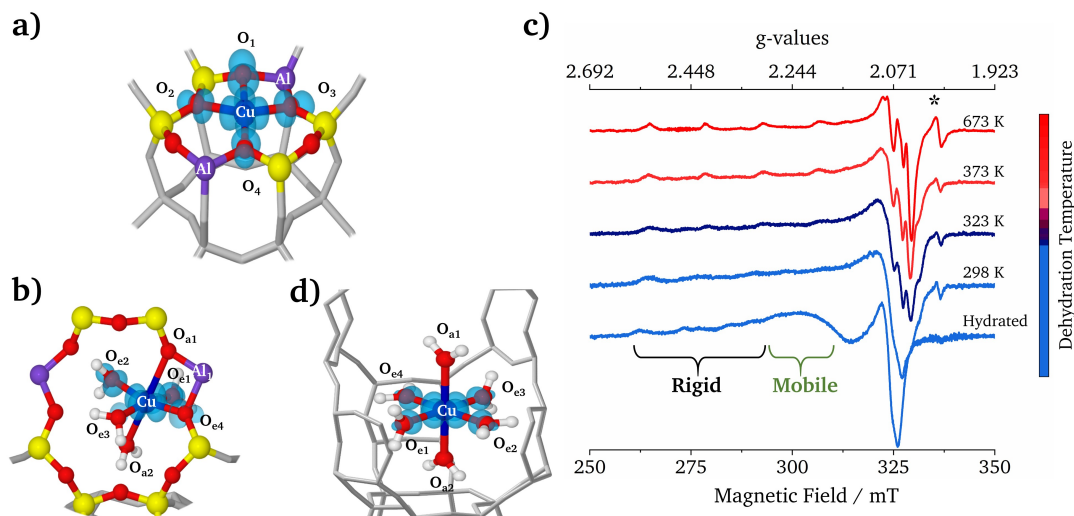


**Figure 5.1:** Spin density plots of dehydrated Cu<sup>II</sup> ion sitting on 6MR and hydrated Cu<sup>II</sup> complex attached to the framework in 8MR site are illustrated in a) and b), respectively. c) X-band CW-EPR spectra recorded at room temperature of fully hydrated with H<sub>2</sub><sup>16</sup>O Cu-CHA(B) and dehydrated at increasing temperatures according to the procedure described in paragraph 4.2.1. The hyperfine components of rigid and mobile species are indicated. The asterisk indicates a carbon radical signal. d) Spin density plots of [Cu(H<sub>2</sub>O)<sub>6</sub>]<sup>2+</sup> complex encapsulated in the largest CHA's cage. The labels O<sub>en</sub> and O<sub>an</sub> refer to *n* equatorial and axial oxygen ligands, respectively. This figure was adapted from Bruzzese *et al.*<sup>78</sup>

either two framework aluminium atoms (2Al) or one aluminium site (1Al) plus an extra-lattice OH<sup>-</sup> ligand for charge compensation (for additional details on this structure, see Section 5.2).

CW-EPR spectra of Cu-CHA(B) recorded as a function of the dehydration temperature are reported in Figure 5.1c and show characteristic spectral patterns depending on the degree of hydration. The spectrum of the fully hydrated system is due to two  $S = 1/2$  EPR signals, characteristic of Cu<sup>II</sup> ion with a different local environment. The room temperature (RT) spectrum shows the contribution of a motionally averaged and a rigid-limit anisotropic components, corresponding to a mobile solvated structure (Figure 5.1d) and framework-bound Cu<sup>II</sup> species (Figure 5.1b), respectively. Indeed, this spectrum can be simulated by including a motionally averaged component obtained by imposing a rotational correlation time  $\tau = 10$ -11 ns to the spin Hamiltonian parameters determined from the rigid-limit spectrum (see Figure 5.2a, at the bottom). At low temperature, the motion of the solvated species is frozen and the spectrum

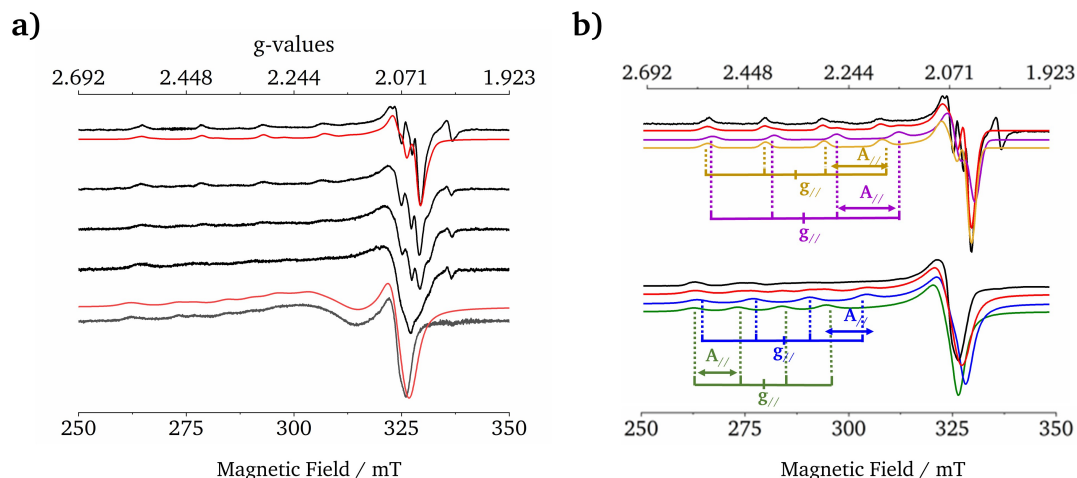


**Figure 5.2:** a) Experimental (black) X-band CW-EPR spectra recorded at room temperature at different dehydration stages. The simulations of the spectra of the fully hydrated and dehydrated samples are shown in red. The spectra of the dehydrated sample at room temperature and 77 K are virtually identical. b) Experimental (black) and simulated (red) X-band CW-EPR spectra recorded at 77 K of fully hydrated and dehydrated Cu-CHA. The contribution of each individual species (A - D in Table 5.1) is shown in blue, green, gold and violet for A, B, C and D, respectively. This figure was first published in Bruzzese *et al.*<sup>78</sup>

exhibits only anisotropic features (see Figure 5.2b, at the bottom).

The progressive dehydration of the sample (Figure 5.1c) is accompanied by a narrowing of the spectral linewidth and disappearance of the motionally averaged component in the RT CW-EPR spectrum. A sharp signal at  $g = 2.0028$  (asterisk in Figure 5.1c) is observed in the dehydrated sample, which is often present even in the most careful calcination protocols and assigned to carbon radicals deriving from carbonaceous residues in the zeolite framework.<sup>42</sup> After dehydration at 673 K the overall EPR spectral intensity is reduced of about 40% with respect to the fully hydrated system. The loss of EPR intensity during the sample activation is a well-known phenomenon, which strongly depends on the Si/Al and Cu/Al ratios.<sup>43,213</sup> A detailed analysis on the possible mechanisms leading to such a signal loss is reported in the following Section (see paragraph 5.2.3).

To summarize, the analysis of the CW-EPR spectra as a function of the sample dehydration evidences the presence of at least two  $\text{Cu}^{\text{II}}$  species characterized by distinctively different spin Hamiltonian parameters, which change as a function

**Table 5.1:** Experimental Cu  $g$ - and  $A$ -tensors obtained from the simulations of the CW-EPR spectra recorded at 77 K and reported in Figure 5.2b. Only the absolute values of the hyperfine components are extracted from the spectra. Hyperfine couplings are given in units of MHz.

Samples	Weight	$g_{\perp}$	$g_{\parallel}$	$A_{\perp}$	$A_{\parallel}$
Hydrated	55% A	$2.070 \pm 0.005$	$2.415 \pm 0.001$	$30 \pm 10$	$400 \pm 5$
	45% B	$2.065 \pm 0.006$	$2.370 \pm 0.002$	$30 \pm 10$	$450 \pm 4$
Dehydrated	85% C	$2.058 \pm 0.002$	$2.355 \pm 0.001$	$30 \pm 10$	$462 \pm 5$
	15% D	$2.062 \pm 0.003$	$2.320 \pm 0.001$	$30 \pm 10$	$487 \pm 4$

of the dehydration treatment in line with previous reports.<sup>108</sup> In the case of the hydrated sample, two species with nearly equal abundance are present (Table 5.1). One such species (A in Table 5.1) shows spin Hamiltonian parameters typical for  $[\text{Cu}(\text{H}_2\text{O})_6]^{2+}$  complexes (Figure 5.1d). The other species (B in Table 5.1) has spin Hamiltonian parameters consistent with a tetragonally elongated 6-coordination, i.e. with a distorted octahedral geometry (Figure 5.1b).<sup>29,214</sup> On the other hand, the spectrum of the fully dehydrated sample is dominated by a  $\text{Cu}^{\text{II}}$  species accounting for about 80% of the total EPR intensity with spin Hamiltonian parameters (C in Table 5.1) agreeing with a tetragonal planar coordination of  $\text{Cu}^{\text{II}}$  (Figure 5.1a).<sup>33,51,215,216</sup> These configurations are supported DFT calculations (for further details on the computed EPR parameters, see Appendix A) that give the SOMO as dominated by the Cu  $3d_{x^2-y^2}$  orbital with participation of the  $2p$  oxygen orbitals (Figure 5.1a-b-d). The degree of covalency of the Cu–O bond (i.e. the oxygen contribution to the SOMO) will be addressed in the following, along with the detailed topological description of the  $\text{Cu}^{\text{II}}$  docking sites under specific hydration conditions.

### 5.1.2 Geometric and electronic structure through $^{27}\text{Al}$ and $^1\text{H}$ spin density studies

Most of the information relative to the topological distribution of the  $\text{Cu}^{\text{II}}$  species is hidden in the inhomogeneously broadened line of the CW-EPR spectrum and is related to the hyperfine interactions with nearby magnetic nuclei ( $^1\text{H}$ ,  $^{27}\text{Al}$  and  $^{17}\text{O}$ ). In order to obtain such fundamental knowledge for the structural characterization of  $\text{Cu}^{\text{II}}$  siting, hyperfine techniques (HYSCORE and ENDOR) were employed at X- and Q-band frequencies. The progressive dehydration of the sample was carefully followed by X-band HYSCORE and Q-band Davies ENDOR experiments. The results are shown in Figure 5.3 where  $^1\text{H}$  HYSCORE,  $^1\text{H}$  ENDOR and  $^{27}\text{Al}$  HYSCORE experiments are shown for the same dehydration



conditions reported in Figure 5.1c.

The  $^1\text{H}$  HYSCORE spectrum of the hydrated sample is characterized by two distinct ridges with maximum extension of the order of 9 and 3 MHz (Figure 5.3a, at the top). These couplings are also confirmed by Q-band Davies ENDOR experiments (Figure 5.3b, at the top). The field dependent experimental spectra are simulated exceedingly well considering two interacting protons with hyperfine coupling tensors (in MHz) of  $\mathbf{A}_{\text{H}(1)} = [-5.5 \quad -7.5 \quad +8.5]$  and  $\mathbf{A}_{\text{H}(2)} = [-2.7 \quad -3.7 \quad +7.3]$ , whereby the maximum coupling of H(1) lies in the plane of the  $3d_{x^2-y^2}$  orbital, while for H(2) is approximately perpendicular to it. The smaller hyperfine coupling also correlates with the larger axial Cu–O distance (around 0.30 nm with respect 0.25 nm of the equatorial Cu–O distance; distances obtained from periodic DFT geometry optimization are listed in Table A.3) of the axially coordinating water molecules. These values are typical for hexaaquacopper complexes (Figure 5.1d) and were attributed by Pöppl and Kevan to equatorial and axial water molecules of the  $[\text{Cu}(\text{H}_2\text{O})_6]^{2+}$  complex.<sup>31</sup> A very weakly coupled proton signal is also detected and labelled H(3) in Figure 5.3, which we assign to second shell coordinating water molecules. The intensity of the  $^1\text{H}$  HYSCORE ridges decreases until the signal completely disappears in the fully dehydrated state, probing the progressive dehydration of the sample. Correspondingly, the  $^1\text{H}$  ENDOR spectra show that the weakly coupled protons (H(2) and H(3)) are the first one to be lost at this dehydration stage. These couplings are amenable to axially coordinated water molecules (H(2)) or second shell coordinating  $\text{H}_2\text{O}$  (H(3)), both displaying a weaker binding energy and therefore removed in the first stages of the dehydration process. On the other hand, H(4) nuclei possess hyperfine couplings and Euler angles similar to H(1), suggesting the stronger persistence of equatorial protons with respect to axial ones. When complete dehydration was achieved, the proton signals are no longer observed (Figure 5.3a, b, at the bottom) proving that all coordinated water molecules were removed.

$^{27}\text{Al}$  HYSCORE spectra (Figure 5.3c) display a pair of cross peaks centered at the Al Larmor frequency ( $\nu_{\text{Al}}$ ) indicating a hyperfine interaction of the order of 3 MHz. The narrow shape of the cross peaks and absence of multiple quantum transitions indicate a low value of the nuclear quadrupole interaction (estimated to be of the order of  $e^2qQ/h \leq 4$  MHz, see Figure A.1). These features are typical for  $S = 1/2$  transition metal ions in zeolite systems<sup>44,45,217</sup> and diagnostic of M–O–Al linkages, demonstrating that under hydration conditions a fraction of the  $\text{Cu}^{\text{II}}$  ions maintains, at least, a partial interaction with the zeolite framework, in agreement with the RT CW-EPR spectrum. At increasing dehydration temperatures, the  $^{27}\text{Al}$  signals drastically change, evolving from well-defined cross peaks in the hydrated sample to a unique unresolved diffuse signal in the

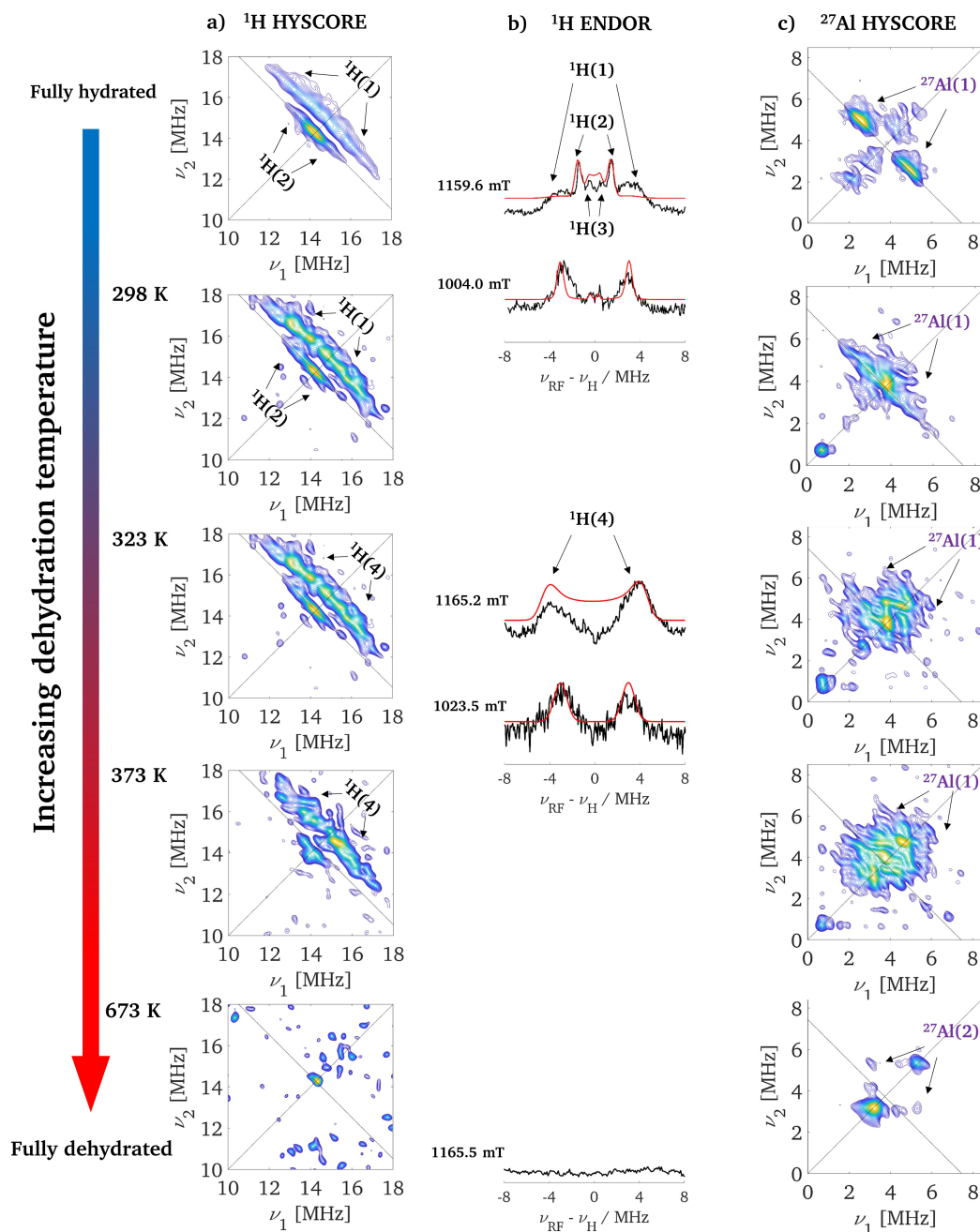


**Figure 5.3:** a) X-band  $^1\text{H}$  HYSORE spectra recorded at 4.5 K and obtained at the echo maximum intensity position of Cu-CHA(B) gradually dehydrated. b) Corresponding Q-band  $^1\text{H}$  Davies ENDOR spectra (black line) acquired at 20 K at the field indicated above the plot and their simulations (red line). c) X-band  $^{27}\text{Al}$  HYSORE spectra recorded at same experimental conditions of  $^1\text{H}$  HYSORE spectra.  $^1\text{H}$  and  $^{27}\text{Al}$  signals are indicated by arrows. The parameters used in the simulation satisfy both HYSORE and Davies ENDOR spectra. This figure was first published in Bruzzese *et al.*<sup>78</sup>

**Table 5.2:** Experimental  $^1\text{H}$  and  $^{27}\text{Al}$  hyperfine coupling components and quadrupolar coupling constants used for the simulations of HYSCORE and ENDOR spectra in Figure 5.3. All hyperfine interactions are given in units of MHz, while angles are in degrees.

Nucleus			$a_{\text{iso}}$	$T_1$	$T_2$	$T_3$	$[\alpha, \beta, \gamma]$	$e^2qQ/h$	$[\alpha', \beta', \gamma']$
$^1\text{H}$	Hydrated	H(1)	$-1.5 \pm 0.2$	$-4.0 \pm 0.3$	$-6.0 \pm 0.2$	$10 \pm 0.8$	$[0, 90, 0] \pm 10$		
		H(2)	$0.3 \pm 0.2$	$-3.0 \pm 0.2$	$-4.0 \pm 0.3$	$7.0 \pm 0.5$	$[0, 20, 0] \pm 5$		
		H(3)	$-0.8 \pm 0.2$	$-0.4 \pm 0.3$	$-0.4 \pm 0.3$	$-0.8 \pm 0.3$	$[0, 50, 0] \pm 20$		
	Part. Hydrated	H(4)	$-2.2 \pm 0.2$	$-4.0 \pm 0.3$	$-7.0 \pm 0.2$	$11 \pm 0.8$	$[0, 85, 0] \pm 5$		
$^{27}\text{Al}$	Hydrated	Al(1)	$-2.3 \pm 0.2$	$-1.0 \pm 0.2$	$-1.0 \pm 0.2$	$2.0 \pm 0.4$	$[0, 0, 0] \pm 5$	$\leq 4$	$[0, 20, 0] \pm 5$
	Dehydrated	Al(2)	$-3.0 \pm 0.5$	$2.0 \pm 0.2$	$2.0 \pm 0.2$	$-4.0 \pm 0.3$	$[0, 0, 0] \pm 5$	$11 \pm 5$	$[0, 90, 0] \pm 5$

fully dehydrated sample (Figure 5.3c, at the bottom). This behaviour corresponds to a continuous increase of the aluminium quadrupolar interaction upon water removal, consistent with previous reports on metal-doped zeolites<sup>46,218</sup> and quantum mechanical modelling (Tables A.4 and A.5).<sup>78</sup> The full set of  $^{27}\text{Al}$  and  $^1\text{H}$  hfis evaluated through the simulation of HYSCORE and ENDOR spectra (for the simulation of HYSCORE spectra, see Figures A.1 and A.2) are listed in Table 5.2.

Summarizing, the combination of CW-EPR and hyperfine techniques, provides evidence, in the hydrated sample, for solvated and mobile  $[\text{Cu}(\text{H}_2\text{O})_6]^{2+}$  species along with framework interacting species, which attain a partially solvated structure bearing intimate contact with the framework. Upon dehydration, the two species adopt a tetragonal planar coordination through coordinating oxygen donor atoms of the zeolite cage.

### 5.1.3 Nature of the Cu–O bonding interaction from $^{17}\text{O}$ EPR

Since the SOMO serves as the redox-active orbital in  $\text{Cu}^{\text{II}}$  systems, the covalency of this orbital is crucial for understanding the catalytic properties of Cu-based catalysts. The degree of covalency in the ligand–metal bond has far-reaching implications towards reactivity and catalysis as it is the key to activate directional long-range electron transfer pathways,<sup>219,220</sup> enhance catalyst stability<sup>221</sup> and determine the selective stabilization of intermediate species in redox reactions.<sup>222</sup> Detailed information on the Cu–O bonding interaction can be obtained through the detection of the  $^{17}\text{O}$  hyperfine interaction, which is a direct reflection of the spin delocalization over the coordinating ligands and a direct probe of the metal–ligand covalent character. To enable the detection of  $^{17}\text{O}$  hyperfine interactions, the zeolite framework has been enriched by following protocols developed by Morra *et al.*<sup>171</sup> and described in Section 4.2. Under the mild reaction conditions adopted in this work, both Al–O and Si–O bonds undergo  $^{17}\text{O}$  isotopic exchange, as confirmed by previous studies.<sup>171,202</sup> This is schematically shown in Figure 5.4a, where the exchangeable sites are highlighted. Orienta-

**Table 5.3:** Experimental  $^{17}\text{O}$  hyperfine coupling components and quadrupolar coupling constants used for the simulations of Davies ENDOR spectra in Figure 5.4. The hfi parameters satisfy simultaneously all the six field  $^{17}\text{O}$  ENDOR spectra. All hyperfine interactions are given in units of MHz, while angles are in degrees.

State		$a_{iso}$	$T_1$	$T_2$	$T_3$	$[\alpha, \beta, \gamma]$
Hydrated	$^{17}\text{O}(1)$	$-44.5 \pm 0.2$	$8.0 \pm 0.3$	$8.0 \pm 0.2$	$-16 \pm 0.4$	$[0, 90, 0] \pm 2$
	$^{17}\text{O}(2)$	$-10.0 \pm 0.2$	$2.0 \pm 0.2$	$2.0 \pm 0.3$	$-4.0 \pm 0.5$	$[0, 20, 0] \pm 2$
Dehydrated	$^{17}\text{O}(3)$	$-51.0 \pm 0.4$	$12.0 \pm 0.3$	$12.0 \pm 0.3$	$-24.0 \pm 0.4$	$[0, 90, 0] \pm 2$
	$^{17}\text{O}(4)$	$-41.0 \pm 0.5$	$9.5 \pm 0.3$	$9.5 \pm 0.3$	$-19.0 \pm 0.4$	$[0, 92, 0] \pm 2$

tionally selected  $^{17}\text{O}$  Q-band Davies ENDOR spectra of the hydrated and fully dehydrated zeolite are shown in Figure 5.4b and 5.4c, respectively.

The low field  $^{17}\text{O}$  ENDOR spectrum of the hydrated zeolite (Figure 5.4b) corresponds to a single crystal-like orientation and is characterized by an unresolved set of  $2I = 5$  quadrupole lines separated by  $2\nu_I$  and centered at a frequency corresponding to  $A/2$  (about 17 MHz,  $^{17}\text{O}(1)$  in Figure 5.4b). The higher-frequency component is more intense, probably due to hyperfine enhancement and/or due to RF conversion efficiency of the RF coils. A second oxygen ( $^{17}\text{O}(2)$  in Figure 5.4b) with a hyperfine coupling of the order of 12 MHz, close to the cancellation regime ( $2|\nu|I \approx |A|$ ), is also present and responsible for the resonance fixed at approximately 12 MHz.

To identify the oxygen ligand containing  $^{17}\text{O}$  and ascertain the presence of framework coordination, experiments were performed on the  $^{17}\text{O}$  isotopically enriched Cu-CHA(B) zeolite subsequently hydrated with normal water. The presence of  $^{17}\text{O}$  resonances (Figure A.3), similar to those reported in Figure 5.4b in the ENDOR spectra, demonstrates the presence of an intimate interaction of  $\text{Cu}^{\text{II}}$  species with the zeolite framework under hydrating conditions, supporting the assignment based on  $^{27}\text{Al}$  HYSCORE spectra.

By fitting the experimental spectra taken at various resonant magnetic field the full  $^{17}\text{O}$  interacting tensor for the two families of interacting nuclei was recovered with  $\mathbf{A}_{\text{O}(1)} = [-36.5 \ -36.5 \ -60.5]$  MHz and  $\mathbf{A}_{\text{O}(2)} = [-8 \ -8 \ -14]$  MHz whereby a negative sign was assumed, based on the negative nuclear  $g$  factor of  $^{17}\text{O}$  and in agreement with the results of DFT calculations, listed in Table A.4. The observed couplings can be assigned to equatorially ( $A_{\text{O}(1)}$ ) and axial ( $A_{\text{O}(2)}$ ) coordinating oxygen atoms, whereby the difference in the hyperfine coupling reflects the small overlap of the oxygen  $2p$  orbitals of the axial ligands with the Cu  $3d_{x^2-y^2}$  orbital, major contributor to the SOMO. The spin density on the two coordinating oxygens is estimated to be  $\rho_{\text{O}(1)} = 5.4\%$  and  $\rho_{\text{O}(2)} = 1.1\%$  (see Appendix A and Table A.6).

ENDOR spectra for the dehydrated zeolite (Figure 5.4c) provide a unique

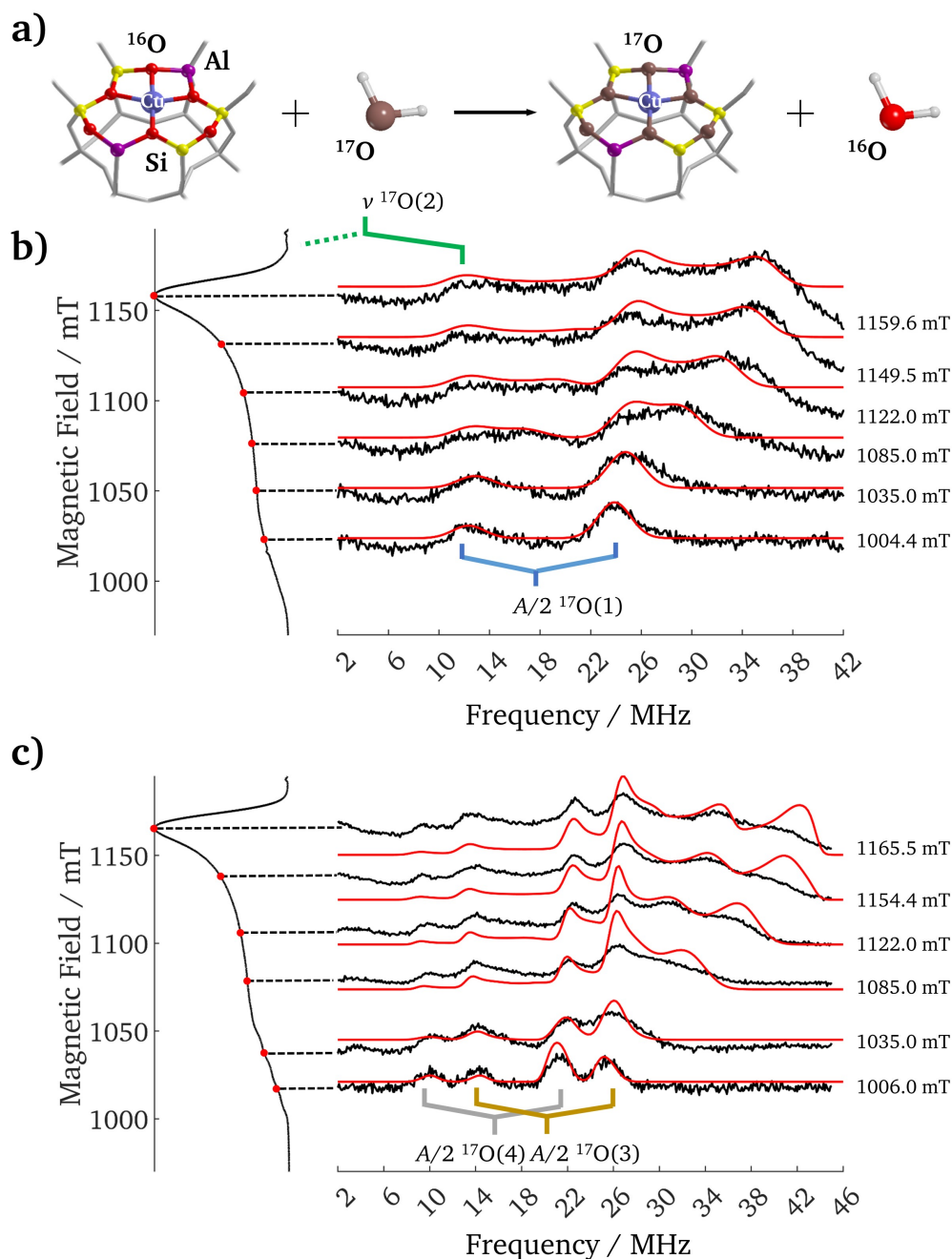


**Figure 5.4:** a) Schematic representation of the isotopic enrichment of the zeolite framework. b) Experimental (black) and simulated (red) Q-band  $^{17}\text{O}$  ENDOR spectra recorded at different magnetic field settings of  $^{17}\text{O}$  isotopically enriched Cu-CHA(B) fully hydrated with  $\text{H}_2^{17}\text{O}$ . c) Corresponding experiment performed on fully dehydrated  $^{17}\text{O}$  enriched Cu-CHA(B). The ESE spectra with the corresponding field positions at which the ENDOR spectra were taken are plotted on the left-hand side. All spectra were recorded at 20 K. This figure was first published in Bruzzese *et al.*<sup>78</sup>

level of detail on the dehydrated  $\text{Cu}^{\text{II}}$  docking site, giving evidence of two distinct oxygen species coordinated to the  $\text{Cu}^{\text{II}}$  species. At variance with the fully hydrated system, the single crystal-like spectrum recorded at 1006.0 mT is characterized by two doublets separated by  $2\nu_I$  and centered at 37 MHz and 30 MHz, respectively. Simulation of the field dependent spectra allowed to extract the full  $^{17}\text{O}$   $\mathbf{A}$ -tensors (Table 5.3 and Figure A.4). The larger  $^{17}\text{O}$  hyperfine couplings imply an increased spin density transfer over the framework oxygen donor atoms with respect to the hydrated system equivalent to  $\rho_{\text{O}(3)} = 8.5\%$  and  $\rho_{\text{O}(3)} = 6.6\%$ . These values correspond to the covalent contribution to the SOMO per O atom. Considering four coordinating oxygen atoms (Figure 5.1a and Table A.7), the wave function is composed by a 70% contribution from Cu  $3d_{x^2-y^2}$  orbital with the remaining 30% being shared among the  $2p$  orbitals of the lattice oxygen ligands.

Based on the ENDOR linewidth, we estimate an upper limit of the order of 7 MHz for the  $^{17}\text{O}$  nuclear quadrupole coupling constant ( $e^2qQ/h$ ) for both anhydrous and hydrated conditions. These values are consistent with those reported from  $^{17}\text{O}$  NMR studies<sup>201</sup> for Brønsted acid sites of 6.6 MHz and in line with computed values reported in Tables A.4 and A.5.

The contribution from the different species were properly weighted in the simulation in order to better fit the experimental plot.  $^{17}\text{O}(3)$  and  $^{17}\text{O}(4)$  species were considered in 1:1 ratio, whereas  $^{17}\text{O}(1)$  bestows the 95% of the simulated signal and  $^{17}\text{O}(2)$  accounts for the remaining 5%. H(1),  $^{17}\text{O}(1)$ ,  $^{17}\text{O}(3)$  and  $^{17}\text{O}(4)$  hyperfine tensors are found to be in the same plane (same Euler  $\beta$  angle which expresses the orientation of  $\mathbf{A}$ -tensor with respect to  $\mathbf{g}$ -tensor). In the same way, Al(1), H(2) and  $^{17}\text{O}(2)$  hfi tensors are almost collinear to each other. A summary of the  $^{17}\text{O}$  spin Hamiltonian parameters adopted for simulating the ENDOR spectra is given in Table 5.3.

#### 5.1.4 Microscopic structure of $\text{Cu}^{\text{II}}$ and Al siting from computational modelling

To transpose the spectroscopic findings into atomistic models, DFT calculations were carried out for copper docking sites differing in the Al distribution, namely two Al in two adjacent D6MRs, two Al in the same D6MR at second-nearest-neighbour positions and two Al in the same D6MR at third-nearest-neighbour positions (1Al, 2Al-2NN, 2Al-3NN in Figure 5.5a). All the aluminium distributions obey the Löwenstein rule avoiding two adjacent sites to be occupied by Al ions.<sup>158</sup>

The relative energy of  $\text{Cu}^{\text{II}}$  at the three sites was computed for two different Si/Al ratios (Si/Al = 11 and Si/Al = 5). The optimized structures all con-

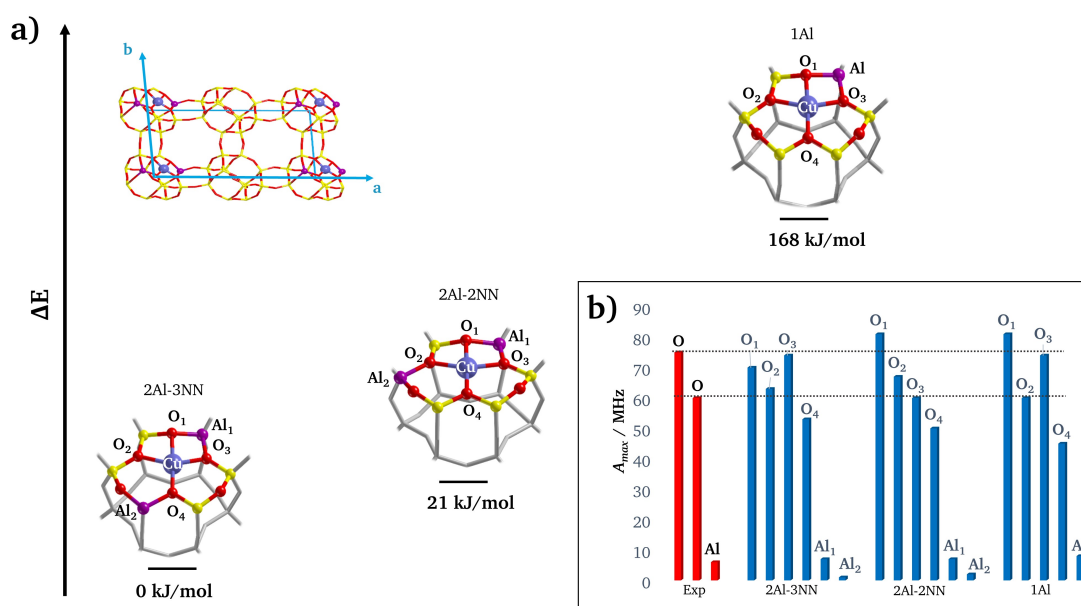


**Figure 5.5:** a) B3LYP-D3(ABC)/pob-TZVP fully optimized structures of dehydrated Cu-CHA models (Si/Al = 11) by employing three different Al distributions, namely 2Al-3NN, 2Al-2NN and 1Al. The corresponding relative electronic energy per unit cell is shown for each structure. The unit cell (top left of the figure) is oriented according to the lattice vectors reported in cyan. b) Comparison of experimental (red) and computed (blue) maximum hyperfine coupling values ( $A_{\text{max}}$ ) for  $^{17}\text{O}$  and  $^{27}\text{Al}$  nuclei for the three different Al distributions illustrated in a). The black dashed lines represent the experimental range of  $A_{\text{max}}$  for  $^{17}\text{O}$  nuclei. This figure was first published in Bruzzese *et al.*<sup>78</sup>

verged to a tetragonal coordination by the lattice oxygen donor atoms (henceforth named  $[\text{Cu}^{\text{II}}(\text{O-6MR})_4]$ ). The most energetically stable configuration was obtained for 2Al at third-nearest-neighbour (2Al-3NN) positions in a 6MR unit independent of the Si/Al ratio, in agreement with the previous evidences.<sup>26,69</sup>

For each model, the spin Hamiltonian parameters were calculated and compared to the experimental data. The computed  $g$ - and copper  $A$ -tensors obtained by using the geometry optimized structures are reported in Table A.2 and are in qualitative agreement with the experimental data, but do not allow to confidently discriminate among the three different possible structures presented in Figure 5.5. This is unsurprising as the precise and robust calculation of  $g$ - and  $A$ -tensors for  $\text{Cu}^{\text{II}}$  systems is still a great challenge for quantum chemistry methods and only qualitative agreements are usually obtained.<sup>74–76</sup> On the other hand, the prediction of hyperfine couplings for lighter elements (due to negligible spin-orbit coupling and a more accurate determination of the Fermi contact term) is far more reliable.<sup>77</sup> In Figure 5.5b the maximum hyperfine coupling values ( $A_{\text{max}} = |a_{\text{iso}} + 2T|$ ) for  $^{17}\text{O}$  and  $^{27}\text{Al}$  nuclei is plotted for the three different structures and compared with the experimental values. Examination of the computed values shows that the experimental  $^{27}\text{Al}$  couplings are quantitatively reproduced, however they are not diagnostic as all models yield very similar values. In particular, in the case of the 2Al models (2Al-3NN and 2Al-2NN in Figure 5.5b) the computed couplings display analogous values ( $\approx 7$  MHz and  $\approx 1$  MHz) irrespectively of the Al location. While the 7 MHz coupling is in agreement with the experimental value of 6 MHz, typical for Cu loaded zeolites,<sup>45</sup> the 1 MHz coupling is too small to be confidently measured, making it impossible to discriminate between 2Al and 1Al sites.  $^{17}\text{O}$  hyperfine couplings prove to be a far more sensitive structural probe. The experimental data (Table 5.3) point to two sets of  $^{17}\text{O}$  nuclei characterized by different couplings, whereas four different couplings are computed for all models. However, inspections of Figure 5.5b shows that only for 2Al-3NN two classes of alike couplings ( $\text{O}_1$ ,  $\text{O}_2$  and  $\text{O}_3$ ,  $\text{O}_4$ ) can be recognized, with values falling within the experimental range, while 1Al and 2Al-2NN models feature remarkably different couplings for all four oxygen nuclei (see also the simulation of the  $^{17}\text{O}$  ENDOR spectra considering the DFT calculated hyperfine couplings in Figure A.5).

The differences in the  $^{17}\text{O}$  hyperfine couplings do not arise from differences in the Cu–O bond lengths (Table A.7), but rather in slightly different spin density transfer over the coordinating oxygen atoms. This can be traced back to geometric distortions from square planar coordination, resulting in a decreased overlap between the Cu  $3d_{x^2-y^2}$  orbital and the O  $2p$  orbitals. A similar effect is observed for  $[\text{CuCl}_4]^{2-}$  complexes where the covalent contribution of the ligands to the SOMO is found to increase from  $D_{2d}$  to  $D_{4h}$  symmetries due to the



increasing overlap between the Cu  $3d_{x^2-y^2}$  and the Cl  $3p$  orbitals in the two geometries.<sup>223</sup> The three different sites considered in this work feature very similar Cu–O distances but slightly different geometric distortions, leading to asymmetries in the spin delocalization, characteristic for the different sites. Crucially, asymmetries in the spin delocalization are of outmost relevance as they report on the covalent character of each ligand–metal bond, which ultimately design preferential electron transfer pathways.<sup>219,220</sup>

Overall, this analysis shows that not only structure 2Al-3NN is the most energetically favoured, but it is also the only one for which a satisfactory agreement between computed and experimental spin Hamiltonian parameters is obtained. In turn, this allows to confidently conclude that 2Al-3NN sites are those dominantly populated by  $\text{Cu}^{\text{II}}$  species under the experimental conditions.

A similar analysis on the hydrated system, yields a different scenario for the  $\text{Cu}^{\text{II}}$  docking and allows the assessment of migration pathways induced by hydration/dehydration processes. Based on experimental UV-vis, IR and XAS spectra of Cu-CHA in hydrated state at room temperature, previous studies have assumed the presence of two types of  $\text{Cu}^{\text{II}}$  complexes, regardless the copper loading and the composition of the zeolite: the former are divalent complexes charge-compensated by a pair of Al atoms (such as  $[\text{Cu}(\text{H}_2\text{O})_6]^{2+}$  or  $[\text{Cu}^{\text{II}}(\text{H}_2\text{O})_n(\text{O}-8\text{MR})_{6-n}]$ ); the latter are monovalent complexes whose charge is compensated by one Al atom (e.g.  $[\text{Cu}^{\text{II}}(\text{OH})(\text{H}_2\text{O})_5]$  or  $[\text{Cu}^{\text{II}}(\text{OH})(\text{H}_2\text{O})_n(\text{O}-8\text{MR})_{5-n}]$ ).<sup>26,169</sup> However, the discrimination among such hydrated complexes is hampered by the resolution of the experimental techniques mentioned above. To shed light on the nature of the hydrated species, the relative stability of  $\text{Cu}^{\text{II}}$  species at different sites has been assessed as a function of hydration conditions by considering the effect of a single water molecule coordinated to  $\text{Cu}^{\text{II}}$  ions hosted in 6MRs or 8MRs sites, as illustrated in Figure 5.6a and b.

For a dehydrated  $\text{Cu}^{\text{II}}$  cation, the 6MR site is far more stable than the 8MR because of the stronger binding to the four framework oxygen atoms in a tetragonal geometry. Energetic considerations suggest thus such a location is the preferred one for the dehydrated material, in agreement with several experimental and theoretical studies.<sup>21,23,224</sup> However, the adsorption of water molecules completely alters the relative stabilities: with one water ligand, the stability of both sites becomes similar (Figure 5.6a). Further addition of  $\text{H}_2\text{O}$  molecules increases the energy gap between the different cage locations pointing out that, in hydrated and partially hydrated conditions (both experimentally observed), 8MR sites are more stable than 6MR, in agreement with the findings of Kerkeni *et al.*<sup>225</sup> Details on such results are reported in Figure A.6.

The computed  $^1\text{H}$  hyperfine couplings for the  $[\text{Cu}(\text{H}_2\text{O})_6]^{2+}$  (Figure 5.7a) and interfacial Cu species (Figure 5.7b) are in quantitative agreement with the

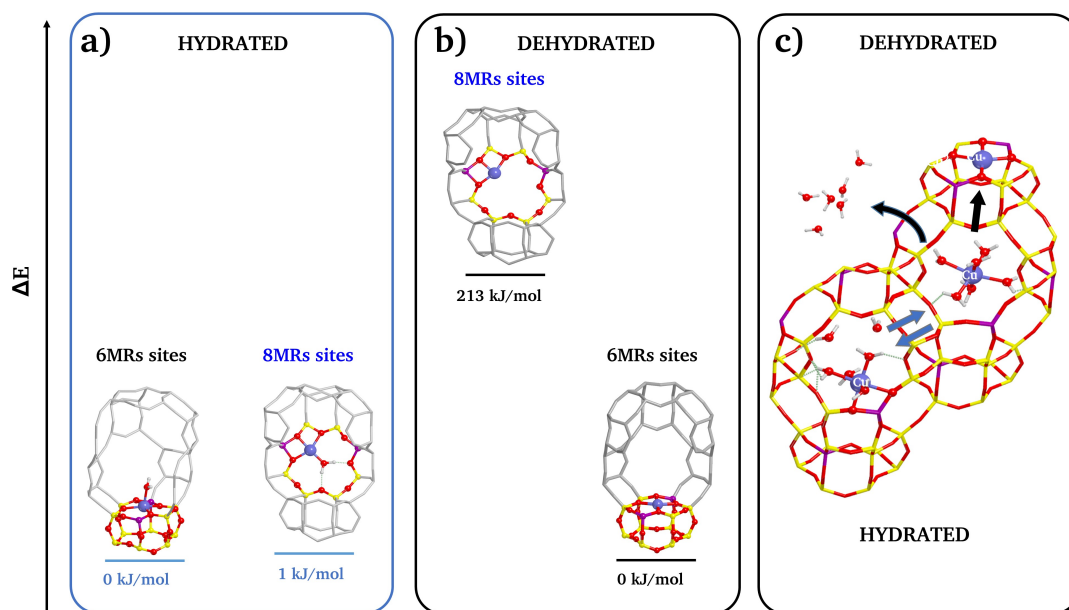


**Figure 5.6:** a) Hydrated and b) dehydrated  $\text{Cu}^{\text{II}}$  species in 6MRs and 8MRs sites with the corresponding relative electronic energy per unit cell. c) Picture of the  $\text{Cu}^{\text{II}}$  dynamics inside the CHA framework due to the presence of water molecules. Some relevant atoms are represented by balls-and-sticks (colour code: medium blue Cu, yellow Si, violet Al, red O, white H). This figure was first published in Bruzzese *et al.*<sup>78</sup>

experimental values and characteristic for axially (small hyperfine coupling) and equatorially (large hyperfine coupling) water bound protons (Table A.4). Computed oxygen hyperfine couplings for these structures (Table A.4) reproduce the experimental values showing a set of large  $a_{\text{iso}}$  couplings (-45 MHz and -55 MHz) related to equatorially coordinated oxygen ligands and a set of small values (-8 MHz and -6 MHz) associated to axially coordinated oxygen ligands.

### 5.1.5 Summary

In summary, two  $\text{Cu}^{\text{II}}$  complexes are identified under hydrating conditions, i.e.  $[\text{Cu}^{\text{II}}(\text{H}_2\text{O})_6]@\text{CHA}$  (Figure 5.7a) and an interfacial  $[\text{Cu}^{\text{II}}(\text{H}_2\text{O})_4(\text{O}-8\text{MR})_2]$  complex (Figure 5.7b), whereby the notation @CHA indicates the hexaaquacopper complex encapsulated in the Chabazite's largest cage. The CHA cage has a diameter of 1.2 nm ensuring the possibility of free tumbling of the water complex at room temperature and explaining the motionally averaged spectrum observed at RT. This mobile species coexists along with the complex  $[\text{Cu}^{\text{II}}(\text{H}_2\text{O})_4(\text{O}-8\text{MR})_2]$  (Figure 5.6c and Equation 5.1), where two water ligands are substituted by two oxygen donor atoms belonging to the 8MR site as demonstrated by  $^{17}\text{O}$  ENDOR spectra recorded on the  $^{17}\text{O}$ -exchanged zeolite in the presence of  $\text{H}_2^{16}\text{O}$  (Figure

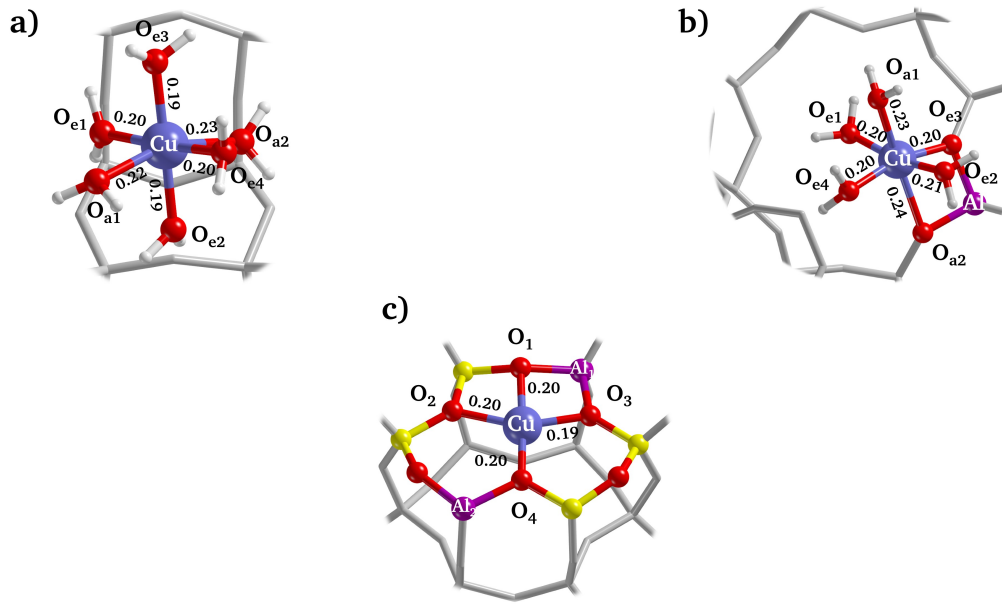
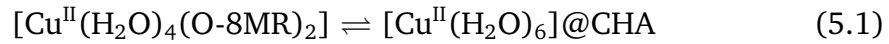
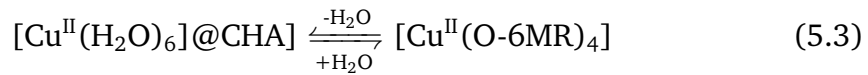
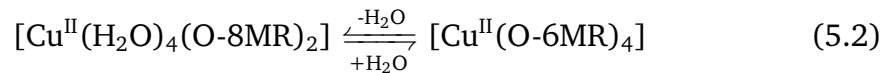


**Figure 5.7:** a)  $[\text{Cu}(\text{H}_2\text{O})_6]^{2+}$  in the Chabazite's largest cage, b)  $[\text{Cu}^{\text{II}}(\text{H}_2\text{O})_4(\text{O}-8\text{MR})_2]$  complex and c)  $[\text{Cu}^{\text{II}}(\text{O}-6\text{MR})_4]$  complex at the 2Al-3NN site. Cu–O bond lengths are indicated in nm. The label of relevant nuclei is reported whereas Si and H atoms are shown in yellow and white, respectively. The remaining framework atoms are represented by grey sticks. This figure was first published in Bruzzese *et al.*<sup>78</sup>

A.3).



The hydration/dehydration processes in Cu-CHA can therefore be described in terms of a dynamic conversion (Equations 5.2 and 5.3) between water solvated species and an interfacial complex  $[\text{Cu}^{\text{II}}(\text{O}-6\text{MR})_4]$ , whereby the 6MR cage behaves as a tetradentate ligand as shown in Figure 5.7c.



The  $[\text{Cu}^{\text{II}}(\text{O}-6\text{MR})_4]$  interfacial complexes (Figure 5.7c) feature a SOMO with predominant metal  $3d_{x^2-y^2}$  character and a covalent contribution of about 30% from the coordinating framework oxygen donor atoms. Importantly, DFT calculations demonstrate that the spin density distribution over the coordinating oxygens and the corresponding  $^{17}\text{O}$  hyperfine couplings are significantly dependent upon the Al distribution in the 6MR site, allowing to discriminate between different Al locations. In particular, for the low Cu loading considered in this

work, the 2Al-3NN site, characterized by 2 Al atoms separated by two Si, not only has the lowest energy but also provides the better agreement between calculated and experimental  $^{17}\text{O}$  hyperfine couplings constants.

The new methodology and associated new knowledge that emerges from this study will need to be applied systematically to other framework topologies and comparison will need to be set to catalysts characterized by different Si/Al and Cu/Al ratios. This systematic approach will form the basis to correlate catalytic performances to the Cu (and in general paramagnetic metal species) location at specific zeolite sites. Moreover, while providing a strategy to optimize catalyst compositions (Al distribution, Cu loading, etc.), the detection of  $^{17}\text{O}$  hyperfine couplings provides an effective means to selectively probe the framework lability at open-shell metal centers in zeolite. Most importantly, the exquisite sensitivity of such couplings enables to account for minute structural differences related to the Al distribution and identify the Al siting in the most stable  $\text{Cu}^{\text{II}}$  coordination, a long-standing issue in the field.

## 5.2 The structure of monomeric $[\text{Cu}^{\text{II}}(\text{OH})]^+$ species in Chabazite

Monomeric hydroxo- $\text{Cu}^{\text{II}}$  species are of particular interest in copper-loaded zeolites as they are considered as active redox species.<sup>17,24,226,227</sup> Indeed,  $[\text{Cu}(\text{OH})]^+$  moieties have been invoked as active<sup>197,228–230</sup> and pre-active<sup>14,198</sup> species in the catalytic conversion of methane to methanol at low temperatures. Despite their relevance, their atomistic and electronic structure is ill-defined and oddly described in literature as an approximately trigonal planar coordination.<sup>51,197</sup> Such geometry is affected by a pseudo Jahn-Teller effect (PJTE),<sup>231,232</sup> which is taken as the basis for explaining the lack of EPR signal corresponding to such monomeric  $\text{Cu}^{\text{II}}$  species.<sup>29,51</sup>

Recent studies<sup>21,24,26,27,233</sup> indicate the presence of two major monomeric Cu sites in activated Cu-CHA, namely interfacial complexes coordinated with four oxygen donor atoms of the 6MR cavities ( $[\text{Cu}^{\text{II}}(\text{O-6MR})_4]$ ), whereby the  $\text{Cu}^{\text{II}}$  is stabilized by two neighboring charge-balancing  $\text{Al}^{3+}$  framework ions, and  $[\text{Cu}(\text{OH})]^+$  species at 8MR cages next to an isolated  $\text{Al}^{3+}$  ion. The relative population of the two species depends on the number and distribution of Al ions in the framework and on the Cu/Al ratio. Materials with low Si/Al and Cu/Al ratios should contain predominantly  $[\text{Cu}^{\text{II}}(\text{O-6MR})_4]$  species, while materials with high Si/Al and Cu/Al ratios are dominated by  $[\text{Cu}(\text{OH})]^+$ .<sup>211,234</sup>

First suggested by Valyon,<sup>235</sup>  $[\text{Cu}(\text{OH})]^+$  has been identified in high loaded Cu-CHA (Si/Al = 11-15) after dehydration in  $\text{O}_2/\text{He}$  by Giordanino and Borfec-

chia *et al.*<sup>24,169</sup> through characteristic IR stretching and bending bands at  $3656\text{ cm}^{-1}$  and  $905\text{ cm}^{-1}$ . EPR spectroscopy has been used to indirectly evaluate the amount of  $[\text{Cu}^{\text{II}}(\text{OH})]^+$ ,<sup>29,51–53</sup> however, no direct detection of these species in dehydrated Cu-CHA has been reported so far. In this section, the identification of the EPR signature of framework bound  $[\text{Cu}^{\text{II}}(\text{OH})]^+$  species is reported, elucidating their structure that is different from past assignments.<sup>24,25,29,51,197,211,226</sup>

### 5.2.1 Identification of the EPR signature of $[\text{Cu}^{\text{II}}(\text{OH})]^+$

The structural requirement for the stabilization of  $[\text{Cu}^{\text{II}}(\text{OH})]^+$  is based on the availability of single Al framework sites, which are assumed to be populated after 2Al sites.<sup>26</sup> Paolucci *et al.*<sup>26,211</sup> computed a Cu-site compositional phase diagram for  $\text{O}_2$ -activated Cu-CHA, under the assumptions that Al is distributed randomly and the Löwenstein's rule<sup>158</sup> is obeyed. Based on this diagram (Figure 5.8a), four different Cu-CHA compositions corresponding to different  $[\text{Cu}^{\text{II}}(\text{OH})]^+$  predicted populations, ranging from approximately 0 (A in Figure 5.8a) to about 40% of total Cu (point D in Figure 5.8a), were chosen (see Section 4.1 for details on synthetic procedures adopted). The samples were activated by adopting conditions known to maximize  $[\text{Cu}^{\text{II}}(\text{OH})]^+$  sites (dehydration at 523 K under  $\text{O}_2$  atmosphere, see also Section 4.2.1)<sup>226</sup> and the corresponding EPR spectra are shown in Figure 5.8b.

The CW-EPR spectrum of Cu-CHA(A) (spectrum A in Figure 5.8b) shows the characteristic hyperfine structure due to coupling of the electronic spin  $S = 1/2$  of the  $\text{Cu}^{\text{II}}$  ion with the nuclear spin  $I = 3/2$  of both copper isotopes  $^{63}\text{Cu}$  and  $^{65}\text{Cu}$  (natural abundances 69.17% and 30.83% respectively) with  $g_{\parallel} > g_{\perp} > g_e$ . Computer simulation of the spectrum (Figure 5.9a and Table 5.4) reveals the contribution of a single species with spin Hamiltonian parameters corresponding to the  $[\text{Cu}^{\text{II}}(\text{O-6MR})_4]$ . In Section 5.1 the SOMO character was identified to be predominantly Cu  $3d_{x^2-y^2}$  with a covalent contribution of about 30% from the coordinating framework oxygen donor atoms.<sup>78</sup> The EPR spectrum of Cu-CHA(B) (Figure 5.8b) shows the presence of at least two  $\text{Cu}^{\text{II}}$  species with similar parameters amenable to  $[\text{Cu}^{\text{II}}(\text{O-6MR})_4]$  with slightly different local environment (species C and D in Table 5.1 and Figure 5.9b).<sup>51,78</sup> Moving towards a composition favoring the presence of  $[\text{Cu}^{\text{II}}(\text{OH})]^+$  species (point C in Figure 5.8a) a new quartet of lines appears in the low field region of the spectrum, highlighted by the stick diagram shown on the top of Figure 5.8b. The spin Hamiltonian parameters of the new species, assessed via computer simulation (Figure 5.9c), are characterized by reduced  $g_{\parallel} = 2.290$  and  $A_{\parallel} = 410\text{ MHz}$  values (Table 5.4), still in agreement with a dominant metal  $3d_{x^2-y^2}$  character of the SOMO (see paragraph 5.2.2). These values remain constant in the interval 10K

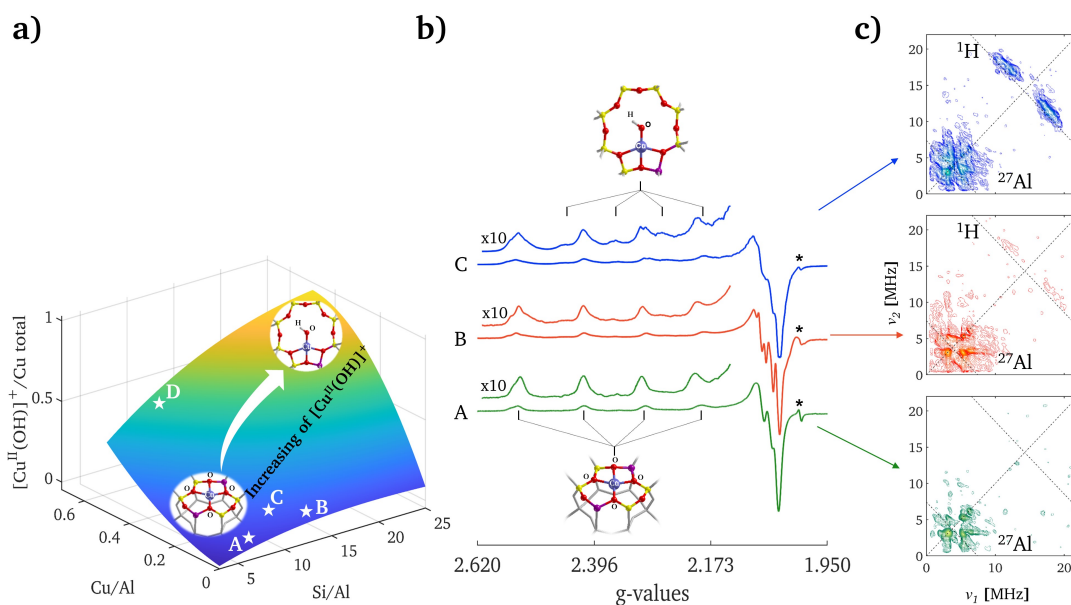


**Figure 5.8:** a) Computed Cu speciation as function of zeolite chemical composition space (Si/Al and Cu/Al ratio). The diagram is drawn based on data taken from the work of Paolucci *et al.*<sup>211</sup> The compositions of the synthesized Cu-CHA samples are indicated by white stars, The labelling A-D for the Cu-CHA samples is the same as adopted in Section 4.1. b) CW-EPR spectra of O<sub>2</sub>-activated CuCHA samples measured at 77 K. The asterisk indicates a carbon radical signal. Stick diagrams indicate the spectral features associated to [Cu<sup>II</sup>(O-6MR)<sub>4</sub>] in A and [Cu<sup>II</sup>(OH)]<sup>+</sup> in B and C. The spectrum of Cu-CHA(D) (label D in Figure a) is shown in Figure 5.9d. c) X-band <sup>1</sup>H HYSCORE spectra recorded at a magnetic field position corresponding to  $g=2.072$  ( $g_{\perp}$ ),  $\tau = 130$  ns and  $T=10$  K. This figure was first published in Bruzzese *et al.*<sup>79</sup>

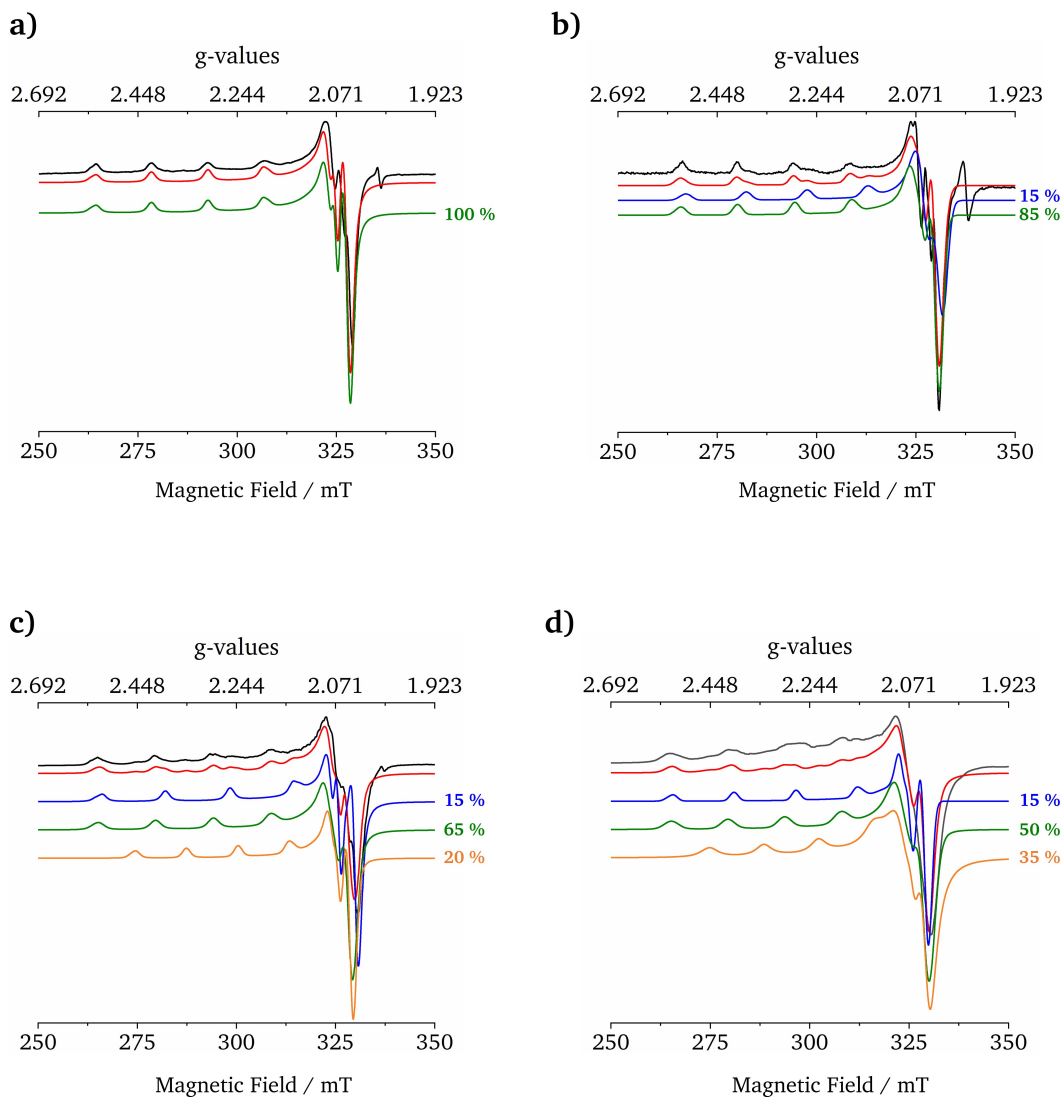


**Figure 5.9:** Experimental (black lines) and computer simulations (red lines) of CW-EPR spectra recorded at 77 K of  $\text{O}_2$ -activated a) Cu-CHA(A) (Si/Al=7; Cu/Al=0.001), b) Cu-CHA(B) (Si/Al=15; Cu/Al=0.005), c) Cu-CHA(C) (Si/Al=12; Cu/Al=0.09), d) Cu-CHA(D) (Si/Al=12; Cu/Al=0.67). The contribution of each individual Cu species together with their weight used for the overall simulations are shown in green, blue and orange for  $[\text{Cu}^{\text{II}}(\text{O-6MR})_4]$  (species C in Table 5.1),  $[\text{Cu}^{\text{II}}(\text{O-6MR})_4]$  (species D in Table 5.1) and  $[\text{Cu}^{\text{II}}(\text{OH})]^+$ . This figure was first published in Bruzzese *et al.*<sup>79</sup>

**Table 5.4:** Experimental Cu  $g$ - and  $A$ -tensors retrieved from the simulations of the CW-EPR spectra recorded at 77 K reported in Figure 5.8b and 5.9. Only the absolute values of the hyperfine components are extracted from the spectra. Hyperfine couplings are given in units of MHz. Linewidth for isotropic broadening taken peak-to-peak (lwpp) is given in mT. Peak-to-peak refers to the horizontal distance between the maximum and the minimum of a first-derivative lineshape. Uncertainty of 0.002, 5 MHz, 0.3 mT and 6% were estimated for the  $g$ -values, hyperfine couplings, lwpp and weights, respectively.

Samples	Si/Al; Cu/Al	Weight	Species	$g_{\perp}$	$g_{\parallel}$	$A_{\perp}$	$A_{\parallel}$	lwpp	
								Gaussian	Lorentzian
Cu-CHA(A)	7; 0.001	100%	[Cu <sup>II</sup> (O-6MR) <sub>4</sub> ]	2.075	2.352	35	470	1.8	1.0
Cu-CHA(B)	15; 0.005	85%	[Cu <sup>II</sup> (O-6MR) <sub>4</sub> ]	2.075	2.352	35	470	1.8	1.0
		15%	[Cu <sup>II</sup> (O-6MR) <sub>4</sub> ]	2.072	2.325	35	490	1.0	1.0
Cu-CHA(C)	12; 0.09	65%	[Cu <sup>II</sup> (O-6MR) <sub>4</sub> ]	2.075	2.352	35	470	1.8	1.0
		15%	[Cu <sup>II</sup> (O-6MR) <sub>4</sub> ]	2.072	2.325	35	490	1.0	1.0
		20%	[Cu <sup>II</sup> (OH)] <sup>+</sup>	2.072	2.290	30	410	1.5	0.5
Cu-CHA(D)	12; 0.67	50%	[Cu <sup>II</sup> (O-6MR) <sub>4</sub> ]	2.075	2.352	47	460	3.0	0.5
		15%	[Cu <sup>II</sup> (O-6MR) <sub>4</sub> ]	2.072	2.329	35	500	2.0	0.0
		35%	[Cu <sup>II</sup> (OH)] <sup>+</sup>	2.072	2.290	45	410	0.0	2.7

– RT. The same new species is present also in Cu-CHA(D), although the EPR spectrum becomes more complex as the amount of Cu<sup>II</sup> increases (see Figure 5.9d).

As reported in paragraph 2.4.2, Larsen and co-workers used the empirical correlations between  $A_{\parallel}$  and  $g_{\parallel}$  to infer the formal charge of Cu species in zeolites.<sup>34,108</sup> The Peisach-Blumberg correlation plot for [Cu<sup>II</sup>(O-6MR)<sub>4</sub>] and [Cu<sup>II</sup>(OH)]<sup>+</sup> species together with two model compounds [Cu(H<sub>2</sub>O)<sub>6</sub>]<sup>2+</sup> and [Cu(OH)<sub>4</sub>]<sup>2-</sup> is shown in Figure 5.10. The parameters of the Cu<sup>II</sup> complex at the 6MR position ([Cu<sup>II</sup>(O-6MR)<sub>4</sub>]) fall in the region where neutral oxygen coordinated copper complexes are expected. This is coherent with the computed Mulliken charge on Cu equal to +0.7 and the fact that Cu<sup>II</sup> is coordinated by four O<sup>2-</sup> ions and stabilized by two Al<sup>3+</sup> ions, leading to a neutral complex. Indeed the observation of non-negligible spin density on the Al<sup>3+</sup> (see Figure 5.3c) substantiate this notion, pointing to a situation similar to the case of contact ion pairs in solutions. In a similar way, the [Cu<sup>II</sup>(OH)]<sup>+</sup>, whereby the single positive charge is balanced by a single Al<sup>3+</sup> ion, remains in this “neutral region” but shows decreased  $g_{\parallel}$  and  $A_{\parallel}$  values. The  $g$  factor is consistent with the hydroxo complex while the reduced  $A_{\parallel}$  coupling concurs with departure from a square planar complex as reported by Peisach<sup>107</sup> and coherent with the structure derived in paragraph 5.2.2.

The distinctive feature of the [Cu<sup>II</sup>(OH)]<sup>+</sup> species is expected to be the <sup>1</sup>H ( $I=1/2$ ) hyperfine coupling of the coordinated hydroxo group. This is too small to be detected in standard CW-EPR experiments but can be measured by hyper-



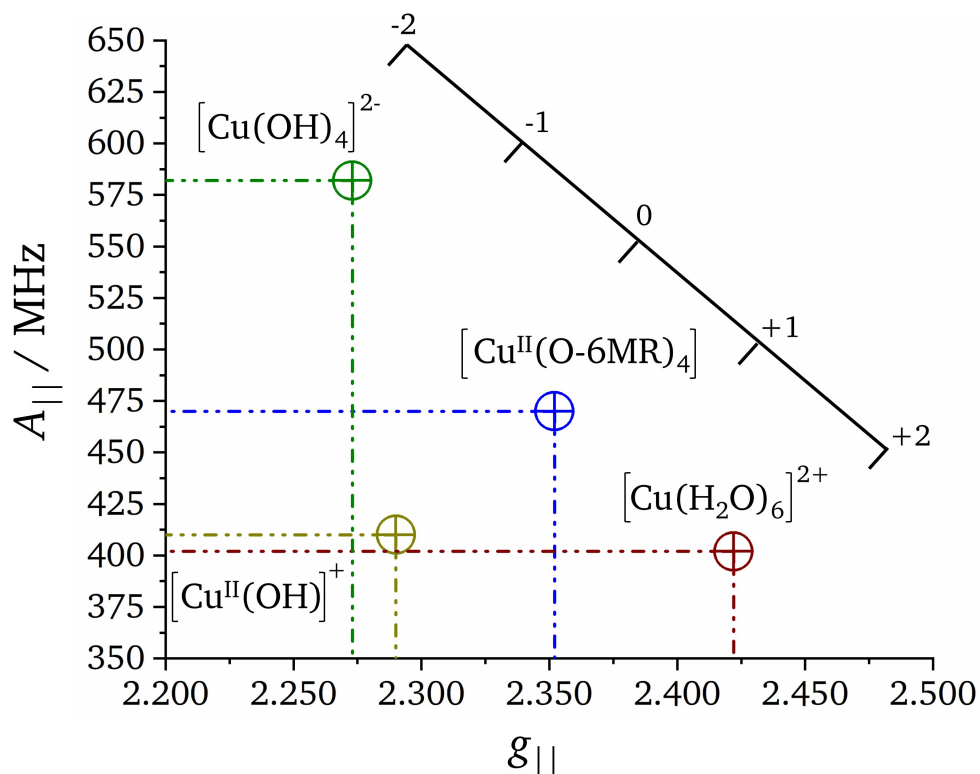


**Figure 5.10:** Peisach-Blumberg plot correlating  $A_{||}$  and  $g_{||}$  for the copper interfacial complexes  $[\text{Cu}^{\text{II}}(\text{O-6MR})_4]$ ,  $[\text{Cu}^{\text{II}}(\text{OH})]^+$  and two solution model compounds. This figure was first published in Bruzzese *et al.*<sup>79</sup>

fine techniques.

HYSCORE experiments were therefore used to interrogate each sample and the spectra, recorded at a magnetic field corresponding to  $g_{\perp}$  component of the CW-EPR spectrum, are presented in Figure 5.8c. It is important to note that under the experimental conditions employed, Cu coordinated to water is absent<sup>24,226</sup> and the only source of significant  $^1\text{H}$  hyperfine coupling must arise from coordinated hydroxo ligands. All HYSCORE spectra display a complex signal in the low frequency region of the spectrum due to the interaction of the unpaired electron with a nearby  $^{27}\text{Al}$  nucleus ( $I=5/2$ ).<sup>44</sup> While no  $^1\text{H}$  features are present in the HYSCORE spectrum of Cu-CHA(A), a pair of elongated cross-peaks centered at the  $^1\text{H}$  Larmor frequency and separated by approximately 13 MHz starts to appear in Cu-CHA(B) and dominates the spectrum of Cu-CHA(C) in Figure 5.8c. Computer simulation of HYSCORE spectra recorded at different magnetic field settings reported in Figure B.1, allowed recovering the full  $^1\text{H}$  hyperfine tensor  $\mathcal{A}_{\text{H}} = [-13.0 \ -4.5 \ +11.5]$  MHz (Table 2), whereby the absolute signs of the hyperfine tensors have been assigned according to *ab initio* computations (see paragraph 5.2.2).

HYSCORE experiments indicate that large proton couplings, amenable to Cu coordinated to hydroxo ligands, emerge at zeolites compositions in agreement

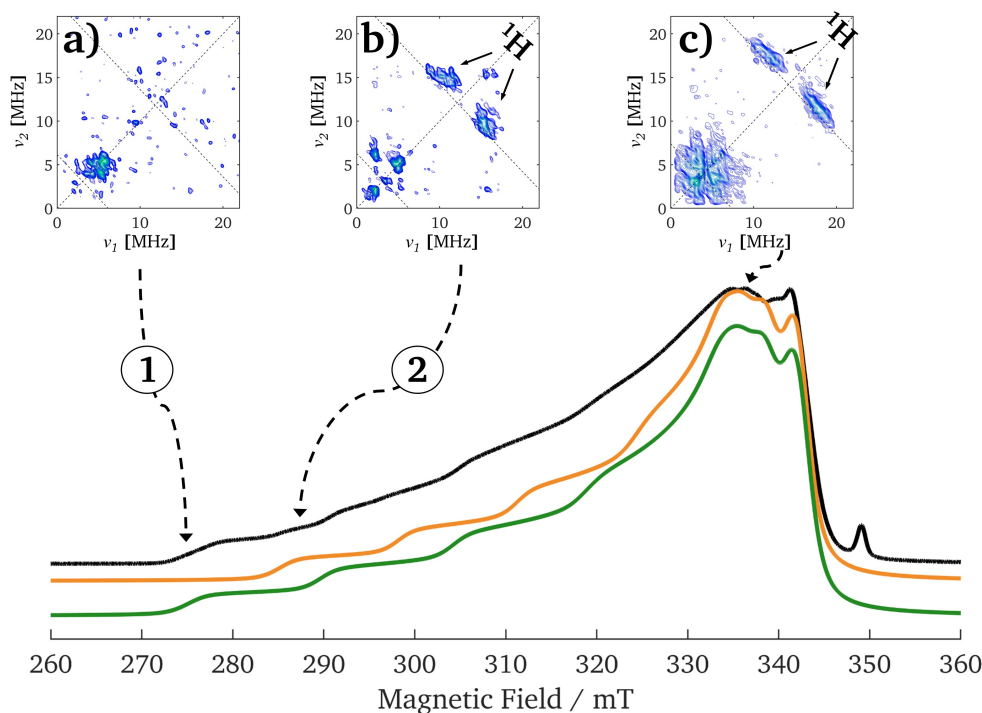


**Figure 5.11:** ESE detected EPR spectrum of Cu-CHA(C). Simulation of the two main species contributing the spectrum are shown in yellow ( $[\text{Cu}^{\text{II}}(\text{OH})]^+$ ) and green ( $[\text{Cu}^{\text{II}}(\text{O-6MR})_4]$ ). a), b) and c) are the HYSCORE spectra recorded at the magnetic field positions indicated by the arrows and  $T=10$  K. This figure was first published in Bruzzese *et al.*<sup>79</sup>

with predictions based on the distribution reported in Figure 5.8a. To correlate the observed  $^1\text{H}$  hyperfine coupling with the specific EPR features observed in Cu-CHA(C), selective HYSCORE experiments have been carried out at EPR transitions pertaining exclusively to such species and they are reported in Figure 5.11a-c. Figure 5.11 shows the ESE detected EPR spectrum of Cu-CHA(C) along with the simulation of the two main contributing species ( $[\text{Cu}^{\text{II}}(\text{O-6MR})_4]$  green line and  $[\text{Cu}^{\text{II}}(\text{OH})]^+$  in orange) identified by simulation of the CW experiments (Figure 5.9). The simulated components show that the spectral features of the two species overlap at high field ( $g_{\perp}$ ), while they are sufficiently separated at low field to allow for selective excitation of the  $^1\text{H}$  NMR transitions. The HYSCORE spectrum recorded at position 1 (Figure 5.11a) shows no trace of  $^1\text{H}$  coupling, while clearly showing the expected  $^{27}\text{Al}$  signal. The corresponding spectrum recorded at position 2 (Figure 5.11b), coinciding with the  $m_I = -3/2$  transition of the second  $\text{Cu}^{\text{II}}$  species (orange trace) shows the distinct  $^1\text{H}$  cross peaks, allowing to unambiguously assign this species to the monomeric hydroxo- $\text{Cu}^{\text{II}}$  species.

**Table 5.5:** Experimental and computed  $g_{||}$  and  $A_{||}$  (absolute values in MHz) of the principal  $\text{Cu}^{\text{II}}$  species in  $\text{O}_2$ -activated Cu-CHA samples. Uncertainties of 0.004 and 5 MHz are estimated for  $g_{||}$  and  $A_{||}$ . Computed values were obtained at the B2PLYP/CP(PPP) level of theory.

Cu-CHA samples		$g_{  }$	$A_{  }$
Experimental	A	2.352	470
	B	2.352	470
		2.325	490
	C	2.352	470
		2.290	410
Cu-CHA model		$g_{  }$	$A_{  }$
Computed	$[\text{Cu}^{\text{II}}(\text{O-6MR})_4]$	2.282	455
	$[\text{Cu}^{\text{II}}(\text{OH})(\text{O-8MR})_3]$	2.275	388

### 5.2.2 Atomistic structure of monomeric $[\text{Cu}^{\text{II}}(\text{OH})]^+$ species

To translate the spectroscopic features extracted from the analysis of the EPR and HYSCORE experiments into a microscopic structure of  $[\text{Cu}^{\text{II}}(\text{OH})]^+$  species in Cu-CHA, *ab initio* calculations at different levels of theory were performed. The 8MR windows have been proposed as privileged sites for hydroxo- $\text{Cu}^{\text{II}}$  species.<sup>25,27,236</sup> The optimized structure of the mono copper hydroxo species is shown in Figure 5.12a and displays a four-fold coordination, with three zeolite lattice oxygens from the 8MR (O-8MR) and the OH- ligand pointing towards the center of the cage. This coordination geometry  $[\text{Cu}^{\text{II}}(\text{OH})(\text{O-8MR})_3]$  is consistent with the Cu  $3d_{x^2-y^2}$  character of the SOMO (Figure 5.12b) and differs from previous assignments, based on trigonal Cu coordination.<sup>24,29,51</sup> The computed  $\text{Cu}^{\text{II}}$   $g$ - and  $A$ -tensors reported in Table 5.5 reflect the decrease of the  $g_{||}$  and  $A_{||}$  with respect to the  $[\text{Cu}^{\text{II}}(\text{O-6MR})_4]$  species. The relative orientations of  $g$ - and  $^1\text{H}$   $A$ -tensors reported in Figure 5.12c show the  $g_z \equiv g_{||}$  component perpendicular to Cu  $3d_{x^2-y^2}$  whereby the  $A_z$  component from the  $^1\text{H}$  nucleus is parallel to the 8MR plane.

The calculation of the  $^1\text{H}$  hyperfine tensor is particularly delicate as it requires the careful scrutiny of the different levels of theory reported in Table 5.6. Popular hybrid DFT methods (B3LYP,<sup>131,132</sup> PBE0<sup>237</sup> and B3PW91<sup>131,238</sup>) tend to overestimate the hyperfine couplings of the  $^1\text{H}$  nucleus of the OH- ligand and underestimate the  $g_z \equiv g_{||}$  value because of the too covalent description of the Cu-OH bond. This is clearly evident in the computed spin density over the OH group reported in Figure B.2, where the B3LYP functional predicts about 15% of spin density on the O atom of the hydroxyl group exaggerating the spin de-

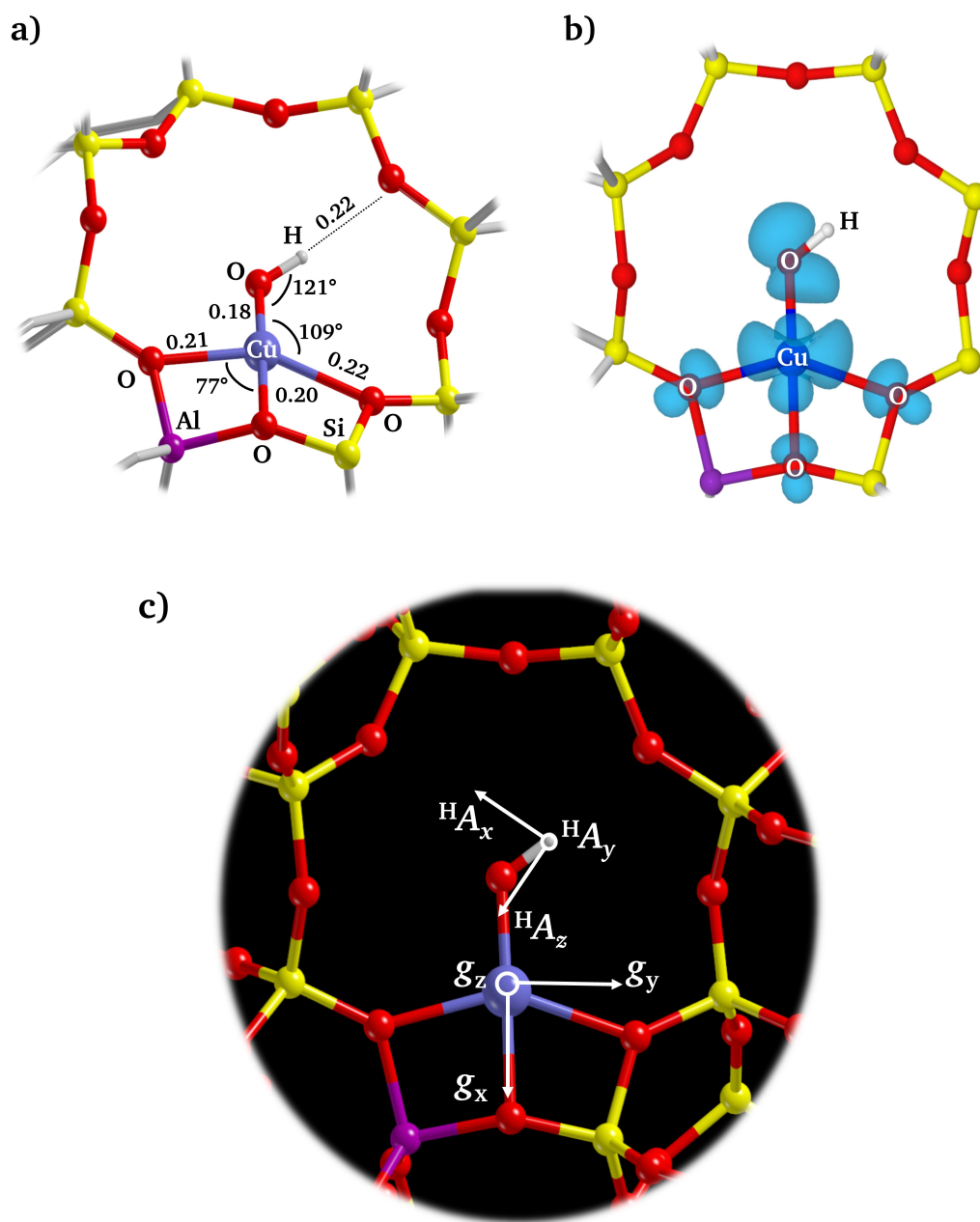


**Figure 5.12:** a) Atomistic structure of  $[\text{Cu}^{\text{II}}(\text{OH})]^+$  species in CHA. The relevant bond distances (in nm) and angles are reported. b) Spin density plot (isovalue of 0.002) of  $[\text{Cu}^{\text{II}}(\text{OH})]^+$  species in CHA. c) Computed (at B2PLYP/CP(PPP) for Cu and EPR-III for H nuclei, level of theory)  $g$ - and  $^1\text{H}$   $A$ -tensors orientations reported on the atomistic model of  $[\text{Cu}^{\text{II}}(\text{OH})(\text{O-8MR})_3]$ . This figure was adapted from Bruzzese *et al.*<sup>79</sup>

**Table 5.6:** Comparison between experimental and calculated spin Hamiltonian parameters at different level of theory on  $[\text{Cu}^{\text{II}}(\text{OH})(\text{O}-8\text{MR})_3]$  cluster model. The  $\mathbf{A}$ -tensor components are given in MHz. Euler angles  $(\alpha, \beta, \gamma)$  are given in degrees. Since the calculation of  $g$ -tensor and relative orientation of the  $\mathbf{A}$ -tensor are not yet implemented in ORCA code at DLPNO-CCSD level of theory, they are not reported here. \* $\alpha$  angle was found immaterial.

	Level of theory	$g$ -tensor				$^1\text{H}$ $\mathbf{A}$ -tensor			$\alpha, \beta, \gamma$
		$g_x$	$g_y$	$g_z$	$a_{\text{iso}}$	$T_1$	$T_2$	$T_3$	
Computed	B3LYP	2.026	2.107	2.212	-8.0	-18.4	-2.1	20.5	-135, 25, 100
	PBE0	2.027	2.124	2.238	-5.7	-16.8	-1.5	18.4	-134, 26, 97
	PBE (30% of HF exchange)	2.028	2.136	2.257	-3.9	-15.3	-1.4	16.7	-133, 26, 96
	PBE (35% of HF exchange)	2.029	2.148	2.277	-2.3	-13.8	-1.3	15.1	-131, 26, 95
	PBE (40% of HF exchange)	2.030	2.160	2.295	-0.9	-12.4	-1.4	13.8	-129, 25, 94
	PBE (45% of HF exchange)	2.031	2.168	2.313	0.1	-11.2	-1.6	12.9	-126, 25, 94
	PBE (50% of HF exchange)	2.032	2.175	2.328	0.8	-10.4	-1.8	12.2	-123, 24, 94
	B3PW91	2.026	2.109	2.214	-8.0	-18.5	-1.9	20.4	-134, 25, 99
	M06	2.026	2.286	2.861	-16.6	-19.3	-2.7	21.9	58, 54, -48
	M06-2X	2.065	2.437	3.026	1.8	-9.8	-2.1	11.9	-59, 31, 86
	B2PLYP	2.029	2.135	2.275	-3.0	-15.3	-1.6	16.9	-123, 25, 95
	DSD-BLYP	2.035	2.185	2.416	0.82	-11.3	-1.6	13.0	-127, 25, 94
	DSD-PBEP86	2.035	2.181	2.399	0.58	-11.3	-1.6	12.9	-127, 25, 94
	DLPNO-CCSD	\	\	\	-1.1	-12.1	-1.2	13.4	\
	Experimental	2.072	2.072	2.290	-2.0	-11.0	-2.5	13.5	*, 14, 93

localization towards the OH group. Highly parametrized functionals (M06 and M06-2X)<sup>239</sup> produce the worst result with a too high  $g_z$  component (M06-2X) and an overestimation of the  $^1\text{H}$  hyperfine interaction (M06). The DSD double-hybrid functionals<sup>240</sup> tested here give very similar results, not so far from the “gold standard” DLPNO-CCSD approach<sup>143</sup> and the simulated values. Concerning the  $^1\text{H}$  hfi, the DLPNO-CCSD method provides an excellent agreement with the experimental values, consistent with a more precise prediction of the spin density on the O atom of the hydroxyl group ( $\approx 7\%$ , see Figure B.2). However, increasing the HF exchange in the common PBE functional improves the results providing smaller dipolar couplings and  $|a_{\text{iso}}|$  term for the  $^1\text{H}$  nucleus. Simultaneously,  $g_z$  value increases due to the reduction of the self-interacting error.<sup>241</sup> The most performing hybrid DFT method for this specific case is PBE with 40% of HF exchange.

While the computed  $^1\text{H}$  hfis for the four-coordinated  $[\text{Cu}^{\text{II}}(\text{OH})]^+$  structure presented in Figure 5.12 nicely agree with the experimental values, the three-coordinated model shown in Figure B.3b provides values inconsistent with the experimental findings. In this case, the  $^1\text{H}$  couplings differ by 1 order of magnitude from the experimental values validating the four-coordinated model (see also Table B.2). This structure corresponds to an energy minimum, coherent with spectroscopic data collected in the temperature interval 10 K-RT. It is important to note that spectroscopic data collected at high temperature

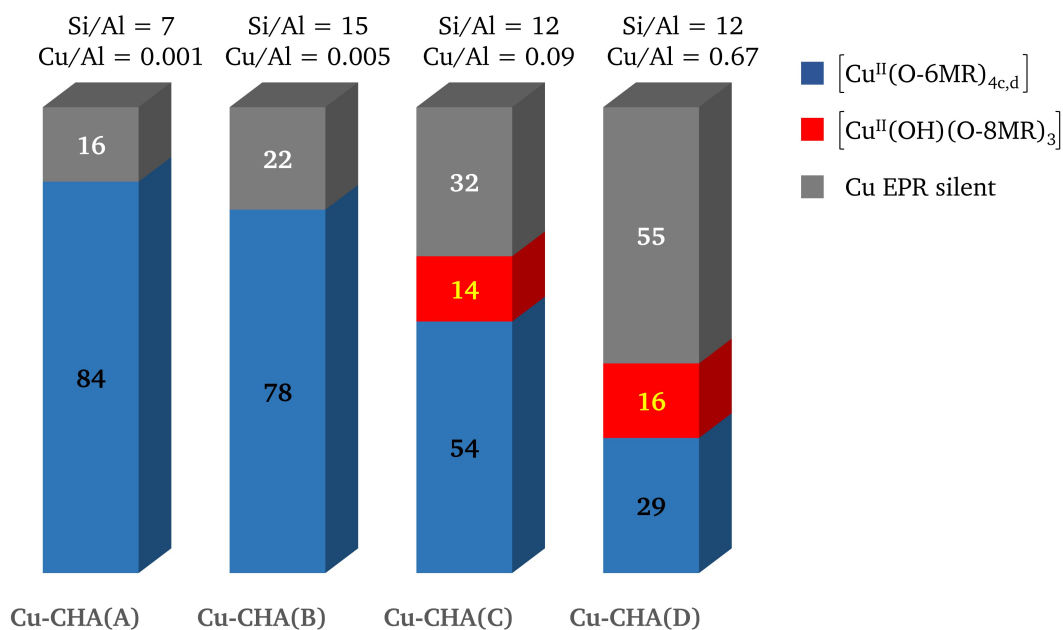


**Figure 5.13:** Column graph representing the percentage of Cu species quantified by CW-EPR with respect to the total amount of Cu determined by ICP-AES. The percentage of each species are reported inside the column according to the color code given by the legend. This figure was first published in Bruzzese *et al.*<sup>79</sup>

(673 K)<sup>24,25</sup> may not be capable of distinguishing between the four- and three-coordination geometry due to fluctuations in Cu coordination at this temperature. As an independent validation, the OH stretching and bending frequencies for the structure presented in Figure 5.12 have been calculated, providing values (3658 and 928 cm<sup>-1</sup>, respectively) in agreement with experimental results.<sup>24,227</sup> Noteworthy, computed IR frequencies for the four-coordinated and the three-coordinated models are not sufficiently different to safely distinguish between the two geometries (see Table B.2), while the <sup>1</sup>H hfis prove to be a far more sensitive structural probe allowing to discriminate between the two structures.

### 5.2.3 Quantitative assessment of isolated Cu<sup>II</sup> species in activated Cu-CHA

The total Cu amount in the four samples determined by ICP-AES has been compared with the amount of the two paramagnetic Cu<sup>II</sup> species identified in this work, namely [Cu<sup>II</sup>(O-6MR)<sub>4</sub>] (species C and D from Table 5.1) and [Cu<sup>II</sup>(OH)(O-8MR)<sub>3</sub>]. Based on the difference between the amount of paramagnetic Cu<sup>II</sup> measured by CW-EPR and the amount of Cu determined by ICP-AES, the percentage of EPR silent Cu is also recovered. Inspection of Figure 5.13

shows that the amount of paramagnetic  $\text{Cu}^{\text{II}}$  decreases as a function of increasing Cu content and Si/Al ratio. While in Cu-CHA(A) 84% of total Cu is EPR active after  $\text{O}_2$ -dehydration, in Cu-CHA(C) this fraction lowers to 68%. This EPR active  $\text{Cu}^{\text{II}}$  is composed by 54% of  $[\text{Cu}^{\text{II}}(\text{O}-6\text{MR})_4]$  at 2Al sites and 14% of  $[\text{Cu}^{\text{II}}(\text{OH})(\text{O}-8\text{MR})_3]$  at 1Al sites. These correspond to the isolated  $[\text{Cu}^{\text{II}}(\text{OH})]^+$  species that survived in their oxidized state and did not undergo condensation to form antiferromagnetically coupled dimers. This amount is consistent with literature data where the amount of  $[\text{Cu}^{\text{II}}(\text{OH})]^+$  species was determined by XANES spectroscopy<sup>226</sup> or by chemical titration<sup>5</sup> and with the theoretical value expected from the compositional phase diagram reported by Paolucci.<sup>26</sup>

Cu-CHA(D) displays the largest amount of EPR silent species after the dehydration treatment (55%), while the number of framework bound  $[\text{Cu}^{\text{II}}(\text{OH})(\text{O}-8\text{MR})_3]$  species at 1 Al sites increases up to 16%. These values concur with estimates obtained by XANES spectroscopy on a Cu-CHA sample with Si/Al=15 and Cu/Al=0.5 activated under He for which  $[\text{Cu}^{\text{II}}(\text{OH})]^+$  was found to be 13% and  $\text{Cu}^{\text{I}}=79\%$ .<sup>226</sup> In this case reduction or condensation of  $[\text{Cu}^{\text{II}}(\text{OH})]^+$  species during the outgassing treatment (1 h under high vacuum at 773 K) and the formation of EPR silent species is clearly dominant. Assuming that the EPR silent species are originated from  $[\text{Cu}^{\text{II}}(\text{OH})]^+$ , their overall amount (71%) is in the range predicted by the compositional phase diagram of Paolucci and consistent with estimates present in the literature reported in Table B.1.

The mechanisms leading to reduction of  $\text{Cu}^{\text{II}}$  and consecutive loss of EPR signal in Cu-loaded zeolites as a function of dehydration might be summarized as follows:

- One of the most common but poorly understood process is the so-called “autoreduction” or “self-reduction”, which takes place during the activation of copper-exchanged zeolites. It implies the transformation of some of the  $\text{Cu}^{\text{II}}$  species to  $\text{Cu}^{\text{I}}$  at elevated temperature, typically above 673 K, in an inert environment and in the absence of a reducing agent. The generally accepted pathway involves the elimination of water from two neighboring  $[\text{Cu}^{\text{II}}(\text{OH})]^+$  species leading to  $[\text{Cu}-\text{O}-\text{Cu}]^{2+}$  species. These species feature two antiferromagnetically coupled copper ions and are EPR silent. At high temperature ( $\geq 673$  K) these copper-oxo bridged species decompose to  $\text{Cu}^{\text{I}}$  and molecular oxygen, which desorbs from the material. The EPR signal loss in general (and in the case of this work in particular) can therefore be associated to the first step (i.e. the  $[\text{Cu}^{\text{II}}(\text{OH})]^+$  condensation).
- A second possible reason for the loss of  $\text{Cu}^{\text{II}}$  EPR intensity is copper reduction by reaction with residual carbonaceous impurities, which can remain in the catalyst after synthesis. In this case conversion of EPR active  $\text{Cu}^{\text{II}}$  to

EPR silent  $\text{Cu}^{\text{I}}$  occurs quantitatively at low temperature during the thermal activation with release of  $\text{CO}_2$ .<sup>242</sup>

- $\text{Cu}^{\text{II}}$  reduction involving the formation of  $\text{Cu-O}^\cdot$  radical species has been suggested in literature, but never experimentally confirmed.<sup>243</sup>
- A final reason for the loss of  $\text{Cu}^{\text{II}}$  EPR active species that has been proposed in literature<sup>51</sup> is linked to the formation of three-coordinated Cu species characterized by very fast relaxation rates as a consequence of a pseudo Jahn-Teller effect. However, this effect has never been directly observed and the detection of  $[\text{Cu}^{\text{II}}(\text{OH})]^+$  here reported rules out this hypothesis, leaving the first three (in particular the first two) mechanisms as the origin of loss of EPR signal upon dehydration of Cu-exchanged zeolites.

#### 5.2.4 Summary

In conclusion, this section provides a quantitative assessment of the electronic and geometric structure of monomeric hydroxo- $\text{Cu}^{\text{II}}$  species in Cu-CHA, which can be described in terms of four-fold-coordinated  $[\text{Cu}^{\text{II}}(\text{OH})(\text{O-8MR})_3]$  complexes at 8MR cages. By combining HYSCORE experiments with advanced modeling, the EPR signature of such species is univocally identified. This allows to characterize their abundance with respect to monomeric  $\text{Cu}^{\text{II}}$  or the total Cu loading by merely using the widely available CW-EPR equipment.



# Conclusions

In this PhD thesis EPR methodologies in conjunction with quantum chemical modelling were adopted to determine the microscopic structure of monomeric Cu<sup>II</sup> species in CHA systems as a function of the hydration conditions and sample composition. Specific synthetic protocols, activation procedures and isotopic enrichment were employed to tackle the complexity of the problem.

By isotopic labelling of the zeolite framework with <sup>17</sup>O and employing EN-DOR spectroscopy, the <sup>17</sup>O resonance from oxygen atoms directly bound to Cu<sup>II</sup> species were detected for the first time in a low copper-loaded zeolite with CHA topology. The measured <sup>17</sup>O hyperfine couplings provided exquisite details on the nature of the Cu interaction with the oxygen donor atoms of the zeolite framework and of solvating water molecules. This, in conjunction with *ab initio* modelling, enabled the identification of specific binding sites which are selectively populated as a function of the hydration conditions. In particular, the atomistic structure of two Cu<sup>II</sup> complexes were identified under hydrating conditions, i.e. [Cu<sup>II</sup>(H<sub>2</sub>O)<sub>6</sub>]@CHA (Figure 5.7a) and an interfacial [Cu<sup>II</sup>(H<sub>2</sub>O)<sub>4</sub>(O-8MR)<sub>2</sub>] complex (Figure 5.7b). The hexaaquacopper species coexists along with the complex [Cu<sup>II</sup>(H<sub>2</sub>O)<sub>4</sub>(O-8MR)<sub>2</sub>], where two water ligands are substituted by two oxygen donor atoms belonging to the 8MR site. The hydration/dehydration processes in Cu-CHA can be described in terms of a dynamic conversion between water solvated species and an interfacial complex [Cu<sup>II</sup>(O-6MR)<sub>4</sub>], whereby the 6MR cage behaves as a tetradentate ligand (Figure 5.6c). The [Cu<sup>II</sup>(O-6MR)<sub>4</sub>] interfacial complexes feature a SOMO with predominant metal 3d<sub>x<sup>2</sup>-y<sup>2</sup></sub> character and a covalent contribution of about 30% from the coordinating framework oxygen donor atoms. Theoretical calculations demonstrated that <sup>17</sup>O hyperfine couplings are significantly dependent upon the Al distribution in the in the 6MR site, allowing to discriminate between different Al locations and determine the most likely one for the Si/Al and Cu/Al ratios considered (Figure 5.5).

The <sup>1</sup>H hyperfine couplings associated to the hydroxo ligand bound to monomeric Cu<sup>II</sup> species in O<sub>2</sub>-activated CHA zeolites were identified using <sup>1</sup>H HYSCORE spectroscopy. This permitted to univocally assign the EPR signature of such species (long considered as EPR silent<sup>29,51-53</sup>) and determine their abundance with respect to isolated Cu<sup>II</sup> or the total amount of Cu, by using widely available

CW-EPR equipment. In agreement with previous theoretical<sup>26</sup> and experimental studies,<sup>234</sup> the detection of the EPR signal of  $[\text{Cu}^{\text{II}}(\text{OH})]^+$  species occurs at higher Si/Al and Cu/Al ratios with respect to the case of  $[\text{Cu}^{\text{II}}(\text{O-6MR})_4]$  interfacial complex. The experimental  $^1\text{H}$  hyperfine couplings were exploited to model the microscopic structure of  $[\text{Cu}^{\text{II}}(\text{OH})]^+$  species, which can be described in terms of four-fold-coordinated  $[\text{Cu}^{\text{II}}(\text{OH})(\text{O-8MR})_3]$  complexes at 8MR cages. Cutting-edge calculations of the  $^1\text{H}$  hfi allowed to distinguish between four-coordinated  $[\text{Cu}^{\text{II}}(\text{OH})(\text{O-8MR})_3]$  and three-coordinated  $[\text{Cu}^{\text{II}}(\text{OH})(\text{O-8MR})_2]$  structure, the latter ascribed to a trigonal planar coordination in previous studies.<sup>24,25,29,51,197,211,226</sup> In particular, computed  $^1\text{H}$  hyperfine couplings values for the trigonal  $[\text{Cu}^{\text{II}}(\text{OH})(\text{O-8MR})_2]$  model deviate by 1 order of magnitude from the experimental values, validating the four-coordinated model presented in Figure 5.12.

The presented results highlight the potentials of the interplay between high-resolution hyperfine spectroscopy and quantum chemical calculations in characterizing Cu species in zeolites. The exquisite sensitivity of the superhyperfine interactions is such that they account even for minute structural differences (i.e. Al distribution in the second coordination sphere of  $\text{Cu}^{\text{II}}$  ions, discrimination between three- or four-coordinated hydroxo- $\text{Cu}^{\text{II}}$  complexes). The reproduction of these spectroscopic features with sophisticated electronic structure methods translates the experimental findings into microscopic structures providing new structural data to enable structure-function correlation in Cu-loaded zeolites. Most importantly, this methodology establishes EPR with its pulsed variants and the quantum chemical modelling of EPR parameters as a unique and complementary tool for characterizing the siting of paramagnetic metal ions in zeolites with atomic-scale precision.

# Appendix A

**Table A.1:** B2PLYP-D3 computed  $g$  and Cu hyperfine principal components for hydrated cluster models of Cu-CHA compared with experimental values taken from Table 5.1. Reported hyperfine parameters are expressed in MHz. For the sake of clarity, the absolute values of the computed hyperfine components are given.

Models		$g_{xx}$	$g_{yy}$	$g_{zz}$	$A_{xx}$	$A_{yy}$	$A_{zz}$
[Cu <sup>II</sup> (H <sub>2</sub> O) <sub>6</sub> @CHA]	Experimental	2.070	2.070	2.415	30	30	400
	Computed	2.116	2.131	2.391	188	195	396
[Cu <sup>II</sup> (H <sub>2</sub> O) <sub>4</sub> (O-8MR) <sub>2</sub> ]	Experimental	2.065	2.065	2.370	30	30	450
	Computed	2.072	2.116	2.327	93	189	415

**Table A.2:** B2PLYP-D3 computed  $g$  and Cu hyperfine principal components for [Cu<sup>II</sup>(O-6MR)<sub>4</sub>] cluster models at 2Al-3NN, 2Al-2NN and 1Al sites compared with signal C taken from Table 5.1. Signal D was not reported since it represents only the 15% of the total simulated EPR signal. Reported hyperfine parameters are expressed in MHz. For the sake of clarity, the absolute values of the computed hyperfine components are given.

Models	$g_{xx}$	$g_{yy}$	$g_{zz}$	$A_{xx}$	$A_{yy}$	$A_{zz}$
2Al-3NN	2.070	2.076	2.282	42	62	455
2Al-2NN	2.060	2.082	2.278	38	83	433
1Al	2.068	2.074	2.275	32	35	469
Experimental	2.058	2.058	2.355	30	30	462

**Table A.3:** Bond distances of Cu-H obtained from  $[\text{Cu}^{\text{II}}(\text{H}_2\text{O})_6@\text{CHA}]$  and  $[\text{Cu}^{\text{II}}(\text{H}_2\text{O})_4(\text{O}-8\text{MR})_2]$  periodic models after fully optimization at B3LYP-D3/pob-TZVP level of theory. Equatorial (*eq*) and axial (*ax*) protons are listed distinctly. The distances are given in nm.

Models	$d(\text{Cu}-\text{H}_{eq})$	$d(\text{Cu}-\text{H}_{ax})$
$[\text{Cu}^{\text{II}}(\text{H}_2\text{O})_6@\text{CHA}]$	0.27	0.30
	0.28	0.28
	0.25	0.30
	0.25	0.28
	0.26	
	0.26	
	0.29	
	0.26	
$[\text{Cu}^{\text{II}}(\text{H}_2\text{O})_4(\text{O}-8\text{MR})_2]$	0.25	0.30
	0.26	0.29
	0.26	
	0.26	
	0.25	
	0.26	

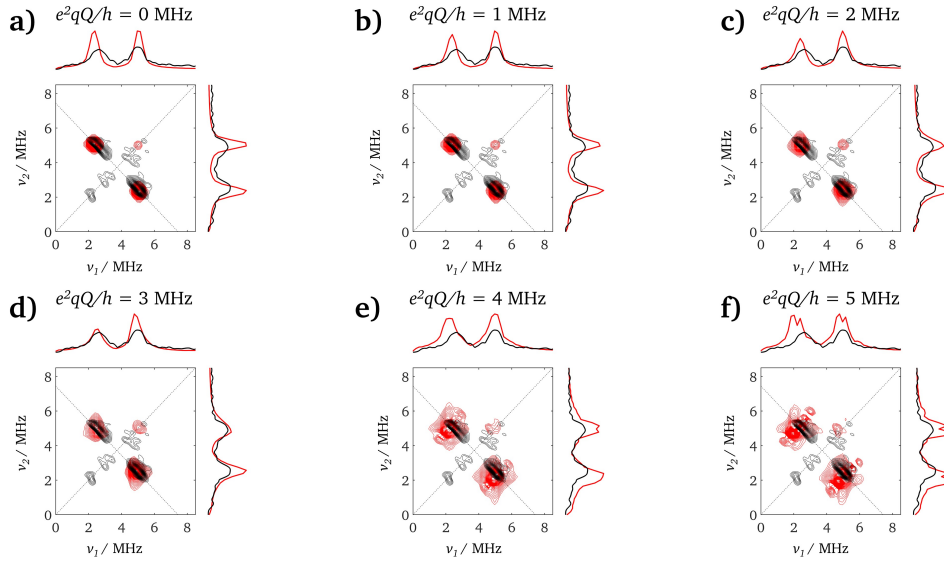


**Figure A.1:** Evaluation of the effect of the nuclear quadrupole interaction in X-band  $^{27}\text{Al}$  HYSCORE experiments (in black) in the hydrated Cu-CHA(B) sample. A  $e^2qQ/h$  value of a) 0 MHz, b) 1 MHz, c) 2 MHz, d) 3 MHz, e) 4 MHz, f) 5 MHz was used with  $[\alpha', \beta', \gamma']$  angles equal to  $[0, 20, 0]$  degrees. In the simulations (in red) the  $^{27}\text{Al}$   $\mathbf{A}$ -tensor and its relative orientation with respect to g-tensor employed are the same as reported in Table 5.2. This figure was first published in Bruzzese *et al.*<sup>78</sup>

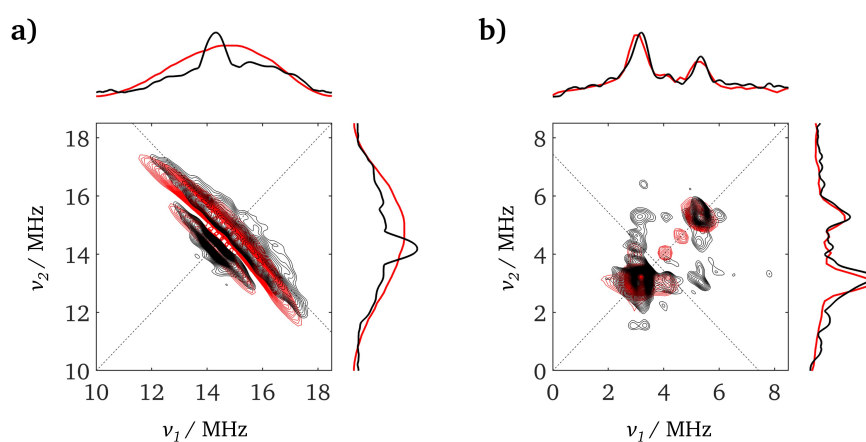


**Figure A.2:** a) Simulation (in red) of the  $^1\text{H}$  HYSCORE spectrum (in black) of the fully hydrated Cu-CHA(B) sample. b) Simulation (in red) of the  $^{27}\text{Al}$  HYSCORE spectrum (in black) of the fully dehydrated Cu-CHA(B) sample. Due to the fact that it was impossible to record  $^{27}\text{Al}$  HYSCORE spectrum at the  $g_{\parallel}$  position because of the low S/N ratio, it is not possible to obtain a univocal set of parameters. A representative simulation obtained using the spin Hamiltonian parameters reported in Table 5.2 is shown which qualitatively reproduces the experimental features. The parameters are consistent with data reported for other Cu-doped zeolites<sup>44,46</sup> and with the computed values. This figure was first published in Bruzzese *et al.*<sup>78</sup>

**Table A.4:** Periodic computed spin Hamiltonian parameters of  $^{17}\text{O}$ ,  $^{27}\text{Al}$  and  $^1\text{H}$  nuclei on (a)  $[\text{Cu}^{\text{II}}(\text{H}_2\text{O})_6@ \text{CHA}]$  and (b)  $[\text{Cu}^{\text{II}}(\text{H}_2\text{O})_4(\text{O}-8\text{MR})_2]$  atomistic models at B3LYP-D3/EPR-III(truncated) for  $^{17}\text{O}$  and  $^1\text{H}$  and aug-cc-pVTZ-J(truncated) for  $^{27}\text{Al}$  level of theory. The labelling of the atoms refers to the one indicated in Figure 5.7. Hyperfine coupling constants and quadrupole coupling constants are given in MHz. The experimental values are taken from Tables 5.2 and 5.3 for comparison. For the sake of clarity, we reported the mean values of  $a_{\text{iso}}$  and  $T$  components of the equatorial and axial protons. While the computed  $a_{\text{iso}}$  term for axial water protons is always set around 0.1-0.4 MHz, the isotropic hyperfine coupling constants of the equatorial water molecules depend on the orientation of the water molecules with respect to the equatorial plane, as previously discussed by Larsen.<sup>244</sup> Therefore a realistic comparison of the experimental and computed isotropic hfi is difficult to assess because the actual orientation of water ligands is affected by remote water molecules as well as the zeolite framework.

<sup>17</sup> O A-tensor							<sup>1</sup> H A-tensor					<sup>27</sup> Al A-tensor					
		<i>a</i> <sub>iso</sub>	<i>T</i> <sub>1</sub>	<i>T</i> <sub>2</sub>	<i>T</i> <sub>3</sub>	<i>e</i> <sup>2</sup> <i>qQ</i> / <i>h</i>		<i>a</i> <sub>iso</sub>	<i>T</i> <sub>1</sub>	<i>T</i> <sub>2</sub>	<i>T</i> <sub>3</sub>		<i>a</i> <sub>iso</sub>	<i>T</i> <sub>1</sub>	<i>T</i> <sub>2</sub>	<i>T</i> <sub>3</sub>	<i>e</i> <sup>2</sup> <i>qQ</i> / <i>h</i>
(a)	O <sub>e1</sub>	-40.1	5.1	5.5	-10.6	10.3	H <sub>eq</sub>	2.0	-2.8	-5.5	8.4						
	O <sub>e2</sub>	-55.7	11.3	11.2	-22.5	9.0	H <sub>ax</sub>	0.4	-2.5	-2.7	5.2						
	O <sub>e3</sub>	-58.7	9.0	8.9	-17.8	10.0											
	O <sub>e4</sub>	-45.4	4.9	5.1	-10.0	10.3											
	O <sub>a1</sub>	-8.3	1.8	1.8	-3.7	9.4											
	O <sub>a2</sub>	-6.9	1.7	1.6	-3.3	9.7											
(b)	O <sub>e1</sub>	-45.4	9.0	9.0	-18.0	4.9	H <sub>eq</sub>	1.05	-2.4	-7.7	10.1	Al <sub>1</sub>	-1.3	-0.9	-0.5	1.4	9.9
	O <sub>a2</sub>	0.7	0.8	0.7	-1.5	4.1	H <sub>ax</sub>	-0.2	-2.3	-2.5	4.8						
	O <sub>e3</sub>	-46.7	10.3	10.6	-20.9	9.0											
	O <sub>e4</sub>	-55.8	9.8	9.8	-19.5	9.3											
	O <sub>a1</sub>	2.6	0.5	0.6	-1.1	9.3											
	O <sub>e2</sub>	-42.5	7.9	8.1	-16.0	9.7											
Experimental	O(1)	-44.0	8.0	8.0	-16.0	3.0	H(1)	-1.5	-4.0	-6.0	10.0	Al(1)	-2.3	-1.0	-1.0	2.0	≤4
	O(2)	-10.0	2.0	2.0	-4.0	3.0	H(2)	0.3	-4.0	-3.0	7.0						

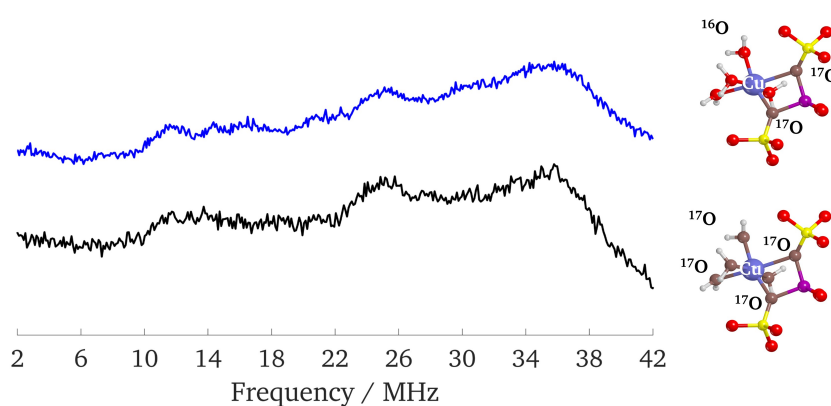


**Figure A.3:**  $^{17}\text{O}$  Davies ENDOR spectra recorded at the maximum of the echo intensity. The black spectrum refers to Cu-CHA(B) isotopically enriched sample hydrated with  $\text{H}_2^{17}\text{O}$  whereas the blue one corresponds to Cu-CHA(B) hydrated with normal water after the isotopic enrichment. The corresponding pictorial representation of the Cu site is reported on the right of each spectrum. The similarity of the two spectra demonstrates that  $\text{Cu}^{\text{II}}$  retains a direct linkage with the framework under hydrating conditions and that the water and framework oxygen equatorial ligands display a similar degree of spin density, in accord with the computed data (see  $\text{O}_{\text{e}1}$  and  $\text{O}_{\text{e}3}$  in Table A.4). 64 scans were averaged for the  $^{16}\text{O}$  solvating water against 25 scans for the  $^{17}\text{O}$  solvating water. This figure was first published in Bruzzese *et al.*<sup>78</sup>

**Table A.5:** Periodic computed spin Hamiltonian parameters of  $^{17}\text{O}$  and  $^{27}\text{Al}$  on  $[\text{Cu}^{\text{II}}(\text{O-6MR})_4]$  periodic models at 2Al-3NN, 2Al-2NN and 1Al sites at B3LYP-D3/EPR-III(truncated) for  $^{17}\text{O}$  and aug-cc-pVTZ-J(truncated) for  $^{27}\text{Al}$  level of theory. The labelling of the atoms refers to the one indicated in Figure 5.5. Hyperfine coupling constants and quadrupole coupling constants are given in MHz. The experimental values are taken from Tables 5.2 and 5.3.

$^{17}\text{O}$ A-tensor							$^{27}\text{Al}$ A-tensor					
		$a_{\text{iso}}$	$T_1$	$T_2$	$T_3$	$e^2qQ/h$		$a_{\text{iso}}$	$T_1$	$T_2$	$T_3$	$e^2qQ/h$
2Al-3NN	O <sub>1</sub>	-37.5	16.5	16.4	-32.9	4.1	Al <sub>1</sub>	-5.6	0.2	1.3	-1.4	12.3
	O <sub>2</sub>	-45.4	8.9	9.0	-18.0	5.2	Al <sub>2</sub>	0.5	-0.3	-0.7	1.0	13.1
	O <sub>3</sub>	-49.8	11.8	11.8	-23.6	4.6						
	O <sub>4</sub>	-36.0	8.6	8.6	-17.2	5.1						
2Al-2NN	O <sub>1</sub>	-39.9	20.5	20.3	-40.8	4.1	Al <sub>1</sub>	0.9	-0.5	-0.9	1.3	12.7
	O <sub>2</sub>	-43.0	12.2	12.1	-24.2	4.6	Al <sub>2</sub>	-6.0	0.2	1.2	-1.4	11.7
	O <sub>3</sub>	-41.1	9.3	9.4	-18.7	4.5						
	O <sub>4</sub>	-37.2	6.7	6.7	-13.4	3.7						
1Al	O <sub>1</sub>	-42.1	19.8	19.6	-39.5	4.3	Al	-6.6	0.2	1.3	-1.4	16.3
	O <sub>2</sub>	-42.8	8.7	8.7	-17.4	5.3						
	O <sub>3</sub>	-49.6	12.9	12.9	-25.9	4.8						
	O <sub>4</sub>	-32.5	6.3	6.4	-12.7	3.7						
Experimental	O(3)	-51.0	12.0	12.0	-24.0	4.0	Al(2)	-3.0	2.0	2.0	-4.0	11.0
	O(4)	-41.0	9.5	9.5	-19.0	4.0						

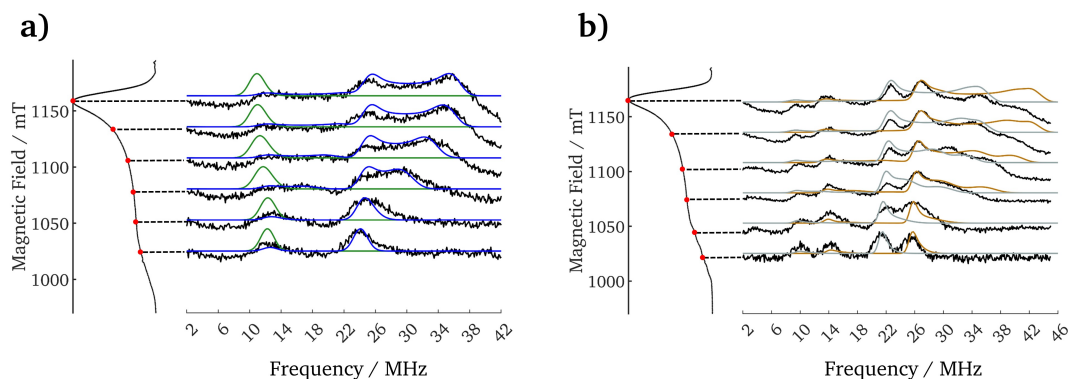


**Figure A.4:** Q-band  $^{17}\text{O}$  ENDOR spectra simulation highlighting the contribution of each  $^{17}\text{O}$  species. The black lines are the experimental spectra. The ESE spectrum with the corresponding field position sampled are plotted on the left. a) Fully hydrated with  $\text{H}_2^{17}\text{O}$ . The blue lines represent the simulation obtained with the spin Hamiltonian of  $^{17}\text{O}(1)$ , the green ones of  $^{17}\text{O}(2)$ . b) Dehydrated after  $^{17}\text{O}$  enrichment. The brown lines represent the simulation obtained with the spin Hamiltonian of  $^{17}\text{O}(3)$ , the gray ones of  $^{17}\text{O}(4)$ . This figure was first published in Bruzzese *et al.*<sup>78</sup>



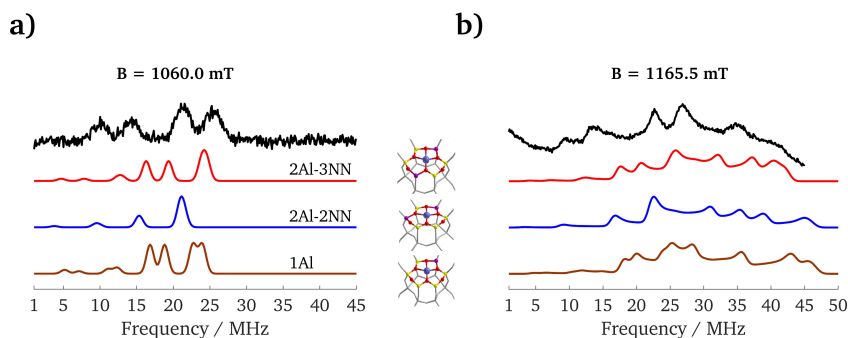


**Figure A.5:** Comparison of experimental (black) and simulated Q-band  $^{17}\text{O}$  ENDOR spectra of the  $^{17}\text{O}$  enriched dehydrated sample measured at a) parallel and b) perpendicular field. The simulated spectra were obtained by using the computed  $^{17}\text{O}$  hyperfine coupling tensors for the three different Al distributions considered in the main text (1Al in brown, 2Al-2NN in blue and 2Al-3NN in red). All four coordinating oxygen donor atoms were considered. We remark that the data refer to geometrically optimized structures at 0 K, while averaged parameters are determined in the experiment. This figure was first published in Bruzzese *et al.*<sup>78</sup>

## Calculation of spin density from the $^{17}\text{O}$ hyperfine couplings

From the observation of the hyperfine structure and determination of the  $a_{iso}$  and  $T$  hyperfine couplings, the electronic spin distribution in a molecular fragment can be obtained. To do so it is important that the hfi interaction with several nuclei in the molecule are observed. Then, with the knowledge of  $a_{iso}$  and  $T$  for the atomic species, and assuming that the hfi interaction at a given nucleus is proportional to the electron spin density at that nucleus, one can obtain the spin population in  $s$ -type orbitals  $\rho_s$ ,  $p$ -type orbitals  $\rho_p$ .

For an unpaired electron (free electron,  $g_e=2.0023$ ) on a  $^{17}\text{O}$  nucleus with a unitary spin population ( $\rho_s = 1$ ) in an  $s$ -type orbital, one would observe an isotropic hyperfine coupling constant of  $a_0 = -4622.83$  MHz. If the electron resides in a  $p$ -type orbital one would observe a uniaxial hyperfine constant of  $b_0 = 130.4$  MHz. Including a correction for the difference in the  $g$  values, the spin populations in  $s$ -type and  $p$ -type orbitals can thus be estimated as:

$$\rho_s = \frac{A_{iso}}{a_0} \frac{g_e}{g_{iso}} \text{ and } \rho_p = \frac{T}{b_0} \frac{g_e}{g_{iso}} \quad (\text{A.1})$$

In the calculation of  $\rho_p$  we consider that the value used for  $T$  should be corrected

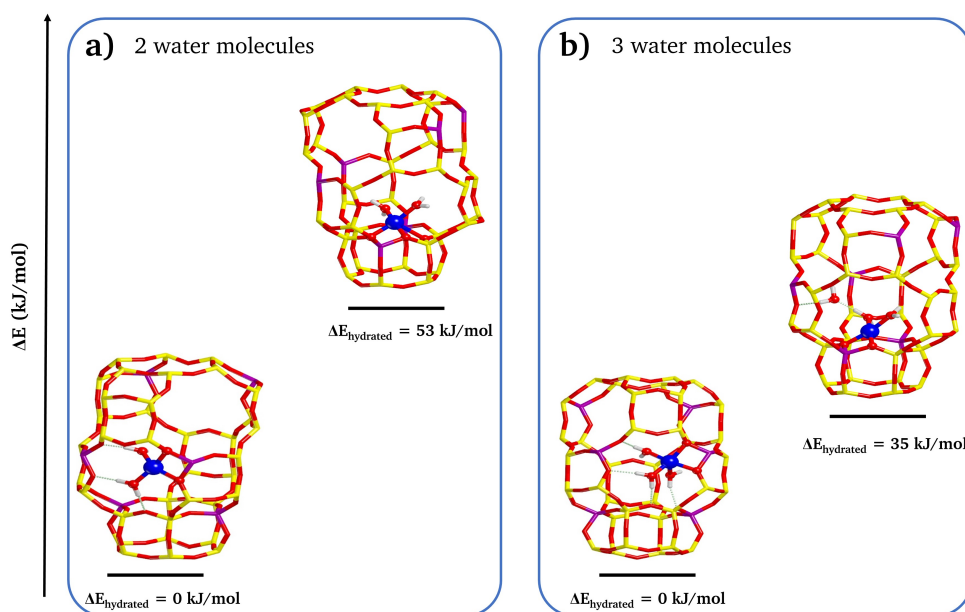


**Figure A.6:** Full optimized structures at B3LYP-D3/pob-TZVP level of theory of  $\text{Cu}^{\text{II}}$  species sitting in 6MRs and 8MRs hydrated with a) 2 water molecules and b) 3 water molecules. Cu are indicated with blue balls, Al with violet balls, O red balls, H in white balls and Si in yellow sticks. The relative stability of both the sites is evaluated in terms of relative electronic energy per unit cell. DFT computations point out that, in presence of more than one water molecules in the copper coordination sphere, 8MR sites appears to be more stable with respect to 6MR location. This difference between the two sites is likely due to the lower coordination number of  $\text{Cu}^{\text{II}}$  cations in 8MR in comparison to 6MR sites when no adsorbates are present. Moreover, the adsorption of water molecules provokes significant change in the local geometry of the copper ions (from distorted square planar to a distorted square pyramidal geometries). Note that the third water molecules in 6MR site does not interact directly with Cu but it is linked to its first coordination sphere through hydrogen bonds. The increasing of the water molecules bound to  $\text{Cu}^{\text{II}}$  leads copper ion shifted upward, above the position of 6MR unit. This figure was first published in Bruzzese *et al.*<sup>78</sup>

for the through space dipolar interaction ( $T^d$ ) between the magnetic moment of  $^{17}\text{O}$  and spin population that is located on the metal center. Using the Cu-O values obtained from the DFT calculations and assuming 70% spin density on Cu, for the hydrated case, we can estimate the contribution  $^{17}\text{O}$ -hyperfine matrix as  $T^d = \begin{bmatrix} 0.94 & 0.94 & -1.88 \end{bmatrix}$  MHz for the equatorial O ligand ( $d_{\text{Cu-O}} = 0.20$  nm) and  $T^d = \begin{bmatrix} 0.54 & 0.54 & -1.08 \end{bmatrix}$  MHz for the axial O ligands ( $d_{\text{Cu-O}} = 0.24$  nm) respectively. The corrected value to estimate  $\rho_p$  is thus given by:  $T = T_{\text{tot}} - T^d = 8.00 - 0.94 = 7.06$  MHz for the equatorial case and  $T = T_{\text{tot}} - T^d = 2.00 - 0.54 = 1.46$  MHz for the axial case, corresponding to 5.4% and 1.1% O  $p$  character for the equatorial and axial ligands, respectively. Analogous calculations in the case of the tetragonal complex of the dehydrated system lead to  $\rho_p$  equal to 8.5% and 6.6 % for the two oxygen families ( $^{17}\text{O}(3)$  and  $^{17}\text{O}(3)$  in Table 5.3). The total spin density on the oxygen ligands obtained as the sum of the two  $\rho_s$  and  $\rho_p$  contributions nicely agrees with the Mulliken spin population reported in Tables A.6 and A.7.

**Table A.6:** Mulliken spin population analysis and Cu-O bond distances calculated at B3LYP-D3/EPR-III(truncated) level of theory for  $[\text{Cu}^{\text{II}}(\text{H}_2\text{O})_6@ \text{CHA}]$  and  $[\text{Cu}^{\text{II}}(\text{H}_2\text{O})_4(\text{O}-8\text{MR})_2]$  periodic models illustrated in Figure 5.7. The labelling of the oxygen atoms refers to the one indicated in Figure 5.7. Cu-O bond distances are given in nm.

Models	Nuclei	$d(\text{Cu-O})$	$\rho_{\text{spin}}$	$2s$	$2p_x$	$2p_y$	$2p_z$
$[\text{Cu}^{\text{II}}(\text{H}_2\text{O})_6@ \text{CHA}]$	$\text{O}_{e1}$	0.210	0.022	0.008	0.010	0.008	0.006
	$\text{O}_{e2}$	0.193	0.056	0.012	0.013	0.009	0.027
	$\text{O}_{e3}$	0.194	0.042	0.010	0.012	0.015	0.010
	$\text{O}_{e4}$	0.209	0.020	0.008	0.016	0.003	0.002
	$\text{O}_{a1}$	0.224	0.004	0.002	0.001	0.002	0.003
	$\text{O}_{a2}$	0.227	0.004	0.001	0.000	0.000	0.004
$[\text{Cu}^{\text{II}}(\text{H}_2\text{O})_4(\text{O}-8\text{MR})_2]$	$\text{O}_{e1}$	0.199	0.046	0.011	0.006	0.032	0.006
	$\text{O}_{e2}$	0.206	0.037	0.009	0.001	0.027	0.007
	$\text{O}_{e3}$	0.199	0.044	0.009	0.024	0.006	0.013
	$\text{O}_{e4}$	0.196	0.051	0.011	0.004	0.021	0.022
	$\text{O}_{a1}$	0.234	0.001	0.000	0.000	0.000	0.000
	$\text{O}_{a2}$	0.241	0.001	0.000	0.000	0.000	0.000

**Table A.7:** Mulliken spin population analysis and Cu-O bond distances calculated at B3LYP-D3(ABC)/EPR-III(truncated) level of theory for  $[\text{Cu}^{\text{II}}(\text{O}-6\text{MR})_4]$  periodic models at 2Al-3NN, 2Al-2NN and 1Al sites. The labelling of the oxygen atoms refers to the one indicated in Figure 5.5. Cu-O bond distances are given in nm.

Models	Nuclei	$d(\text{Cu-O})$	$\rho_{spin}$	$2s$	$2p_x$	$2p_y$	$2p_z$
2Al-3NN	O <sub>1</sub>	0.202	0.084	0.010	0.018	0.062	0.0006
	O <sub>2</sub>	0.202	0.041	0.008	0.014	0.029	0.000
	O <sub>3</sub>	0.195	0.059	0.010	0.055	0.000	0.000
	O <sub>4</sub>	0.196	0.044	0.007	0.014	0.025	0.000
2Al-2NN	O <sub>1</sub>	0.205	0.104	0.013	0.025	0.076	0.000
	O <sub>2</sub>	0.194	0.062	0.009	0.024	0.034	0.000
	O <sub>3</sub>	0.195	0.045	0.007	0.041	0.000	0.000
	O <sub>4</sub>	0.205	0.030	0.007	0.007	0.022	0.000
1Al	O <sub>1</sub>	0.199	0.102	0.012	0.023	0.075	0.000
	O <sub>2</sub>	0.203	0.039	0.008	0.014	0.026	0.000
	O <sub>3</sub>	0.193	0.067	0.008	0.061	0.000	0.000
	O <sub>4</sub>	0.204	0.029	0.006	0.008	0.017	0.000

## Appendix B

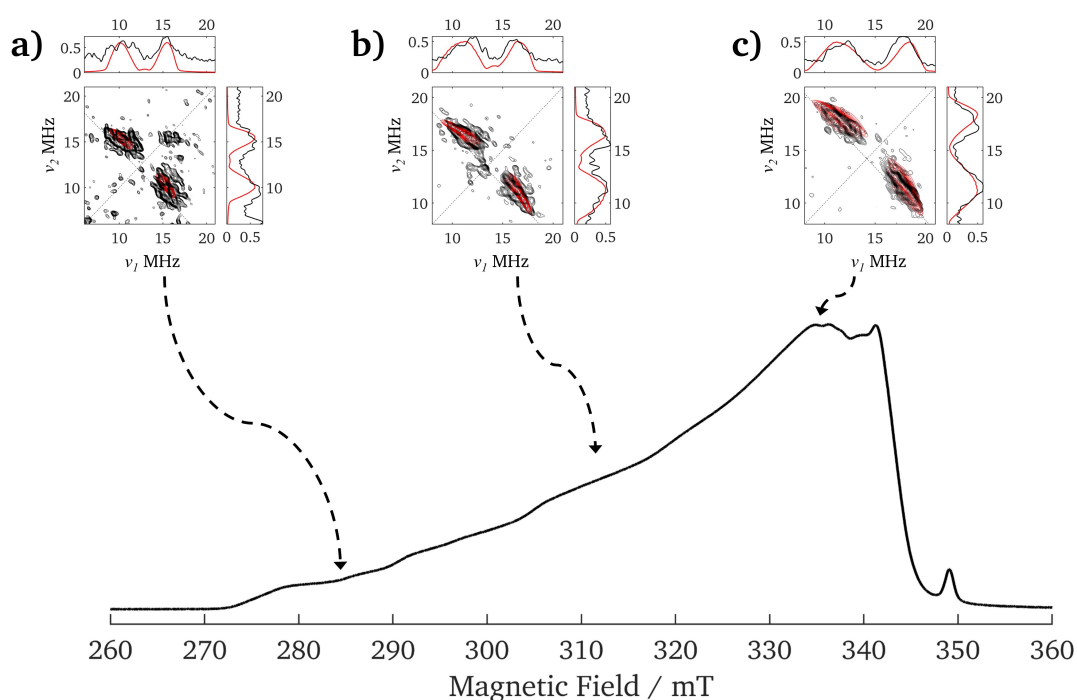


**Figure B.1:** Experimental (in black) and computer simulations (in red) of X-band  $^1\text{H}$  HYSCORE spectra of  $\text{O}_2$ -activated Cu-CHA(C) acquired at a) 284.3 mT, b) 313.0 mT and c) 333.4 mT. The corresponding sum projections are also shown. Each HYSCORE spectrum was measured by employing a  $\tau$  value that suppresses the signal at the proton Larmor frequency at the corresponding magnetic field ( $\tau = 164$  ns in a),  $\tau = 150$  ns in b) and  $\tau = 130$  ns in c)). The computer simulations were obtained by using the spin Hamiltonian parameters given in Table 5.4 (Cu-CHA(C)) and Table 2 (simulated values). The experimental ESE spectrum is reported in black.

**Table B.1:** Speciation of Cu sites and estimation of their amount in activated Cu-CHA samples as reported in literature.

Composition	Activation procedure	Characterization technique	2Al Cu <sup>II</sup>	1Al Cu <sup>II</sup> OH	1Al Cu <sup>I</sup>	Cu <sub>x</sub> O <sub>y</sub>	Reference
Si/Al = 15 Cu/Al = 0.50	773 K in He	XANES spectroscopy	8.0%	13.0%	79.0%	\	Ref. <sup>226</sup>
Si/Al = 12.5 Cu/Al = 0.29	823 K in O <sub>2</sub> /He flow for 1 h	H <sub>2</sub> -TPR	45.0%	55.0%	\	\	Ref. <sup>234</sup>
Si/Al = 12 Cu loading = 2.1 wt %	523 K in He for 1 h	EPR (based on the intensities difference of the hydrated and dehydrated form)	37.0%	63.0%	\	\	Ref. <sup>52</sup>
Si/Al = 14 Cu/Al = unknown	523 K in O <sub>2</sub> /He flow for 2 h	EPR (based on the intensities differences of the hydrated and dehydrated form and the weights used for simulating the spectra)	25.0%	50.0%	\	25.0%	Ref. <sup>51</sup>
Si/Al = 14 Cu/Al = unknown	523 K in He flow for 14 h	EPR (based on the intensities differences of the hydrated and dehydrated form and the weights used for simulating the spectra)	25.0%	\	50.0%	25.0%	Ref. <sup>51</sup>
Si/Al = 15 Cu/Al = 0.10	773 K in O <sub>2</sub>	Titration of the residual H <sup>+</sup>	90.0%	10.0%	\	\	Ref. <sup>5</sup>
Si/Al = 12.5 Cu/Al = 0.11	873 K in O <sub>2</sub> and H <sub>2</sub> O for 5 h	N <sub>2</sub> O adsorption + TPD and H <sub>2</sub> -TPR	45.0%	55.0%	\	\	Ref. <sup>245</sup>
Si/Al = 12 Cu/Al = 0.09	523 K in O <sub>2</sub> for 2 h	EPR (direct measurement)	54.4%	13.6%	\	\	<b>This work</b>
Si/Al = 12 Cu/Al = 0.67	523 K in O <sub>2</sub> for 2 h	EPR (direct measurement)	29.2%	15.7%	\	\	<b>This work</b>

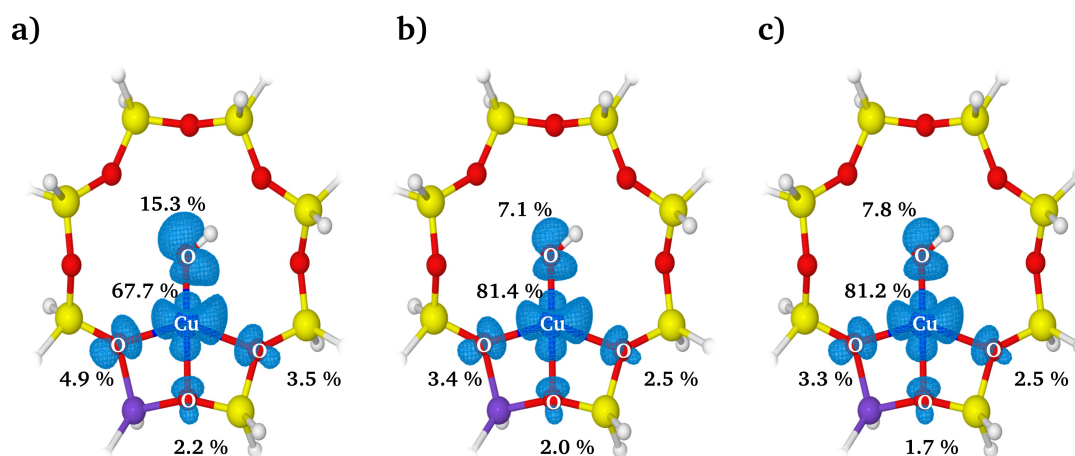


**Figure B.2:** Spin density plots of  $[\text{Cu}^{\text{II}}(\text{OH})(\text{O-8MR})_3]$  cluster model obtained at a) B3LYP, b) DSD-PBEP86 and c) DLPNO-CCSD levels of theory. Isovalue levels were fixed at 0.002. Löwdin spin populations of the relevant atoms are indicated in percentage. Si, Al and H atoms are indicated in yellow, violet and white, respectively.

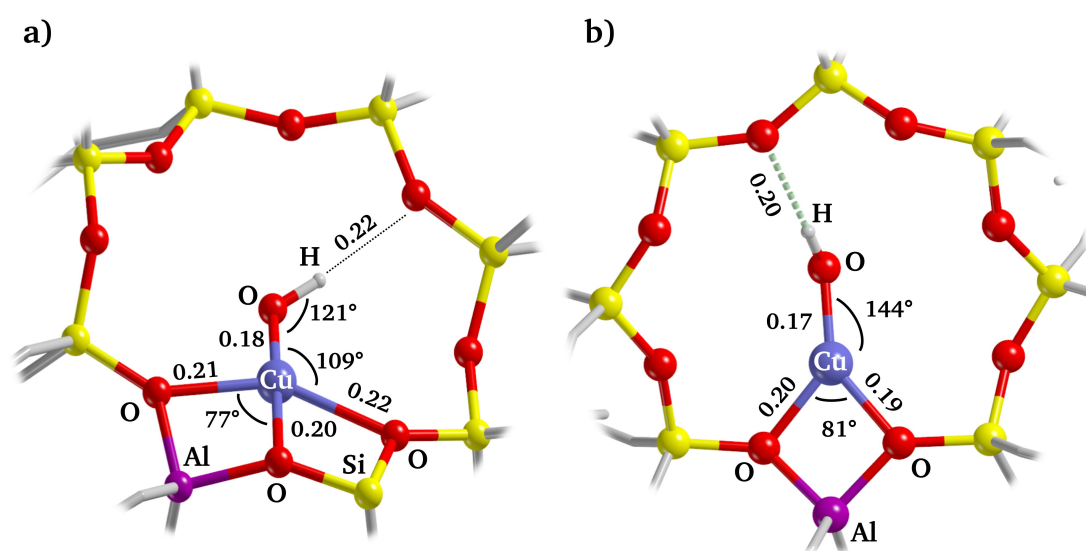


**Figure B.3:** Possible optimized structural geometries of framework bound  $[\text{Cu}^{\text{II}}(\text{OH})]^+$  species. a) four-coordinated  $[\text{Cu}^{\text{II}}(\text{OH})(\text{O-8MR})_3]$  structure; b) three-coordinated  $[\text{Cu}^{\text{II}}(\text{OH})(\text{O-8MR})_2]$  structure

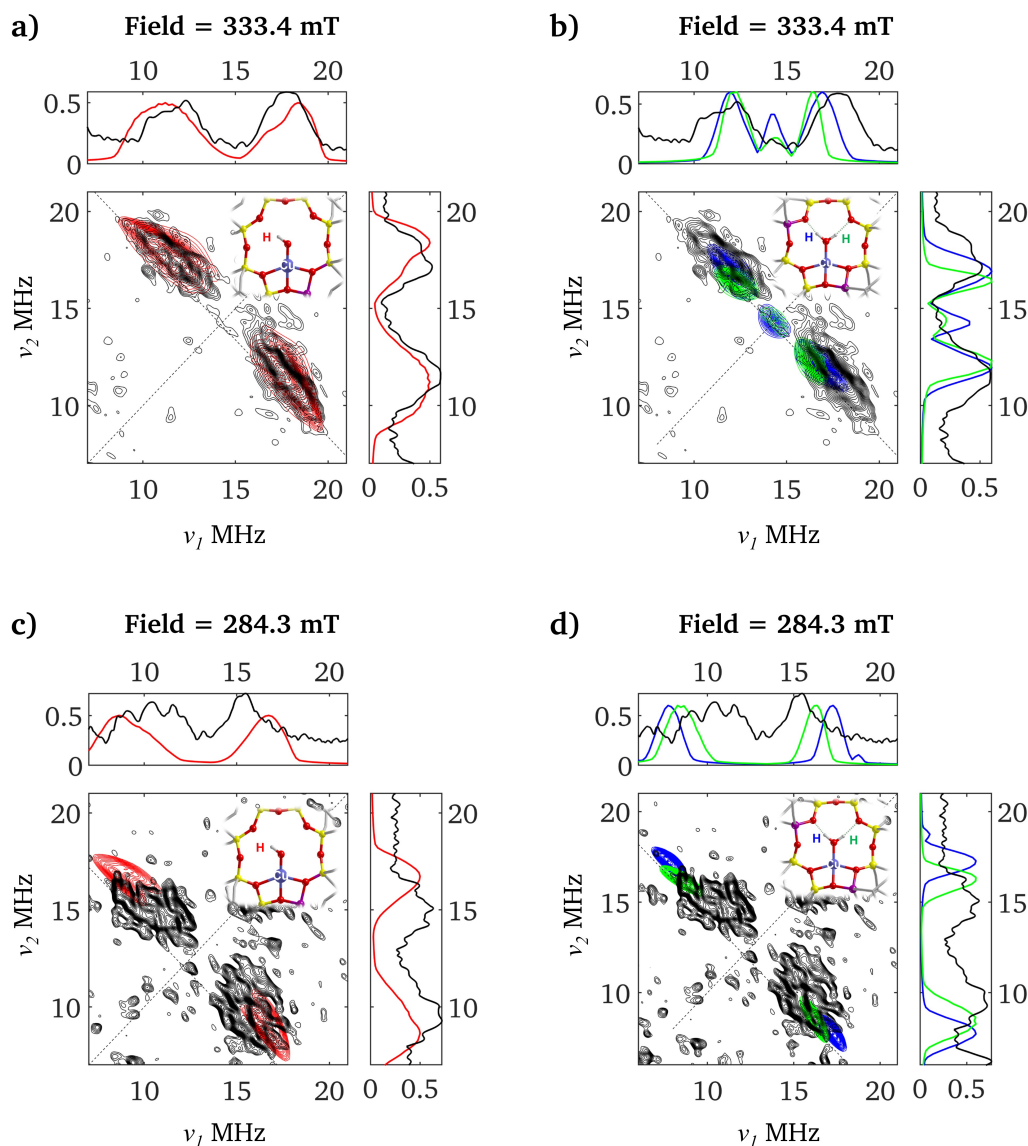


**Figure B.4:**  $^1\text{H}$  HYSCORE spectra (in black) of Cu-CHA(C) together with the computer simulation obtained at the reported magnetic fields by using computed spin Hamiltonian parameters on a) and c) cluster model of  $[\text{Cu}^{\text{II}}(\text{OH})(\text{O}-8\text{MR})_3]$ . The simulated proton signal is given in red; b) and d) cluster model of  $[\text{Cu}^{\text{II}}(\text{H}_2\text{O})(\text{O}-8\text{MRs})_3]$ . The simulated proton signals are given in green and blue. The relative sum projections are also reported. The level of theory employed for the computed values was DSD-PBEP86/EPR-III for  $\mathbf{A}$ -tensor of the H nuclei. This figure was first published in Bruzzese *et al.*<sup>79</sup>



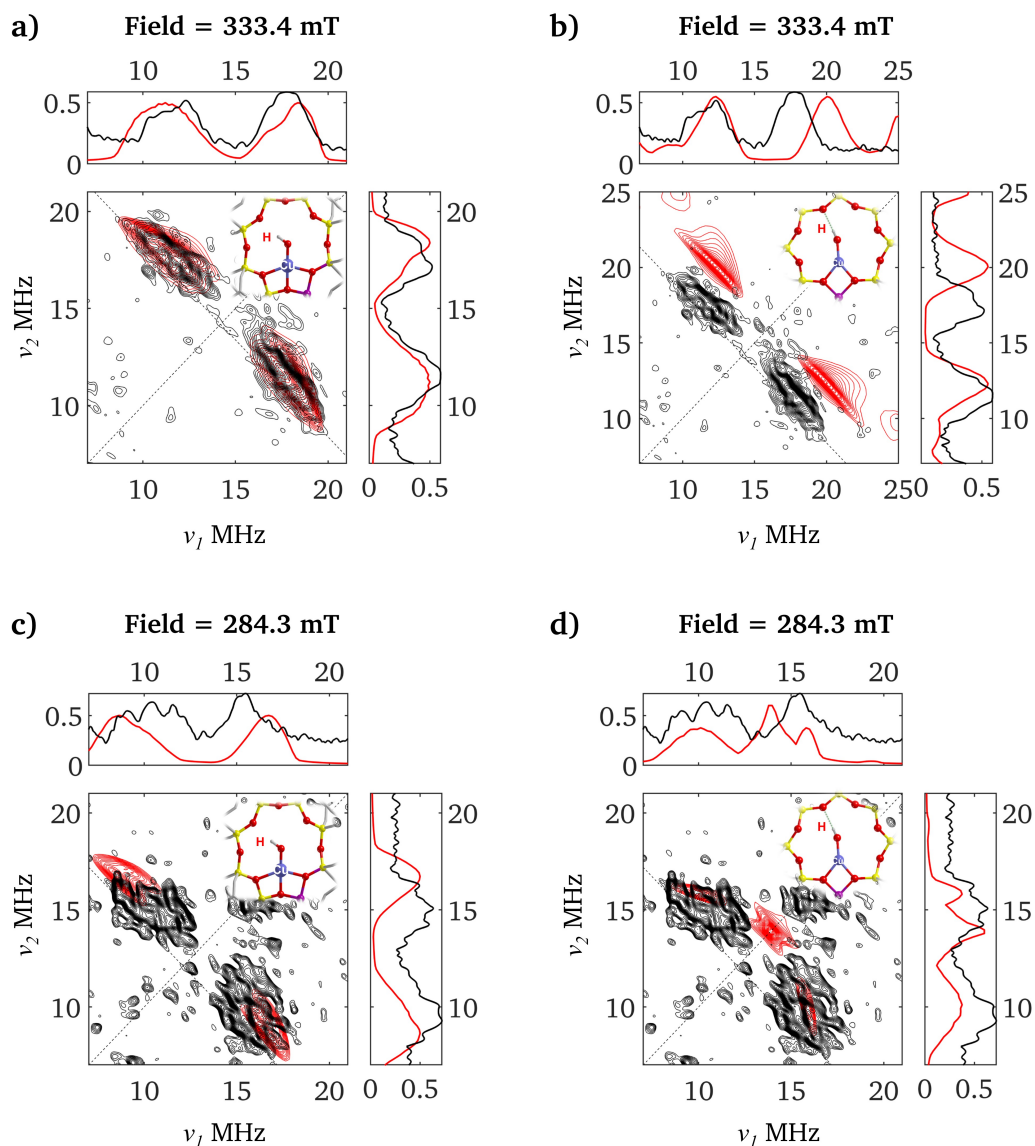


**Figure B.5:** Experimental (black) and simulated (red)  $^1\text{H}$  HSCORE spectra taken at different magnetic field setting using the computed spin Hamiltonian parameters reported in Table B.2. a), c) four-coordinated structure; b, d) three-coordinated structure. The magnetic field settings are reported in the figure and correspond to the perpendicular (a,b) and the parallel component (c,d) of the spectrum. This figure was first published in Bruzzese *et al.*<sup>79</sup>

**Table B.2:** Computed  $^1\text{H}$  hyperfine coupling constants (in MHz) and anharmonic stretching frequencies of OH group bound to Cu ( $\nu_{\text{OH}}$  in  $\text{cm}^{-1}$ ) for  $[\text{Cu}^{\text{II}}(\text{OH})(\text{O}-8\text{MR})_2]$  and  $[\text{Cu}^{\text{II}}(\text{OH})(\text{O}-8\text{MR})_3]$  structures.  $^1\text{H}$  hyperfine coupling constants were computed at DLPNO-CCSD/cc-pwCVQZ level of theory whereas the anharmonic stretching frequencies were computed at B3LYP-D3/pob-TZVP level of theory. \*The experimental value of  $\nu_{\text{OH}}$  is taken from Ref.<sup>24</sup>

		$^1\text{H}$ <i>A</i> -tensor				$\nu_{\text{OH}}$
		$a_{\text{iso}}$	$T_1$	$T_2$	$T_3$	
Computed	$[\text{Cu}^{\text{II}}(\text{OH})(\text{O}-8\text{MR})_2]$	-14.9	-16.8	-7.1	23.9	3626
	$[\text{Cu}^{\text{II}}(\text{OH})(\text{O}-8\text{MR})_3]$	-1.1	-12.1	-1.2	13.4	3658
Experimental		-2.0	-11.0	-2.5	13.5	3656*

# Bibliography

- (1) Schlögl, R. *Angew. Chem. Int. Ed.* **2015**, *54*, 3465–3520.
- (2) Thomas, J. M. *Chem. Eur. J.* **1997**, *3*.
- (3) Thomas, J. M. *Proc. R. Soc. A* **2012**, *468*, 1884–1903.
- (4) Thomas, J. M., *Design and applications of single-site heterogeneous catalysts: contributions to green chemistry, clean technology and sustainability*; World Scientific Publishing Company: 2012.
- (5) Paolucci, C.; Khurana, I.; Parekh, A. A.; Li, S.; Shih, A. J.; Li, H.; Iorio, J. R. D.; Albarracin-Caballero, J. D.; Yezerets, A.; Miller, J. T.; Delgass, W. N.; Ribeiro, F. H.; Schneider, W. F.; Gounder, R. *Science* **2017**, *357*, 898–903.
- (6) Vogt, E. T. C.; Weckhuysen, B. M. *Chem. Soc. Rev.* **2015**, *44*, 7342–7370.
- (7) *Nat. Mater.* **2020**, *19*, 1037.
- (8) Vermeiren, W.; Gilson, J.-P. *Top. Catal.* **2009**, *52*, 1131–1161.
- (9) Corma, A.; Zones, S.; Cejka, J., *Zeolites and catalysis: synthesis, reactions and applications*; John Wiley & Sons, Ltd: 2010.
- (10) Tian, P.; Wei, Y.; Ye, M.; Liu, Z. *ACS Catal.* **2015**, *5*, 1922–1938.
- (11) Bjørgen, M.; Joensen, F.; Spangsberg Holm, M.; Olsbye, U.; Lillerud, K.-P.; Svelle, S. *Appl. Catal. A* **2008**, *345*, 43–50.
- (12) Minachev, K. M.; Garanin, V.; Kharlamov, V.; Isakova, T.; Senderov, E. *Russ. Chem. Bull.* **1969**, *18*, 1611–1615.
- (13) Snyder, B. E. R.; Bols, M. L.; Schoonheydt, R. A.; Sels, B. F.; Solomon, E. I. *Chem. Rev.* **2018**, *118*, 2718–2768.
- (14) Rhoda, H. M.; Heyer, A. J.; Snyder, B. E. R.; Plessers, D.; Bols, M. L.; Schoonheydt, R. A.; Sels, B. F.; Solomon, E. I. *Chem. Rev.* **2022**, *122*, 12207–12243.
- (15) Li, Y.; Li, L.; Yu, J. *Chem* **2017**, *3*, 928–949.

- (16) Newton, M. A.; Knorpp, A. J.; Sushkevich, V. L.; Palagin, D.; van Bokhoven, J. A. *Chem. Soc. Rev.* **2020**, *49*, 1449–1486.
- (17) Borfecchia, E.; Beato, P.; Svelle, S.; Olsbye, U.; Lamberti, C.; Bordiga, S. *Chem. Soc. Rev.* **2018**, *47*, 8097–8133.
- (18) Iwamoto, M.; Furukawa, H.; Mine, Y.; Uemura, F.; Mikuriya, S.-i.; Kagawa, S. *J. Chem. Soc., Chem. Commun.* **1986**, 1272–1273.
- (19) Newton, M. A.; Knorpp, A. J.; Pinar, A. B.; Sushkevich, V. L.; Palagin, D.; van Bokhoven, J. A. *J. Am. Chem. Soc.* **2018**, *140*, 10090–10093.
- (20) Pappas, D. K. et al. *J. Am. Chem. Soc.* **2018**, *140*, 15270–15278.
- (21) Fickel, D. W.; Lobo, R. F. *J. Phys. Chem. C* **2010**, *114*, 1633–1640.
- (22) Korhonen, S. T.; Fickel, D. W.; Lobo, R. F.; Weckhuysen, B. M.; Beale, A. M. *Chem. Commun.* **2011**, *47*, 800–802.
- (23) Deka, U.; Juhin, A.; Eilertsen, E. A.; Emerich, H.; Green, M. A.; Korhonen, S. T.; Weckhuysen, B. M.; Beale, A. M. *J. Phys. Chem. C* **2012**, *116*, 4809–4818.
- (24) Borfecchia, E.; Lomachenko, K. A.; Giordanino, F.; Falsig, H.; Beato, P.; Soldatov, A. V.; Bordiga, S.; Lamberti, C. *Chem. Sci.* **2015**, *6*, 548–563.
- (25) Martini, A.; Borfecchia, E.; Lomachenko, K. A.; Pankin, I. A.; Negri, C.; Berlier, G.; Beato, P.; Falsig, H.; Bordiga, S.; Lamberti, C. *Chem. Sci.* **2017**, *8*, 6836–6851.
- (26) Paolucci, C.; Parekh, A. A.; Khurana, I.; Di Iorio, J. R.; Li, H.; Albarracin Caballero, J. D.; Shih, A. J.; Anggara, T.; Delgass, W. N.; Miller, J. T.; Ribeiro, F. H.; Gounder, R.; Schneider, W. F. *J. Am. Chem. Soc.* **2016**, *138*, 6028–6048.
- (27) Andersen, C. W.; Bremholm, M.; Vennestrøm, P. N. R.; Blichfeld, A. B.; Lundegaard, L. F.; Iversen, B. B. *IUCrJ* **2014**, *1*, 382–386.
- (28) Andersen, C. W.; Borfecchia, E.; Bremholm, M.; Jørgensen, M. R. V.; Vennestrøm, P. N. R.; Lamberti, C.; Lundegaard, L. F.; Iversen, B. B. *Angew. Chem. Int. Ed.* **2017**, *56*, 10367–10372.
- (29) Godiksen, A.; Vennestrøm, P. N. R.; Rasmussen, S. B.; Mossin, S. *Top. Catal.* **2017**, *60*, 13–29.
- (30) Groothaert, M. H.; Pierloot, K.; Delabie, A.; Schoonheydt, R. A. *Phys. Chem. Chem. Phys.* **2003**, *5*, 2135–2144.
- (31) Pöppel, A.; Kevan, L. *J. Phys. Chem.* **1996**, *100*, 3387–3394.
- (32) Actis, A.; Salvadori, E.; Chiesa, M. *Catal. Sci. Technol.* **2021**, *11*, 5191–5199.

- (33) Zamadics, M.; Kevan, L. *J. Phys. Chem.* **1992**, *96*, 8989–8993.
- (34) Carl, P. J.; Larsen, S. C. *J. Catal.* **1999**, *182*, 208–218.
- (35) Larsen, S. C.; Aylor, A.; Bell, A. T.; Reimer, J. A. *J. Phys. Chem.* **1994**, *98*, 11533–11540.
- (36) Conesa, J. C.; Soria, J. *J. Chem. Soc., Faraday Trans. 1* **1979**, *75*, 406–422.
- (37) Gao, F.; Walter, E. D.; Karp, E. M.; Luo, J.; Tonkyn, R. G.; Kwak, J. H.; Szanyi, J.; Peden, C. H. *J. Catal.* **2013**, *300*, 20–29.
- (38) Vanelderen, P.; Vancauwenbergh, J.; Tsai, M.-L.; Hadt, R. G.; Solomon, E. I.; Schoonheydt, R. A.; Sels, B. F. *ChemPhysChem* **2014**, *15*, 91–99.
- (39) Yu, J. S.; Kevan, L. *J. Phys. Chem.* **1990**, *94*, 5995–6002.
- (40) Wang, A.; Chen, Y.; Walter, E. D.; Washton, N. M.; Mei, D.; Varga, T.; Wang, Y.; Szanyi, J.; Wang, Y.; Peden, C. H.; Gao, F. *Nat. Commun.* **2019**, *10*, 1–10.
- (41) Giamello, E.; Murphy, D.; Magnacca, G.; Morterra, C.; Shioya, Y.; Nomura, T.; Anpo, M. *J. Catal.* **1992**, *136*, 510–520.
- (42) Llabrés i Xamena, F. X.; Fiscaro, P.; Berlier, G.; Zecchina, A.; Palomino, G. T.; Prestipino, C.; Bordiga, S.; Giamello, E.; Lamberti, C. *J. Phys. Chem. B* **2003**, *107*, 7036–7044.
- (43) Turnes Palomino, G.; Fiscaro, P.; Bordiga, S.; Zecchina, A.; Giamello, E.; Lamberti, C. *J. Phys. Chem. B* **2000**, *104*, 4064–4073.
- (44) Carl, P. J.; Vaughan, D. E. W.; Goldfarb, D. *J. Phys. Chem. B* **2002**, *106*, 5428–5437.
- (45) Carl, P. J.; Vaughan, D. E. W.; Goldfarb, D. *J. Am. Chem. Soc.* **2006**, *128*, 7160–7161.
- (46) Goldfarb, D.; Kevan, L. *J. Magn. Reson.* **1989**, *82*, 270–289.
- (47) Dedeczek, J.; Sobalik, Z.; Tvaruazkova, Z.; Kaucky, D.; Wichterlova, B. *J. Phys. Chem.* **1995**, *99*, 16327–16337.
- (48) Anderson, M. W.; Kevan, L. *J. Phys. Chem.* **1987**, *91*, 4174–4179.
- (49) Chao, C.-C.; Lunsford, J. H. *J. Chem. Phys.* **1973**, *59*, 3920–3925.
- (50) Conesa, J.; Soria, J. *J. Phys. Chem.* **1978**, *82*, 1847–1850.
- (51) Godiksen, A.; Stappen, F. N.; Vennestrom, P. N. R.; Giordanino, F.; Rasmussen, S. B.; Lundegaard, L. F.; Mossin, S. *J. Phys. Chem. C* **2014**, *118*, 23126–23138.

- (52) Song, J.; Wang, Y.; Walter, E. D.; Washton, N. M.; Mei, D.; Kovarik, L.; Engelhard, M. H.; Proding, S.; Wang, Y.; Peden, C. H. F.; Gao, F. *ACS Catal.* **2017**, *7*, 8214–8227.
- (53) Zhang, Y.; Wu, Y.; Peng, Y.; Li, J.; Walter, E. D.; Chen, Y.; Washton, N. M.; Szanyi, J.; Wang, Y.; Gao, F. *J. Phys. Chem. C* **2020**, *124*, 28061–28073.
- (54) Umamaheswari, V.; Hartmann, M.; Pöppel, A. *J. Phys. Chem. B* **2005**, *109*, 1537–1546.
- (55) Pöppel, A.; Hartmann, M. In *Impact of Zeolites and other Porous Materials on the new Technologies at the Beginning of the New Millennium*, Aiello, R., Giordano, G., Testa, F., Eds.; Studies in Surface Science and Catalysis, Vol. 142; Elsevier: 2002, pp 375–382.
- (56) Neyman, K. M.; Ganyushin, D. I.; Nasluzov, V. A.; Rösch, N.; Pöppel, A.; Hartmann, M. *Phys. Chem. Chem. Phys.* **2003**, *5*, 2429–2434.
- (57) Umamaheswari, V.; Hartmann, M.; Pöppel, A. *J. Phys. Chem. B* **2005**, *109*, 19723–19731.
- (58) Umamaheswari, V.; Pöppel, A.; Hartmann, M. *J. Mol. Catal. A: Chem.* **2004**, *223*, 123–128.
- (59) Umamaheswari, V.; Hartmann, M.; Pöppel, A. *J. Phys. Chem. B* **2005**, *109*, 10842–10848.
- (60) Sojka, Z.; Che, M.; Giamello, E. *J. Phys. Chem. B* **1997**, *101*, 4831–4838.
- (61) Park, S.-K.; Kurshev, V.; Luan, Z.; Wee Lee, C.; Kevan, L. *Microporous Mesoporous Mater.* **2000**, *38*, 255–266.
- (62) Böhlmann, W.; Pöppel, A.; Michel, D. *Colloids Surf.* **1999**, *158*, 235–240.
- (63) Biglino, D.; Li, H.; Erickson, R.; Lund, A.; Yahiro, H.; Shiotani, M. *Phys. Chem. Chem. Phys.* **1999**, *1*, 2887–2896.
- (64) Li, H.; Biglino, D.; Erickson, R.; Lund, A. *Chem. Phys. Lett.* **1997**, *266*, 417–421.
- (65) Gromov, I.; Krymov, V.; Manikandan, P.; Arieli, D.; Goldfarb, D. *J. Magn. Reson.* **1999**, *139*, 8–17.
- (66) Goldfarb, D. *Phys. Chem. Chem. Phys.* **2006**, *8*, 2325–2343.
- (67) McWeeny, R. *The Journal of Chemical Physics* **1965**, *42*, 1717–1725.
- (68) Neese, F. In *eMagRes*; John Wiley & Sons, Ltd: 2017, pp 1–22.
- (69) Fernández, E.; Moreno-González, M.; Moliner, M.; Blasco, T.; Boronat, M.; Corma, A. *Top. Catal.* **2018**, *61*, 810–832.
- (70) Ames, W. M.; Larsen, S. C. *J. Phys. Chem. A* **2010**, *114*, 589–594.

- (71) Ames, W. M.; Larsen, S. C. *J. Phys. Chem. A* **2009**, *113*, 4305–4312.
- (72) Pierloot, K.; Delabie, A.; Groothaert, M. H.; Schoonheydt, R. A. *Phys. Chem. Chem. Phys.* **2001**, *3*, 2174–2183.
- (73) Delabie, A.; Pierloot, K.; Groothaert, M. H.; Weckhuysen, B. M.; Schoonheydt, R. A. *Phys. Chem. Chem. Phys.* **2002**, *4*, 134–145.
- (74) Neese, F. J. *Chem. Phys.* **2003**, *118*, 3939–3948.
- (75) Neese, F. J. *Chem. Phys.* **2001**, *115*, 11080–11096.
- (76) Munzarová, M.; Kaupp, M. J. *Phys. Chem. A* **1999**, *103*, 9966–9983.
- (77) Neese, F. *Coord. Chem. Rev.* **2009**, *253*, Theory and Computing in Contemporary Coordination Chemistry, 526–563.
- (78) Bruzzese, P. C.; Salvadori, E.; Jäger, S.; Hartmann, M.; Civalleri, B.; Pöppl, A.; Chiesa, M. *Nat. Commun.* **2021**, *12*, 1–13.
- (79) Bruzzese, P. C.; Salvadori, E.; Civalleri, B.; Jäger, S.; Hartmann, M.; Pöppl, A.; Chiesa, M. *J. Am. Chem. Soc.* **2022**, *144*, 13079–13083.
- (80) Pidko, E. A. *ACS Catal.* **2017**, *7*, 4230–4234.
- (81) Goldfarb, D.; Stoll, S., *EPR spectroscopy: fundamentals and methods*; John Wiley & Sons, Ltd: 2018.
- (82) Mabbs, F.; Collison, D., *Electron paramagnetic resonance of d transition metal compounds*; Elsevier: 1992.
- (83) Brustolon, M.; Giamello, E., *Electron Paramagnetic Resonance: A Practitioners Toolkit*; John Wiley & Sons, Ltd: 2009.
- (84) Abragam, A.; Pryce, M. H. L.; Simon, F. E. *Proc. Roy. Soc.* **1951**, *205*, 135–153.
- (85) Weltner, W., *Magnetic atoms and molecules*; Dover Publications: 1938.
- (86) Pilbrow, J. R.; Hanson, G. R. In *Metallobiochemistry Part D: Physical and Spectroscopic Methods for Probing Metal Ion Environment in Metalloproteins*; Methods in Enzymology, Vol. 227; Academic Press: 1993, pp 330–353.
- (87) Stoll, S.; Schweiger, A. *J. Magn. Reson.* **2006**, *178*, 42–55.
- (88) Weil, J. A.; Bolton, J. R., *Electron Paramagnetic Resonance: elementary theory and practical applications*; Springer: 1986.
- (89) Schweiger, A.; Jeschke, G., *Principles of pulse electron paramagnetic resonance*; Oxford University Press: 2001.
- (90) Levitt, M. H., *Spin dynamics: basics of nuclear magnetic resonance*; John Wiley & Sons, Ltd: 2013.

- (91) Bloch, F. *Phys. Rev.* **1946**, 70, 460–474.
- (92) Hahn, E. L.; Maxwell, D. E. *Phys. Rev.*, 84, 1246–1247.
- (93) Mims, W. B. *Phys. Rev. B* **1972**, 5, 2409–2419.
- (94) Van Doorslaer, S. In *eMagRes*; John Wiley & Sons, Ltd: 2017, pp 51–70.
- (95) Rowan, L. G.; Hahn, E. L.; Mims, W. B. *Phys. Rev.* **1965**, 137, A61–A71.
- (96) Dikanov, S. A.; Tsvetkov, Y., *Electron spin echo envelope modulation (ESEEM) spectroscopy*; CRC press: 1992.
- (97) Mims, W. B. *Phys. Rev. B* **1972**, 6, 3543–3545.
- (98) Höfer, P.; Grupp, A.; Nebenführ, H.; Mehring, M. *Chem. Phys. Lett.* **1986**, 132, 279–282.
- (99) Hofer, P. J. *Magn. Reson., Ser. A* **1994**, 111, 77–86.
- (100) Hanson, G.; Berliner, L., *High resolution EPR: applications to metalloenzymes and metals in medicine*; Springer Science & Business Media: 2009; Vol. 28.
- (101) Davies, E. *Phys. Lett. A* **1974**, 47, 1–2.
- (102) Mims, W. B. *Proc. R. Soc. Lond. A Math. Phys. Sci.* **1965**, 283, 452–457.
- (103) Harmer, J. R. In *eMagRes*; John Wiley & Sons, Ltd: 2016, pp 1493–1514.
- (104) Fan, C.; Doan, P. E.; Davoust, C. E.; Hoffman, B. M. *J. Magn. Reson.* **1992**, 98, 62–72.
- (105) Jahn, H. A.; Teller, E. *Proc. R. Soc. A-Math. Phys. Sci.* **1937**, 161, 220–235.
- (106) Dunn, T. *Trans. Faraday Soc.* **1961**, 57, 1441–1444.
- (107) Peisach, J.; Blumberg, W. *Arch. Biochem. Biophys.* **1974**, 165, 691–708.
- (108) Carl, P. J.; Larsen, S. C. *J. Phys. Chem. B* **2000**, 104, 6568–6575.
- (109) Jensen, F., *Introduction to computational chemistry*; John Wiley & Sons, Ltd: 2017.
- (110) Dovesi, R.; Erba, A.; Orlando, R.; Zicovich-Wilson, C. M.; Civalleri, B.; Maschio, L.; Rérat, M.; Casassa, S.; Baima, J.; Salustro, S.; Kirtman, B. *WIREs Comput. Mol. Sci.*, 8, e1360.
- (111) Strange, P., *Relativistic Quantum Mechanics: with applications in condensed matter and atomic physics*; Cambridge University Press: 1998.
- (112) McWeeny, R.; Pickup, B. T. *Rep. Prog. Phys.* **1980**, 43, 1065–1144.



- (113) Dovesi, R.; Civalieri, B.; Roetti, C.; Saunders, V. R.; Orlando, R. In *Reviews in Computational Chemistry*; John Wiley & Sons, Ltd: 2005; Chapter 1, pp 1–125.
- (114) Harriman, J. E., *Theoretical foundations of electron spin resonance: physical chemistry: a series of monographs*; Academic press: 2013.
- (115) McWeeny, R. In *Methods in Computational Molecular Physics*, Wilson, S., Diercksen, G. H. F., Eds.; Springer US: Boston, MA, 1992, pp 3–17.
- (116) Neese, F. *J. Chem. Phys.* **2005**, *122*, 034107.
- (117) Heß, B. A.; Marian, C. M.; Wahlgren, U.; Gropen, O. *Chem. Phys. Lett.* **1996**, *251*, 365–371.
- (118) McWeeny, R. *J. Chem. Phys.* **1965**, *42*, 1717–1725.
- (119) Neese, F.; Solomon, E. I. *Inorg. Chem.* **1998**, *37*, 6568–6582.
- (120) Ditchfield, R. *Mol. Phys.* **1974**, *27*, 789–807.
- (121) Wolinski, K.; Hinton, J. F.; Pulay, P. *J. Am. Chem. Soc.* **1990**, *112*, 8251–8260.
- (122) Stanton, R. E. *J. Chem. Phys.* **1962**, *36*, 1298–1300.
- (123) In Löwdin, P.-O., Ed.; *Adv. Quantum Chem.* Vol. 1; Academic Press: 1964, pp 255–374.
- (124) Vahtras, O.; Minaev, B.; Ågren, H. *Chem. Phys. Lett.* **1997**, *281*, 186–192.
- (125) Y. Yamaguchi Y. Osamura, J. G.; Schaefer, H., *A New Dimension to Quantum Chemistry. Analytic Derivative Methods in Ab Initio Molecular Electronic Structure Theory*; Oxford University Press: 1994.
- (126) Atanasov, M.; Aravena, D.; Suturina, E.; Bill, E.; Maganas, D.; Neese, F. *Coord. Chem. Rev.* **2015**, *289-290*, 177–214.
- (127) Parr, R. G. et al., *Density functional theory of atoms and molecules*; Oxford University Press: 1989.
- (128) Hohenberg, P.; Kohn, W. *Phys. Rev.* **1964**, *136*, B864–B871.
- (129) Kohn, W.; Sham, L. J. *Phys. Rev.* **1965**, *140*, A1133–A1138.
- (130) Perdew, J. P. *Phys. Rev. B* **1986**, *33*, 8822–8824.
- (131) Becke, A. D. *J. Chem. Phys.* **1993**, *98*, 5648–5652.
- (132) Lee, C.; Yang, W.; Parr, R. G. *Phys. Rev. B* **1988**, *37*, 785–789.
- (133) Zhao, Y.; Truhlar, D. G. *Acc. of Chem. Res.* **2008**, *41*, 157–167.
- (134) Grimme, S. *J. Chem. Phys.* **2006**, *124*, 034108.
- (135) Grimme, S. *J. Comput. Chem.* **2004**, *25*, 1463–1473.

- (136) Grimme, S.; Hansen, A.; Brandenburg, J. G.; Bannwarth, C. *Chem. Rev.* **2016**, *116*, 5105–5154.
- (137) Chai, J.-D.; Head-Gordon, M. *Phys. Chem. Chem. Phys.* **2008**, *10*, 6615–6620.
- (138) Grimme, S.; Ehrlich, S.; Goerigk, L. *J. Comput. Chem.* **2011**, *32*, 1456–1465.
- (139) Hartree, D. R. *Math. Proc. Camb. Philos. Soc.* **1928**, *24*, 111–132.
- (140) Hartree, D. R. *Math. Proc. Camb. Philos. Soc.* **1928**, *24*, 89–110.
- (141) Hartree, D. R. *Math. Proc. Camb. Philos. Soc.* **1928**, *24*, 426–437.
- (142) Bartlett, R. J.; Musiał, M. *Rev. Mod. Phys.* **2007**, *79*, 291–352.
- (143) Riplinger, C.; Pinski, P.; Becker, U.; Valeev, E. F.; Neese, F. *J. Chem. Phys.* **2016**, *144*, 024109.
- (144) Witwicki, M.; Walencik, P. K.; Jezierska, J. *J. Mol. Model.* **2020**, *26*, 1–12.
- (145) Gómez-Piñeiro, R. J.; Pantazis, D. A.; Orio, M. *ChemPhysChem* **2020**, *21*, 2667–2679.
- (146) Bloch, F. *Z. Phys.* **1929**, *52*, 555–600.
- (147) Giannozzi, P. et al. *J. Phys.: Condens. Matter* **2009**, *21*, 395502.
- (148) Giannozzi, P. et al. *J. Phys.: Condens. Matter* **2017**, *29*, 465901.
- (149) Kresse, G.; Hafner, J. *Phys. Rev. B* **1993**, *47*, 558–561.
- (150) Kresse, G.; Hafner, J. *Phys. Rev. B* **1994**, *49*, 14251–14269.
- (151) Kresse, G.; Furthmüller, J. *Comput. Mater. Sci.* **1996**, *6*, 15–50.
- (152) Kresse, G.; Furthmüller, J. *Phys. Rev. B* **1996**, *54*, 11169–11186.
- (153) Pack, J. D.; Monkhorst, H. J. *Phys. Rev. B* **1977**, *16*, 1748–1749.
- (154) Breck, D., *Zeolite Molecular Sieves*; John Wiley & Sons, Ltd: 1974; Vol. 634.
- (155) Jacobs, P.; Flanigen, E. M.; Jansen, J.; van Bekkum, H., *Introduction to zeolite science and practice*; Elsevier: 2001.
- (156) Baerlocher, C.; McCusker, L. B. Database of Zeolite Structures, <http://www.iza-structure.org/databases/>, 1996.
- (157) Treacy, M.; Higgins, J., *Collection of Simulated XRD Powder Patterns for Zeolites Fifth (5th) Revised Edition*; Elsevier: 2007.
- (158) Loewenstein, W. *Am. Mineral.* **1954**, *39*, 92–96.
- (159) Zecchina, A.; Bordiga, S.; Palomino, G. T.; Scarano, D.; Lamberti, C.; Salvalaggio, M. *J. Phys. Chem. B* **1999**, *103*, 3833–3844.

- (160) Lamberti, C.; Spoto, G.; Scarano, D.; Pazé, C.; Salvalaggio, M.; Bordiga, S.; Zecchina, A.; Turnes Palomino, G.; D'Acapito, F. *Chem. Phys. Lett.* **1997**, *269*, 500–508.
- (161) Prestipino, C.; Capello, L.; D'Acapito, F.; Lamberti, C. *Phys. Chem. Chem. Phys.* **2005**, *7*, 1743–1746.
- (162) Lamberti, C.; Turnes Palomino, G.; Bordiga, S.; Berlier, G.; D'Acapito, F.; Zecchina, A. *Angew. Chem. Int. Ed.* **2000**, *39*, 2138–2141.
- (163) Li, Z.; Xie, K.; Slade, R. C. *Appl. Catal. A* **2001**, *209*, 107–115.
- (164) Zhang, Y.; Drake, I. J.; Briggs, D. N.; Bell, A. T. *J. Catal.* **2006**, *244*, 219–229.
- (165) Dent, L.; Smith, J. *Nature* **1958**, *181*, 1794–1796.
- (166) Smith, J. V.; Rinaldi, F.; Dent Glasser, L. S. *Acta Crystallogr.* **1963**, *16*, 45–53.
- (167) Pluth, J.; Smith, J.; Mortier, W. *Mater. Res. Bull.* **1977**, *12*, 1001–1007.
- (168) Zones, S. I. U.S Patent, 4,544,538, 1985.
- (169) Giordanino, F.; Vennestrøm, P. N. R.; Lundegaard, L. F.; Stappen, F. N.; Mossin, S.; Beato, P.; Bordiga, S.; Lamberti, C. *Dalton Trans.* **2013**, *42*, 12741–12761.
- (170) Gao, F.; Peden, C. H. F. *Catalysts* **2018**, *8*.
- (171) Morra, E.; Signorile, M.; Salvadori, E.; Bordiga, S.; Giamello, E.; Chiesa, M. *Angew. Chem. Int.* **2019**, *58*, 12398–12403.
- (172) Hofer, P.; Eichhoff, U. In *Magnetic Resonance and its Applications*, 2020, pp 41–43.
- (173) Fischer, M. *Phys. Chem. Chem. Phys.* **2016**, *18*, 15738–15750.
- (174) Signorile, M.; Damin, A.; Bonino, F.; Crocellà, V.; Lamberti, C.; Bordiga, S. *J. Comput. Chem.* **2016**, *37*, 2659–2666.
- (175) Grimme, S.; Antony, J.; Ehrlich, S.; Krieg, H. *J. Chem. Phys.* **2010**, *132*, 154104.
- (176) Grimme, S.; Ehrlich, S.; Goerigk, L. *J. Comput. Chem.* **2011**, *32*, 1456–1465.
- (177) Peintinger, M. F.; Oliveira, D. V.; Bredow, T. *J. Comput. Chem.* **2013**, *34*, 451–459.
- (178) Eichkorn, K.; Weigend, F.; Treutler, O.; Ahlrichs, R. *Theor. Chem. Acc.* **1997**, *97*, 119–124.

- (179) Hedegård, E. D.; Kongsted, J.; Sauer, S. P. A. *J. Chem. Theory Comput.* **2011**, *7*, 4077–4087.
- (180) Barone, V. *J. Phys. Chem.* **1995**, *99*, 11659–11666.
- (181) Zicovich-Wilson, C. M.; Pascale, F.; Roetti, C.; Saunders, V. R.; Orlando, R.; Dovesi, R. *J. Comput. Chem.* **2004**, *25*, 1873–1881.
- (182) Pascale, F.; Zicovich-Wilson, C. M.; López Gejo, F.; Civalleri, B.; Orlando, R.; Dovesi, R. *J. Comput. Chem.* **2004**, *25*, 888–897.
- (183) Carteret, C.; De La Pierre, M.; Dossot, M.; Pascale, F.; Erba, A.; Dovesi, R. *J. Chem. Phys.* **2013**, *138*, 014201.
- (184) Ugliengo, P.; Pascale, F.; Mérawa, M.; Labéguerie, P.; Tosoni, S.; Dovesi, R. *J. Phys. Chem. B* **2004**, *108*, 13632–13637.
- (185) Pascale, F.; Tosoni, S.; Zicovich-Wilson, C.; Ugliengo, P.; Orlando, R.; Dovesi, R. *Chem. Phys. Lett.* **2004**, *396*, 308–315.
- (186) Lindberg, B. *J. Chem. Phys.* **1988**, *88*, 3805–3810.
- (187) Neese, F. *WIREs Comput. Mol. Sci.* **2018**, *8*, e1327.
- (188) Neese, F. *WIREs Comput. Mol. Sci.*, *n/a*, e1606.
- (189) Remenyi, C.; Reviakine, R.; Arbuznikov, A. V.; Vaara, J.; Kaupp, M. *J. Phys. Chem. A* **2004**, *108*, 5026–5033.
- (190) Sinnecker, S.; Slep, L. D.; Bill, E.; Neese, F. *Inorg. Chem.* **2005**, *44*, 2245–2254.
- (191) Weigend, F.; Ahlrichs, R. *Phys. Chem. Chem. Phys.* **2005**, *7*, 3297–3305.
- (192) Saitow, M.; Neese, F. *J. Chem. Phys.* **2018**, *149*, 034104.
- (193) Riplinger, C.; Neese, F. *J. Chem. Phys.* **2013**, *138*, 034106.
- (194) Saitow, M.; Becker, U.; Riplinger, C.; Valeev, E. F.; Neese, F. *J. Chem. Phys.* **2017**, *146*, 164105.
- (195) Dunning, T. H. *J. Chem. Phys.* **1989**, *90*, 1007–1023.
- (196) Peterson, K. A.; Dunning, T. H. *J. Chem. Phys.* **2002**, *117*, 10548–10560.
- (197) Kulkarni, A. R.; Zhao, Z.-J.; Siahrostami, S.; Nørskov, J. K.; Studt, F. *ACS Catal.* **2016**, *6*, 6531–6536.
- (198) Rhoda, H. M.; Plessers, D.; Heyer, A. J.; Bols, M. L.; Schoonheydt, R. A.; Sels, B. F.; Solomon, E. I. *J. Am. Chem. Soc.* **2021**, *143*, 7531–7540.
- (199) Ipek, B.; Wulfers, M. J.; Kim, H.; Göltl, F.; Hermans, I.; Smith, J. P.; Booksh, K. S.; Brown, C. M.; Lobo, R. F. *ACS Catal.* **2017**, *7*, 4291–4303.

- (200) Borfecchia, E.; Pappas, D. K.; Dyballa, M.; Lomachenko, K. A.; Negri, C.; Signorile, M.; Berlier, G. *Catal. Today* **2019**, *333*, 17–27.
- (201) Peng, L.; Liu, Y.; Kim, N.; Readman, J. E.; Grey, C. P. *Nat. Mater.* **2005**, *4*, 216–219.
- (202) Heard, C. J.; Grajciar, L.; Rice, C. M.; Pugh, S. M.; Nachtigall, P.; Ashbrook, S. E.; Morris, R. E. *Nat. commun.* **2019**, *10*, 1–7.
- (203) Enemark, J. H.; Astashkin, A. V.; Raitsimring, A. M. *Biochem. Soc. Trans.* **2008**, *36*, 1129–1133.
- (204) Kaminker, I.; Goldberg, H.; Neumann, R.; Goldfarb, D. *Chem. Eur. J.* **2010**, *16*, 10014–10020.
- (205) Colaneri, M. J.; Vitali, J. *J. Phys. Chem. A* **2018**, *122*, 6214–6224.
- (206) Burdi, D.; Sturgeon, B. E.; Tong, W. H.; Stubbe, J.; Hoffman, B. M. *J. Am. Chem. Soc.* **1996**, *118*, 281–282.
- (207) Chiesa, M.; Giamello, E.; Di Valentin, C.; Pacchioni, G.; Sojka, Z.; Van Doorslaer, S. *J. Am. Chem. Soc.* **2005**, *127*, 16935–16944.
- (208) Raitsimring, A. M.; Astashkin, A. V.; Baute, D.; Goldfarb, D.; Poluektov, O. G.; Lowe, M. P.; Zech, S. G.; Caravan, P. *ChemPhysChem* **2006**, *7*, 1590–1597.
- (209) Palagin, D.; Sushkevich, V. L.; van Bokhoven, J. A. *ACS Catal.* **2019**, *9*, 10365–10374.
- (210) Koishybay, A.; Shantz, D. F. *J. Am. Chem. Soc.* **2020**, *142*, 11962–11966.
- (211) Paolucci, C.; Di Iorio, J. R.; Schneider, W. F.; Gounder, R. *Acc. Chem. Res.* **2020**, *53*, 1881–1892.
- (212) Negri, C.; Selleri, T.; Borfecchia, E.; Martini, A.; Lomachenko, K. A.; Janssens, T. V. W.; Cutini, M.; Bordiga, S.; Berlier, G. *J. Am. Chem. Soc.* **2020**, *142*, 15884–15896.
- (213) Sushkevich, V. L.; Smirnov, A. V.; van Bokhoven, J. A. *J. Phys. Chem. C* **2019**, *123*, 9926–9934.
- (214) Gao, F.; Kwak, J. H.; Szanyi, J.; Peden, C. H. *Top. Catal.* **2013**, *56*, 1441–1459.
- (215) Ma, L.; Cheng, Y.; Cavataio, G.; McCabe, R. W.; Fu, L.; Li, J. *Chem. Eng. J.* **2013**, *225*, 323–330.
- (216) Kim, Y. J.; Lee, J. K.; Min, K. M.; Hong, S. B.; Nam, I.-S.; Cho, B. K. *J. Catal.* **2014**, *311*, 447–457.
- (217) Morra, E.; Berlier, G.; Borfecchia, E.; Bordiga, S.; Beato, P.; Chiesa, M. *J. Phys. Chem. C* **2017**, *121*, 14238–14245.

- (218) Freude, D.; Haase, J.; Pfeifer, H.; Prager, D.; Scheler, G. *Chem. Phys. Lett.* **1985**, *114*, 143–146.
- (219) Hadt, R. G.; Gorelsky, S. I.; Solomon, E. I. *J. Am. Chem. Soc.* **2014**, *136*, 15034–15045.
- (220) Hadt, R. G.; Sun, N.; Marshall, N. M.; Hodgson, K. O.; Hedman, B.; Lu, Y.; Solomon, E. I. *J. Am. Chem. Soc.* **2012**, *134*, 16701–16716.
- (221) Yagi, S.; Yamada, I.; Tsukasaki, H.; Seno, A.; Murakami, M.; Fujii, H.; Chen, H.; Umezawa, N.; Abe, H.; Nishiyama, N., et al. *Nat. Commun.* **2015**, *6*, 1–6.
- (222) Lim, H.-K.; Shin, H.; Goddard, W. A.; Hwang, Y. J.; Min, B. K.; Kim, H. *J. Am. Chem. Soc.* **2014**, *136*, 11355–11361.
- (223) Shadle, S. E.; Hedman, B.; Hodgson, K. O.; Solomon, E. I. *Inorg. Chem.* **1994**, *33*, 4235–4244.
- (224) Göltl, F.; Buló, R. E.; Hafner, J.; Sautet, P. *J. Phys. Chem. Lett.* **2013**, *4*, 2244–2249.
- (225) Kerkeni, B.; Berthout, D.; Berthomieu, D.; Doronkin, D. E.; Casapu, M.; Grunwaldt, J.-D.; Chizallet, C. *J. Phys. Chem. C* **2018**, *122*, 16741–16755.
- (226) Pappas, D. K. et al. *J. Am. Chem. Soc.* **2017**, *139*, 14961–14975.
- (227) Negri, C.; Signorile, M.; Porcaro, N. G.; Borfecchia, E.; Berlier, G.; Janssens, T. V.; Bordiga, S. *Appl. Catal. A Gen.* **2019**, *578*, 1–9.
- (228) Ohyama, J.; Tsuchimura, Y.; Hirayama, A.; Iwai, H.; Yoshida, H.; Machida, M.; Nishimura, S.; Kato, K.; Takahashi, K. *ACS Catal.* **2022**, *12*, 2454–2462.
- (229) Sushkevich, V. L.; Artsiusheuski, M.; Klose, D.; Jeschke, G.; van Bokhoven, J. A. *Angew. Chem. Int. Ed.* **2021**, *60*, 15944–15953.
- (230) Gao, F.; Walter, E. D.; Kollar, M.; Wang, Y.; Szanyi, J.; Peden, C. H. *J. Catal.* **2014**, *319*, 1–14.
- (231) Öpik, U.; Pryce, M. H. L. *Proc. R. Soc. A: Math. Phys. Eng. Sci.* **1957**, *238*, 425–447.
- (232) Bersuker, I. B. *Chem. Rev.* **2013**, *113*, 1351–1390.
- (233) Hun Kwak, J.; Zhu, H.; Lee, J. H.; Peden, C. H. F.; Szanyi, J. *Chem. Commun.* **2012**, *48*, 4758–4760.
- (234) Villamaina, R.; Liu, S.; Nova, I.; Tronconi, E.; Ruggeri, M. P.; Collier, J.; York, A.; Thompsett, D. *ACS Catal.* **2019**, *9*, 8916–8927.

- (235) Valyon, J.; Keith Hall, W. *Catal. Lett.* **1993**, *19*, 109–119.
- (236) Li, H.; Paolucci, C.; Khurana, I.; Wilcox, L. N.; Göttl, F.; Albarracin-Caballero, J. D.; Shih, A. J.; Ribeiro, F. H.; Gounder, R.; Schneider, W. F. *Chem. Sci.* **2019**, *10*, 2373–2384.
- (237) Adamo, C.; Barone, V. *J. Chem. Phys.* **1999**, *110*, 6158–6170.
- (238) Perdew, J. P.; Wang, Y. *Phys. Rev. B*, *45*, 13244–13249.
- (239) Zhao, Y.; Truhlar, D. G. *Theor. Chem. Acc.* **2008**, *120*, 215–241.
- (240) Goerigk, L.; Hansen, A.; Bauer, C.; Ehrlich, S.; Najibi, A.; Grimme, S. *Phys. Chem. Chem. Phys.* **2017**, *19*, 32184–32215.
- (241) Perdew, J. P.; Zunger, A. *Phys. Rev. B* **1981**, *23*, 5048–5079.
- (242) Sushkevich, V. L.; van Bokhoven, J. A. *Chem. Commun.* **2018**, *54*, 7447–7450.
- (243) Trout, B. L.; Chakraborty, A. K.; Bell, A. T. *J. Phys. Chem.* **1996**, *100*, 4173–4179.
- (244) Larsen, S. C. *J. Phys. Chem. A* **2001**, *105*, 8333–8338.
- (245) Villamaina, R.; Gramigni, F.; Iacobone, U.; Liu, S.; Nova, I.; Tronconi, E.; Ruggeri, M. P.; Collier, J.; York, A. P. E.; Thompsett, D. *Catalysts* **2021**, *11*.
- (246) Gemperle, C.; Schweiger, A. *Chem. Rev.* **1991**, *91*, 1481–1505.
- (247) Erba, A.; Baima, J.; Bush, I.; Orlando, R.; Dovesi, R. *J. Chem. Theory Comput.* **2017**, *13*, 5019–5027.
- (248) Dossi, C.; Fusi, A.; Moretti, G.; Recchia, S.; Psaro, R. *Appl. Catal. A Gen.* **1999**, *188*, 107–119.
- (249) Kuroda, Y.; Iwamoto, M. *Top. Catal.* **2004**, *28*, 111–118.

# Publications

- [1] Palčić, A.; **Bruzzese, P. C.**; Pyra, K.; Bertmer, M.; Góra-Marek, K.; Poppitz, D.; Pöppl, A.; Gläser, R. and Jabłońska, M. “Nanosized Cu-SSZ-13 and Its Application in NH<sub>3</sub>-SCR.” *Catalysts*, **2020**, 10(5), 506.
- [2] Bracci, M; **Bruzzese, P. C.**; Famulari, A.; Fioco, D.; Guidetti, A.; Liao, Y-K; Podvorica, L.; Rezayi, F. S.; Serra, I.; Thangavel, K. and Murphy, D. “Paramagnetic species in catalysis research: a unified approach towards (the role of EPR in) heterogeneous, homogeneous and enzyme catalysis.” In *Electron Paramagnetic Resonance: Volume 27*, **2021**, 27,1-46.
- [3] Jabłońska, M.; Góra-Marek, K.; Grilc, M; **Bruzzese, P. C.**; Poppitz, D.; Pyra, K.; Liebau, M; Pöppl, A.; Likozar, B. and Gläser, R. “Effect of Textural Properties and Presence of Co-Cation on NH<sub>3</sub>-SCR Activity of Cu-Exchanged ZSM-5.” *Catalysts*, **2021**, 11(7), 843.
- [4] Liao, Y-K; **Bruzzese, P. C.**; Hartmann, M; Pöppl, A. and Chiesa, M. “Chromium Environment within Cr-Doped Silico-Aluminophosphate Molecular Sieves from Spin Density Studies.” *J. Phys. Chem. C*, **2021**, 125(15), 8116–8124.
- [5] **Bruzzese, P. C.**; Salvadori, E.; Jäger, S.; Hartmann, M; Civalleri, B.; Pöppl, A. and Chiesa, M. “<sup>17</sup>O-EPR determination of the structure and dynamics of copper single-metal sites in zeolites.” *Nat. Commun.*, **2021**, 12(1), 4638.
- [6] Jabłońska, M.; Góra-Marek, K.; **Bruzzese, P. C.**; Palčić, A.; Pyra, K.; Tarach, K.; Bertmer, M.; Poppitz, D.; Pöppl, A. and Gläser, R. “Influence of Framework n(Si)/n(Al) Ratio on the Nature of Cu Species in Cu-ZSM-5 for NH<sub>3</sub>-SCR-DeNO<sub>x</sub>” *ChemCatChem*, **2022**, e202200627.
- [7] **Bruzzese, P. C.**; Salvadori, E.; Civalleri, B.; Jäger, S.; Hartmann, M; Pöppl, A. and Chiesa, M. “The Structure of Monomeric Hydroxo-Cu<sup>II</sup> Species in



---

Cu-CHA. A Quantitative Assessment.” *J. Am. Chem. Soc.*, **2022**, 144(29), 13079–13083.

# Acknowledgments

This PhD project was enabled by the contribution of many people. Most importantly, I want to thank my two supervisors, namely Prof. Andreas Pöpl and Prof. Mario Chiesa. Their supervision accompanied me up to now, starting from my first steps in EPR. In particular, I hugely acknowledge Mario for his brilliant ideas and guidance throughout the project: his contribution has been fundamental for the achievement of the results presented in this thesis. Furthermore, I really appreciate the time and patience Andreas took for countless inspiring discussions, which deepened my understanding of EPR and broadened my perspective on many subjects related to this thesis.

I would like to thank all co-workers, PhD fellows, technicians and professors supported me during this journey in Leipzig. In particular, I want to thank Prof. Jürgen Haase for the opportunity working on my PhD in his group in the Felix Bloch Institute of Solid-State Physics of Leipzig University. In addition to him, I would like to thank former PhD students in Andreas group, Dr. Matthias Mendt and Dr. Anastasia Kuldaeva, who introduced me into the practical and technical aspects of EPR, including sample preparation, spectrometer handling and data processing. Moreover, I acknowledge Dr. Winfried Böhlmann for activating and guest loading samples, Stefan Schlayer for the continuous supply of liquid helium as well as advice in technical questions, the technicians Niklas Vetter and Lisa Marie Tauche for all their valuable assistance, my current PhD colleagues Kavipriya Thangavel and Muhammad Fernadi Lukman for their pleasant company and helping hands in the lab and outside the lab. I am grateful to Dr. Magdalena Jabłońska for the fruitful collaboration during my PhD project. I also gratefully acknowledge the support of the glass workers Stephan Eckert and Marko Wende who were involved in the preparation of almost any EPR sample tube.

A huge thank goes to Prof. Martin Hartmann and his group of the Erlangen Center for Interface Research and Catalysis not only for providing me the zeolite materials but also for teaching me the synthesis recipes. In particular, I really thank Dr. Stefan Jäger for his precious and valuable assistance during my secondment in Erlangen.

I am also indebted to the EPR group in Torino, where I spent one year of

my doctoral course. First, I greatly thank Prof. Enrico Salvadori for his invaluable support and guidance in the realization of the objectives of this project. I immensely acknowledge Dr. Valeria Lagostina for teaching me, helping me and assisting me with activation procedures, isotopic labelling and gas loading as well as valuable suggestions in sample preparations. Moreover, I would like to thank Prof. Stefano Livraghi for his assistance in the lab, Prof. Elio Giamello for his useful discussions and Prof. Maria Cristina Paganini for her support. Prof. Bartolomeo Civalleri and Lorenzo Donà are hugely acknowledged for their constant supervision and assistance concerning the computational part of the results of this thesis. Finally I thank Alessia Zollo, Leonora Podvorica, Arianna Actis, Chiara Bellomo, Stefania Cananà, Dr. Jasmine Rita Petriglieri, Sofia Frida Russi and David Fioco for the very lovely company in Torino.

Finally, I thank my fellows from the PARACAT project. In particular, big thanks go to Yu-Kai Liao for his valuable support in several scientific topics and for the pleasant chats.

I greatly acknowledge the financial support by the European Union's Horizon 2020 research and innovation programme under the Marie Skłodowska-Curie grant agreement No 813209.

A special thanks goes to Tony Famulari who supported me in a countless number of times. He enlightened the time spent together through his truthfulness, irony and sync with my thoughts.

Last but not least, I would like to thank my parents, my brother and Silvia for their love and constant support.